ENERGY LABORATORY
AND
MATERIALS PROCESSING CENTER

MASSACHUSETTS INSTITUTE
OF TECHNOLOGY

SINTERABLE POWDERS
FROM
LASER DRIVEN REACTIONS

BY

John S. Haggerty

September 1981

BUILDING NO. 12
MASSACHUSETTS INSTITUTE OF TECHNOLOGY
CAMBRIDGE, MASSACHUSETTS 02139

SINTERABLE POWDERS FROM LASER DRIVEN REACTIONS
FINAL REPORT

John S. Haggerty

Energy Laboratory

Massachusetts Institute of Technology
Cambridge, Massachusetts 02139

REPORT DOCUMENTATION PAGE		READ INSTRUCTIONS BEFORE COMPLETING FORM
1. REPORT NUMBER MIT-EL-82-002	2. GOVT ACCESSION NO. AD- 4114 062	3. RECIPIENT'S CATALOG NUMBER
4. TITLE (and Subtitle) Sinterable Powders from Laser Driven Reactions		5. TYPE OF REPORT & PERIOD COVERED 1 July 77 - 30 Sept. 81 Final Report
		6. PERFORMING ORG. REPORT NUMBER MIT-EL-82-002
7. AUTHOR(s) John S. Haggerty		8. CONTRACT OR GRANT NUMBER(s) N00014-77-C-0581
9. PERFORMING ORGANIZATION NAME AND ADDRESS Massachusetts Institute of Technology Cambridge, MA 02139		10. PROGRAM ELEMENT, PROJECT, TASK AREA & WORK UNIT NUMBERS NR 039-153/12-12-3-80
11. CONTROLLING OFFICE NAME AND ADDRESS O.N.R. Department of the Navy 800 North Quincy Street, Arlington, VA 22217		12. REPORT DATE March 1982
		13. NUMBER OF PAGES 164
14. MONITORING AGENCY NAME & ADDRESS(if different from Controlling Office)		15. SECURITY CLASS. (of this report) Unclassified
		15a. DECLASSIFICATION/DOWNGRADING SCHEDULE

16. DISTRIBUTION STATEMENT (of this Report)

Unrestricted

This document has been approved for public release and sale; its distribution is unlimited.

17. DISTRIBUTION STATEMENT (of the abstract entered in Block 20, if different from Report)

Unrestricted

18. SUPPLEMENTARY NOTES

19. KEY WORDS (Continue on reverse side if necessary and identify by block number)

Laser synthesis of powders   Silicon nitride powder
Laser driven reactions   Silicon carbide powder
Gas phase synthesis of powders   Ceramic powders
Silicon powder   Laser heated gases

20. ABSTRACT (Continue on reverse side if necessary and identify by block number)

Extremely fine, uniform ceramic powders have been synthesized from SiH_4 NH_3 and C_2H_4 gas phase reactants that are heated by absorbing optical energy emitted from a CO_2 laser. Resulting Si, Si_3N_4 and SiC powders have been characterized in terms of parameters which are important for densification processes. They are virtually ideal. The spherical particles typically have mean diameters from 120 to 1500 Å. The standard deviation is typically 25-45% and the diameter of the largest observed particle is

DD FORM 1473   EDITION OF 1 NOV 65 IS OBSOLETE
1 JAN 73   S/N 0102-LF-014-6601

typically less than twice that of the smallest particle. Purities are extremely high. The laser heated process has been modeled in terms of fluid flow and heat transfer criteria and characterized with respect to particle growth rates and temperature distribution. Many fundamental property measurements were made to provide data for these calculations. The process is extremely efficient, ~95% of the SiH_4 is reacted in a single pass through the laser beam and approximately 2 kwhr. of energy are required per kilo of Si_3N_4.

The resulting powders have been processed into dense pieces using several shaping techniques. The Si powders were densified to precisely controlled levels designed to yield high density reaction bonded silicon nitride (RBSN). Nitriding kinetics were rapid at low temperatures because of the small particle sizes. Characteristic dimensions of RBSN microstructures approximated the initial particle dimensions. Sintering experiments with pure Si_3N_4 powder indicated that densification occurred without pressure or sintering aids. Characterization of mechanical properties showed that, with lower densities, strengths and K_{IC}'s equalled or exceeded those of high quality RBSN materials.

Accession For

NTIS GRA&I ☑
DTIC TAB ☐
Unannounced ☐
Justification

By
Distribution/
Availability Codes

Dist | Avail and/or Special

DTIC
COPY
INSPECTED
2

TABLE OF CONTENTS

TABLE OF CONTENTS (cont.)

TABLE OF CONTENTS (cont.)

LIST OF FIGURES

LIST OF FIGURES (cont.)

LIST OF TABLES

LIST OF TABLES

FORWARD

This research program involved several groups within M.I.T. which
represented different technical disciplines. The principal investigator,
Dr. J. S. Haggerty is a materials scientist associated with both the Energy
Laboratory and the Department of Materials Science and Engineering, as are
Dr. W. R. Cannon, who served as co-principal investigator for the first
three years. Dr. S. C. Danforth and Dr. S. Mizuta are Research Associates.
Mr. R. A. Marra is a Doctoral candidate in the Department of Materials
Science and Engineering and his research has contributed to every aspect of
this program. Mr. J. Flint, Ms. L. Schioler and Mr. H. Sawhill are Masters
candidate students in the Department of Materials Science and Engineering.
Ms. M. Gabriel and Mr. M. Schmaier are undergraduate students in the same
department who have worked on the project under the Undergraduate Research
Opportunities Program. Everyone's contributions are gratefully
acknowledged.

I INTRODUCTION

Increasingly, because of their superior properties, ceramic materials are being considered for applications involving high stress levels. The important properties include hardness, high temperature strength, erosion, oxidation and corrosion resistance, low density and, for some uses, specific electrical and optical properties. Their use in many of these applications can only be considered if their reliability is improved. As brittle materials, they fail catastrophically when a strength limiting defect becomes unstable in a stress field and propagates. In most cases, failure of an individual ceramic element would halt or dammage the entire system in which it was used. The wide distribution of strengths observed with ceramic materials forces engineers to design so conservatively that ceramics lose their intrinsic advantages relative to conventional materials.

Strength limiting defects are usually attributable to some specific event in the components processing history extending from powder synthesis through all the handling steps to the final consolidation into a densified part. There are many causes for strength limiting defects and their elimination continues to be the subject of processing research and component development programs. At M.I.T., we are approaching this problem from a new perspective[1] which requires that constituent powders satisfy rigid criteria. With the correct powders and handling procedures, it is possible to cause the individual particles to arrange in a close packed structure as shown in Figure 1. Bodies having this unusual internal structure will exhibit low, uniform shrinkage to theoretical density with low firing temperatures and short times. Short, low temperature densification cycles should virtually eliminate grain growth. Also, the characteristic size of remaining flaws should be approximately that of the particles since individual vacancies are the largest defect.

This research program has investigated laser means of producing powders with the following ideal characteristics: (1) the powder must have a small particle size, typically less than 0.5 μm; (2) the particles must be free of agglomerates; (3) the particle diameters must have a narrow range of sizes;

1

(4) the morphology of the particles must be equiaxed, tending toward
spherical shapes; (5) the powders must have highly controlled purity with
respect to contaminants and multiple polymorphic phases. Either with or
without the ordered structures shown in Figure 1, a powder exhibiting these
ideal characteristics should be sinterable to theoretical density without
resorting to pressure or additives and should permit the final grain
structure to be highly controllable.

Because existing powder synthesis techniques cannot produce powders
with these requisite characteristics, we have undertaken to determine
whether laser heated processes could. We investigated a selective
comminution process in the first year.[2] Since then, we have concentrated on
a laser heated gas phase synthesis process, once it was demonstrated we
could achieve the process conditions which result in uniform nucleation and
growth histories.[2,3,4] This phase of the program has emphasized synthesis

Figure 1. Ordered packing of monodispersed 0.2 μm diameter SiO_2 spheres.

of Si and Si_3N_4 powders. Preliminary synthesis experiments have been made
with SiC. The Si powders are used for the reaction bonding process in which
densification and conversion to Si_3N_4 occur simulultaneously. We have had
two specific objectives. Our initial and primary objective has been to
develop a process for producing ceramic powders with characteristics that
will permit a better understanding of the interactions between powder
characteristics, densification processes, and the properties of ceramic
bodies. Secondly, since very specific powder characteristics are required
to satisfy this objective, we have concentrated on developing an analytical
description of the synthesis process.

Several commercial processes are being used to synthesize Si_3N_4 and
SiC powders. Typically they involve DC arcs, conventional vapor phase
reactions in heated tube furnaces and nitriding or carbiding of silicon
metal. The nitriding of silicon metal typically leaves a silicon core
within the silicon nitride particle. Furthermore, because the process is
done in the solid state, particles must be separated by grinding, which does
not result in a narrow size distributed, non-agglomerated, phase pure
powder. The vapor phase methods (furnace heated vapor and arc plasma
techniques) yield finer and more uniform powders than the nitriding of solid
silicon, but these techniques have less than ideal thermal profiles in their
reaction zones which cause a distribution of nucleation and growth times and
the formation of agglomerates. Despite these specific process deficiencies,
synthesis from dilute gas phase reactants is one of the most promising
routes for producing powders having these specific ideal characteristics.

The laser driven gas phase reaction process investigated in this
program offers many advantages. It is a clean process because no
potentially contaminating surfaces are heated. The reaction zone is
precisely defined, consisting of the volume enclosed by the reactant gas
stream and resulting particles and the laser beam. The ability to maintain
steep temperature gradients in the effective thermal environment, and thus a
well defined reaction zone, should allow precise control of the nucleation
rate, the growth rate and exposure times, permitting the nucleation and

3

growth of very fine uniformly sized particles. The available power levels, the stability of the delivered power, cost, reliability and conversion efficiency all suggest the use of a CO_2 laser source provided that gases are identified which are optically absorbing at emitted wavelengths.

To develop an understanding of the interrelationships between powder characteristics and the synthesis process, it is necessary to be able to describe heating rates, nucleation and growth rates, and the distributions of temperature and mass flow throughout the "reaction zone". We have studied the effect of several process variables on powder characteristics[2,3,4]. These include beam intensity, gas composition (stoichiometry and dilution), gas pressure, and gas velocity. The effect of these process parameters has been correlated with both powder characteristics and process characteristics, e.g. emitted spectra, temperature, and percent conversion.

Two fundamentally different types of reactions have been investigated. Most of our work has been carried out under laser intensity and gas pressure conditions where many collisions occur between the gas molecules during the period that they are heated. These reactions probably proceed as normal thermal reactions. In this case, the principal advantages of the laser heat source are process control and possibly unique reaction paths because of high heating rates and resonance effects between the coherent light and the molecules. The second type of reaction is uniquely possible with laser heating. In this case, molecules absorb sufficient energy to dissociate before colliding with other molecules.

The uses of this synthesis technique as an experimental tool has tremendous potential, and its eventual use as a production tool appears increasingly probable. It is now apparent that it can be applied to elements, oxides, carbides, and nitrides. With slightly different process conditions, it can be used to deposit thin films rather than producing powders.

II OBJECTIVES AND APPROACHES

The broad objective of this program has been to find laser means of
producing powders which exhibit the characteristics stated in the
Introduction and then to demonstrate that superior properties and/or
processing characteristics result from using them. Our specific objectives
have changed during the course of the program as various important issues
were resolved favorably. During the first two years,[2,3] we conducted
research to determine the basic feasibility of the laser comminution and
laser heated gas phase synthesis processes. Resulting powders have been
fully characterized throughout the program. In year three,[4] we concentrated
on developing descriptions of both the laser heated process for synthesizing
the materials of interest, as well as the interaction between process
variables and powder characteristics. We also began processing the
resulting powders into shapes. In the final period, we concentrated on
processing the resulting powders, and began evaluating the properties of the
ceramic pieces to study the interaction between process variables and
properties.

A. Gas Phase Synthesis Process

The powder synthesis process employs an optical energy source to
transfer the energy required to initiate and sustain a chemical reaction in
the gas phase. In this process, the gas molecules are "self-heated"
throughout the gas volume, a process which is distinct from conventional
ones where heat is transmitted from a source to the gas molecules by a
combination of conduction, convection and radiative processes. The
advantages of this means of heating are freedom from contamination, absence
of surfaces that act as heterogeneous nucleation sites, and unusually
uniform and precise process control. These attributes permit the synthesis
of powders with characteristics that are ideal for making ceramic bodies.

A laser, rather than other possible optical heat sources, has been used
because of the narrow spectral width of emitted light and the brightness of

5

this type of light source. The coherency of the light was not considered an important feature for this process. Coupling between the source and the absorbing molecule requires virtual coincidence between the emission and the absorption lines. If this matching occurs, the optical-to-thermal efficiency can be extremely high and the overall process efficiency is essentially that of the laser. This efficiency is much higher than is possible with broad band light sources because only small fractions of their light are absorbed by the gases. With CO_2 lasers, as have been used in this program, the overall process efficiency matches or exceeds that of other conventional heat sources, e.g. various types of plasmas, torches or heated tubes. In addition to the high efficiency, the use of laser energy sources makes possible unique reaction paths which may produce powders with unusual characteristics.

Two basic ranges of laser intensity and exposure time have been investigated. Most of the synthesizing research has been carried out in conditions typical of the normal or thermal domain. We have also investigated the process under conditions anticipated to produce multi-photon, unimolecular reactions.

The laser beam enters the reaction chamber, Figure 2, through a KCl window and is arrested with a water cooled copper block. Power intensities range from 270-1020 watts/cm^2 for the unfocused beam, and reach up to 10^5 watts/cm^2 near the focal point of a 13 cm lens. The reactant gases (SiH_4 for Si, NH_3-SiH_4 for Si_3N_4, and C_2H_4-SiH_4 for SiC) enter the cell orthogonal to the laser beam through a 1.5 mm I.D. stainless steel nozzle 2-3 mm below the laser beam. A coaxial argon stream is used to suppress the expansion of the product stream with entrained particles, so these particles can be collected in a microfiber filter. Argon gas is directed across the KCl window to prevent powder collection there and possible breakage. The reactant gases employed are electronic grade SiH_4, NH_3, and C_2H_4. Prepurified argon is used as the inert buffer gas. The Ar gas train includes a Ti oxygen getter which typically achieves < 1 ppm O_2. Reaction cell pressures, ranging from 0.08 to 1.0 atm, are maintained by a throttling valve in series between the filter and the vacuum pump.
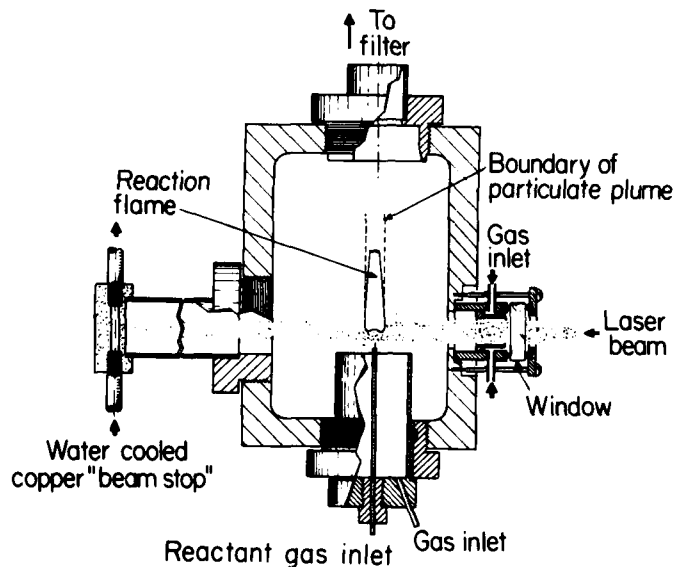
Figure 2. Schematic of powder synthesis cell.

Many features of the laser heated process are visible to the eye and can be recorded on conventional films. Figure 3 shows a photograph of the Si_3N_4 reaction flame taken under typical process conditions in a cross flow configuration. Figure 4 is a graphic, scaled representation of the reaction. It locates the flame and the boundary of the particulate plume with respect to the CO_2 laser beam.

The distribution of laser intensity observed in the CO_2 beam is shown in Figure 4. It was recorded by burning into a PMMA block where the depth of penetration is proportional to intensity. For comparison, the Gaussian distribution of an ideal $T_{M_{00}}$ mode is also shown. The actual intensity is sensitive to the alignment or "tuning" of the optical cavity and is found to vary slightly with the power level and time for any specific alignment. Although a difference between ideal and actual intensity distributions is evident, these results show that the total exposure to which a volume of gas is subjected as it passes through the laser beam is reasonably represented by the Gaussian function.

Two apparently anamalous features exhibited by the reaction flame are explained by the process conditions. The deflection of the flame and plume

7

Figure 4. Schematic representation of reaction photographed in Figure 3.

Figure 3. Photograph of a typical Si$_3$N$_4$ Synthesis Reaction Flame.

8

to the left of the vertical axis is caused by the Ar flow from the laser entrance window at the right side. The deflection angle is influenced by the reactant gas and/or argon flow rates. The bottom contour of the flame (one upper and two lower cusps) is determined by the parabolic velocity profile in the premixed reactants, rather than mass transport effects which cause similar shapes in diffusional flames.[5] The two lower cusps should be at the same level; but the relative positions of the right and left lower cusps is caused by dilution of the energy absorbing gas by Ar from the right side.

It has been possible to determine the existence of a particulate reaction product at any point by light scattering, using a He-Ne laser source ($\lambda = 6328$ Å). In this manner we have been able to identify where a reaction proceeded to any extent within SiH_4, NH_3+SiH_4 and $C_2H_4+SiH_4$ flames as well as where and how the reaction products leave the reaction zone. As the photograph in Figure 3 shows, the scattered light is readily visible either above the flame or within the transparent upper region of the flame. Within the luminous zone, it was necessary to make observations through a narrow bandpass filter to suppress the background light.

Scattering from particulate reaction products was evident throughout the flame. At the bottom side, scattering was first evident at a point coincident with the lower boundary of the luminous zone. Above that point, the optical densities of the flame and plume were measured to determine the nucleation and growth kinetics. Particles travel upward in a cylindrical plume as denoted by dotted lines in Figure 4. Within the accuracy of the measurements, the plume diameter is equal to the maximum diameter of the luminuous zone. We could not observe any distortion from a circular cross section in the plume.

Measurements of CO_2 laser power transmitted through the reaction zone support another assumption regarding the transparency of the reacted gases and particulate product to the 10.6 μm light. Burn patterns have been made to map the transmitted CO_2 laser intensity distribution both with and without reactant gases in its path. These results indicated that the reaction products were no more absorbing than the reactant gases. More

precise statements cannot be made because of the long optical pathlength in the cell ($\ell \simeq 22$ cm) which tends to accumulate unreacted NH_3 during a run. With the long path length, the absorption caused by the ammonia became the same order of magnitude as that absorbed by the reactant stream. It was evident, however, that there was neither a sharp boundary nor any systematic difference across the beam corresponding to the reaction which occurs at approximately the center of the beam (Figure 4).

The powders produced in the reaction zone are carried into the collection filter by the product and agron gases. The process typically produces 1 to 10 grams of powder per hour. Up to 10 grams can be collected before the filter fills and it is no longer possible to maintain a constant cell pressure. With recent equipment modifications, virtually all of the powder is transported to the filter. Based on mass balance, the laser induced reaction typically converts 85-100% of the reactants to products. The collected powders are sealed in the microfiber filter under a positive argon pressure. This filter assembly is then transferred into a glove box through a vacuum antechamber. All post-production handling is performed in a nitrogen environment maintained at less than 1.0 ppm each of O_2 and H_2O. In general the powders do not oxidize pyrophorically on exposure to air. In a very few cases, Si powders have burned spontaneously.

The results of this research program demonstrate that the laser heated synthesis process yields powders having virtually all of the desired characteristics. The resulting particles are small (< 1500 Å), uniform in size, spherical, and pure. The particles appear to be attached to one another in chain-like agglomerates, however, experiments have shown that the Si powders can be dispersed. Unlike the Si powders, direct examination by TEM usually shows no neck formation between Si_3N_4 and SiC particles. We anticipate that they can be dispersed more easily than Si.

Much of our effort has focused on developing an analytical description of the laser heated synthesis process. To develop a model, many fundamental property measurements were required, such as detailed absorptivity measurements for reactant gases as a function of pressure and emitted

10

wavelength. Emissions from the reaction have been studied to identify reaction species and to estimate the reaction temperature. Computer analyses of the gas flow were used to predict gas stream dimensions and velocities. Combined with direct observations of both the reaction positions relative to the laser beam and the reaction temperatures, these analyses and characterizations have been used to describe the time-temperature history of the reactant gases throughout the course of the reaction.

Most process variables were manipulated to determine their effect on particle characteristics. The variables which have a direct effect on the nucleation and growth kinetics include reaction temperature, heating rate, partial pressure of reactants, total pressure and dilution by inert gases. Most of these variables were manipulated to demonstrate their empirical effect on Si and Si_3N_4 powder characteristics.

Besides producing powders with ideal characteristics, the laser heated synthesis process is extremely efficient. Approximately 95% of SiH_4 is converted to powder in a single pass through the laser beam. Also, Si, Si_3N_4 and SiC powders can be produced from these reactants with as little as 2 kWhr of energy per kilogram of powder. It is likely that this process can produce both a superior and lower cost powder than conventional gas phase or solid phase synthesis processes.

B. Particle Size and Shape Modification

Controlled modification of particle size and shape by subjecting powders to high intensity laser illumination was successfully demonstrated in this phase of the first year's work[2]. Selective heating causes particle size reduction by vaporization until decoupling occurs when the oversize particles reach a specific dimension. This approach was based on the diameter dependence of the absorption efficiency (Q_{abs}) of electromagnetic radiation which small particles exhibit.

The Mie theory[6] shows that above a specific diameter, the particles absorb heat with a high efficiency that is independent of diameter. Below a

11

specific diameter, the absorption efficiency decreases with diameter so the particles effectively decouple from the radiation. The absorption efficiency calculated for Si_3N_4 particles is shown in Figure 5. This characteristic permits selective interaction with oversize particles. Their size can be reduced if they are heated long enough to cause considerable vaporization. Oversized particles can be eliminated from the powder, thus avoiding subsequent problems with discontinuous grain growth and strength limiting flaws associated with the oversized grains. Once the particles begin to decouple and cool down, the vaporization rate will effectively stop.

Process models were developed[2] which gave adequate agreement between analytical and observed experimental results. They indicated that two vaporization processes probably occur. At the highest intensities, Si_3N_4
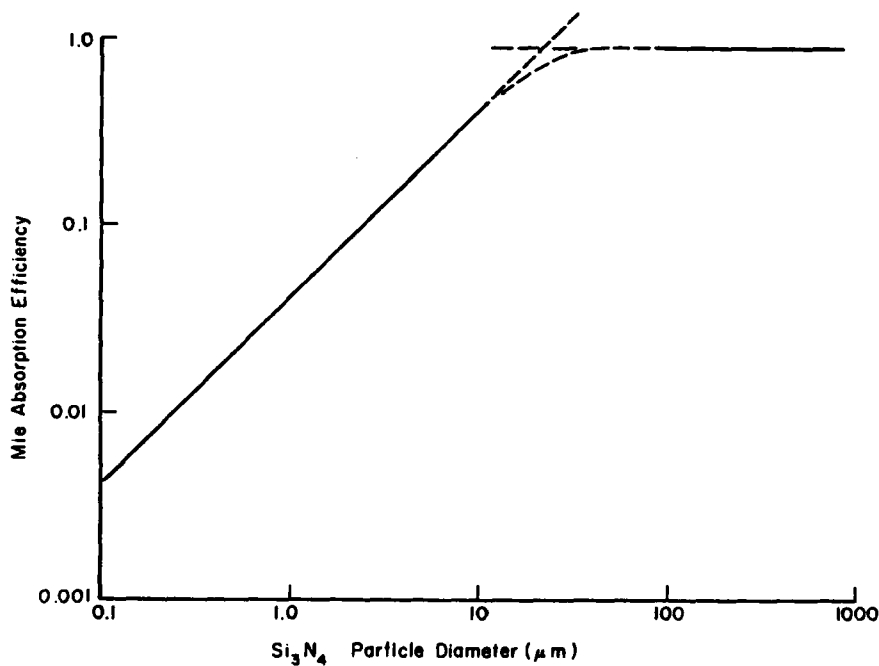
Figure 5. Mie absorption efficiency of Si_3N_4 particles to 10.6 µm light as a function of particle size.

particles vaporize as Si(g) and N_2(g). At lower intensities, they
apparently decompose by losing N_2(g), leaving molten Si.

The intensity-time exposures required to cause particle size reduction
were substantially more severe than predicted in our original analysis.
Achieving the process with a 150 watt laser was only marginally possible.
Most of the mapping of conditions which caused comminution was done with
supported particles in a pulsed laser mode. In this manner, longer and
higher intensity exposures were realized than could be achieved with CW, gas
entrained experiments.

These experiments demonstrated particle size reduction, leaving
equiaxed particles. They did not unequivocally demonstrate decoupling,
which will cause the predicted termination of the comminution process at a
specific particle size. Some of the results suggested that all of the
experiments were carried out in the domain where coupling efficiency was
dependent on particle size.

The pulsed experiments showed that the process should operate as a CW,
gas entrained process with approximately a 1.5 kW laser. These experiments
could not be completed because of the power limits imposed by then existing
laser equipment. They were not reinitiated when the higher power laser
equipment was aquired because it was evident that it would be an inherently
energy intensive process.

III POWDER SYNTHESIS FROM THE GAS PHASE

The character of this research program changed considerably from its inception. Initially, the concepts of forming powders by laser induced reactions had not been demonstrated. The program was viewed as having a high risk of not functioning as anticipated and most of the experiments were empirical. Since then it has been shown that the synthesis process works extremely well and produces powders with most of the desired characteristics. With this evolution, the program has progressively focused more on analysis and modeling to describe the nature of the process and to determine how to achieve a wide range of particle characteristics.

Process characterization has concentrated on measuring the optical absorptivities of reactant gases, analyses of emissions from the reactions and both physical and optical characterization of the reaction zone. The optical absorptivity permits the amount of laser energy absorbed by the gas molecules to be estimated. It was first thought that the emissions would permit reaction intermediates and reaction paths to be identified; but, it was soon realized that although this information could not be obtained, the optically derived flame temperatures were one of the most important process variables. Gas flow was also modeled to permit heating rates and other dependent variables to be estimated.

Resulting powders were characterized extensively. Parameters examined included size, size distribution, shape, surface area, stoichiometry, agglomeration, interparticle neck size, impurities and crystallinity. Instrumentation employed included BET, TEM, SEM, X-ray diffraction, IR spectroscopy, emission spectroscopy and wet chemistry techniques.

This program has concentrated on Si and Si_3N_4 powders. In this program, experiments with SiC powders were limited to demonstration of feasibility. A more extensive set of laser synthesis and powder characterization experiments with SiC are being carried out in other programs at M.I.T.[7,8]

A. Optical Absorptivities

The optical absorption coefficients (α) of the reactant gases determine the fraction of the incident laser power absorbed by the gas. This determines heating rates and the overall efficiency of the process, so that ultimately, the accuracy with which the particle synthesis process can be modeled depends on how precisely α is known. The effective absorption coefficient is a function of the overlap between the absorption spectrum of the reactant gases and the emission spectrum of the laser. Since the untuned high power CO_2 lasers emit almost totally at the P(20) line at 10.591 μm (944.195 cm^{-1}), it is α at this wavelength that is most important.

The low pressure absorption spectra of gases such as silane and ammonia are made up of many narrow absorption lines spaced at somewhat regular intervals. Since it is highly unlikely that a single absorption line will have exactly the same wavelength as an emission line of the laser, the difference between the positions of the two lines and their respective line widths will determine α. At low pressures ($<$ 1 torr), Doppler broadening determines the width of the absorption line. The Doppler width, Δv_D, can be calculated from:[9]

$$\Delta v_D = 7.16 \times 10^{-7} \left(\frac{T}{M} \right)^{1/2} v_o \qquad (cm^{-1}) \qquad (1)$$

where T is the temperature, M the molecular weight, and v_o the line center in cm^{-1}. The absorption coefficient at position v is equal to:[9]

$$\alpha_v = \alpha_o \exp - \left[\frac{2(v-v_o)(\ell n2)^{1/2}}{\Delta v_D} \right]^2 \qquad (2)$$

where α_o is the coefficient at the line center. As the line broadens

with increasing temperature, $\alpha_\bullet$ decreases such that the integrated

absorption, S, remains constant:

$$S = \int \alpha_\nu d\nu = \left(\frac{\pi}{\ln 2}\right)^{1/2} \left(\frac{\Delta\nu_D}{2}\right)\alpha_\bullet = \text{constant} \qquad (3)$$

The absorbtivity is very small if the absorption and emission lines are more
than a few Doppler widths apart. As an example, the SiH_4 absorption line
nearest the P(20) CO_2 line[10] is at 944.213 cm^{-1}, thus the positional
difference is only 0.018 cm^{-1}. The calculated Doppler widths of this
absorption line are 2.1 x 10^{-3} cm^{-1} at 300K and 4.6 x 10^{-3} cm^{-1} at 1500K,
with the resulting values of α_ν being about 10^{-91} $\alpha_\bullet$ and 10^{-18} $\alpha_\bullet$,

respectively. From these values, it is obvious that for silane at low
pressures, any absorption will be an artifact due to rare isotopes of
silicon in the silane or forbidden energy transitions.

At system pressures above a few torr, collisions between the gas
molecules cause the absorption line widths to broaden. For many gases, this
broadening, $\Delta\nu_L$, has been found empirically to be proportional to the system
pressure:[9]

$$\Delta\nu_L = kP \qquad (4)$$

In the presence of pressure broadening, and when $\Delta\nu_L \gg \Delta\nu_D$, the
absorptivity can be approximated by:[9]

$$\alpha_\nu = \left[\alpha_0\left(\frac{1}{\pi\ln 2}\right)^{1/2}\frac{\Delta\nu_D}{\Delta\nu_L}\right]\left[\frac{1}{1 + \left(\frac{2(\nu - \nu_0)}{\Delta\nu_L}\right)^2}\right] \qquad (5)$$

The first term in brackets is the absorption at the peak; it is inversely
proportional to pressure. When $(\nu - \nu_0) = \Delta\nu_L/2$, the absorptivity at

position ν has its maximum value:

$$\alpha_{max} = \frac{\alpha_o}{4}\left(\frac{1}{\pi \ell n 2}\right)^{1/2}\frac{\nu_D}{(\nu - \nu_o)} \tag{6}$$

In the case of silane and for 10.6 μm, $\alpha_{max} = 0.01$ α_o at 300K according to Equation 6.

The intense laser radiation can change the absorptivity of the gas. At room temperature virtually all of the gas molecules are in the ground vibrational level, and they are distributed among approximately twenty rotational levels according to a Boltzmann distribution. As the gas is heated, some rotational levels experience an increase in population, and others experience a loss. Since only one rotational level of the ground vibrational level absorbs the laser radiation, changes in the gas temperatures will change the number of molecules that are capable of absorbing the monochromatic light. Although the exact rotational quantum number of the absorbing level in silane is not known, it is apparently higher than the room temperature average. An increase in temperature will therefore increase the silane absorptivity.

Whenever an infrared photon is absorbed, a molecule makes a transition to an excited vibrational level. Collisions soon return this molecule to the ground state, but in the mean time it is unable to absorb another photon unless a transition between the first and second excited vibrational levels is also resonant with the 10.6 μm radiation. Since the spacing between excited vibrational levels in silane is unknown, it is impossible to predict whether a large degree of vibrational excitation will increase or decrease the absorptivity of silane. This will have to be experimentally determined.

The optical absorptivities of SiH_4 and NH_3 gases were measured[3] for 33 lines emitted from a CO_2 laser with wavelengths ranging from 10·137 to 10·812 μm. These results, Table 1, indicate that the highest overall absorbtivity is by SiH_4 for the P(20) line. For this line, NH_3 has a moderately high absorptivity. There are other lines where both gases have essentially equal and acceptably high absorptivities (P(34) and P(38) lines)

TABLE 1

Absorption Coefficients (atm-cm)$^{-1}$ for the 10.6 μm (00°1-10°0) Band of the CO_2 Laser.

Spectral Line	Wave Length (μm)	Absorption Coefficients (atm^{-1} cm^{-1})	
		NH_3	SiH_4
R(38)	10.137	.044 A	1.68 C
R(36)	10.148	not measured	.27 C
R(34)	10.159	.0072A	(small) C
R(32)	10.171	.0065A	.19 C
R(30)	10.182	.047 A	.96 C
R(28)	10.195	.057 A	2.68 C
R(26)	10.207	.059 A	.70 C
R(24)	10.220	.056 A	.31 C
R(22)	10.233	.071 A	1.36 C
R(20)	10.247	.12 A	1.61 C
R(18)	10.260	.22 B	.87 C
R(16)	10.275	7.25 B	1.14 C
R(14)	10.289	.24 A	.79 C
R(12)	10.304	.47 E	.23 C
R(10)	10.319	.50 A	.34 C
R (8)	10.333	21.5 E	.007C

Spectral Line	Wave Length (μm)	Absorption Coefficients (atm^{-1} cm^{-1})	
		NH_3	SiH_4
P (8)	10.476	.35 A	2.70 C
P(10)	10.494	.16 A	.50 C
P(12)	10.513	.65 A	3.95 C
P(14)	10.532	.83 A	1.94 C
P(16)	10.551	.41 A	.96 C
P(18)	10.571	.18 A	11.8 C
P(20)	10.591	.30 A	(43.0) C
			12.9 D
P(22)	10.611	.13 A	(28.9) C
			8.17 D
P(24)	10.632	.16 A	(34.5) C
			10.7 D
P(26)	10.653	.42 A	7.42 C
P(28)	10.675	.35 A	(29.4) C
			8.94 D
P(30)	10.696	.87 A	6.46 C
P(32)	10.719	13.6 E	3.79 C
P(34)	10.741	3.5 A	5.01 C
P(36)	10.765	1.8 E	18.1 C
P(38)	10.788	1.02 E	1.05 C
P(40)	10.812	1.0 A	

Conditions:
A: 136 ± 2 torr 10 cm cell
B: 130 ± 2 torr 1.7 cm cell
C: 53 ± 1 torr 1.7 cm cell
D: 11 ± 1 torr 1.7 cm cell
E: 25 ± 1 torr 1.7 cm cell
( ) denote uncertainty in precision of results

19

and others where NH_3 has the highest absorptivity (R(12) and R(18) lines). It was concluded we should proceed using the P(20) line because of the high SiH_4 absorptivity and untuned CO_2 lasers emit on this line.[2,3]

More precise absorptivities were measured[2,3] for SiH_4 and NH_3 gases as a function of gas pressure and laser intensity. These results are given in Figures 6 and 7. These data show that α_{SiH_4} is strongly dependent on pressure and laser intensity, perhaps as a temperature effect. The α_{NH_3} is nearly independent of pressure and intensity.

The strong dependence on pressure is expected based on Equation 5 for α_v. A curve for α_v calculated from Equation 5 using the experimental peak of $\alpha_{SiH_4} = 60$ $(atm \cdot cm)^{-1}$ at 85 torr is also included in Figure 6. Agreement between the experimental and calculated absorptivities is good up to the peak, but the experimental absorptivity falls off more rapidly than expected. This may be due to a small amount of non-P(20) emission from the laser that is not absorbed by the silane. If so, a repeat of the low intensity measurement with a still shorter cell will reveal the true high pressure absorption.

B. Emissions from the Reaction Zone

1. General Characteristics

The relatively bright stable visible emission from the reaction flame suggested that this nonintrusive analyses could be used to characterize the laser induced reactions as has been done with other types of more conventional flames.[5] In principle, the emitted spectra should provide a spacial description of chemical species and temperature in the reaction zone.

Synthesis of Si by pyrolysis of SiH_4 and synthesis of Si_3N_4 from various reactants have been studied by many scientists,[11-17] yet no definitive model for these reactions has emerged for conventional process conditions. Most authors suggest that the pyrolysis reaction occurs by a step-by-step reaction[11,13] involving a Si_2H_6 radical. High molecular

20
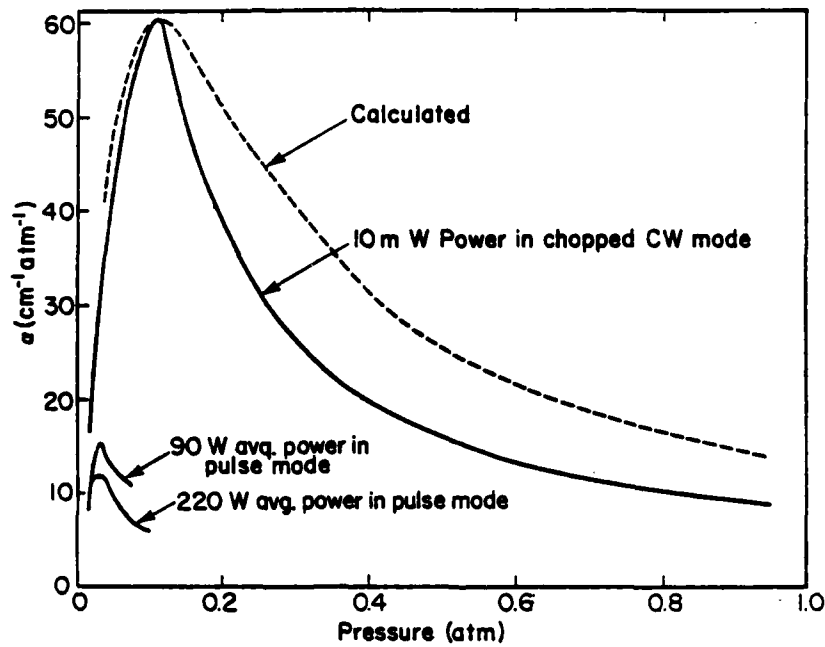
Figure 6. The absorption coefficient of SiH_4 as a function of pressure for the P(20) CO_2 laser line.
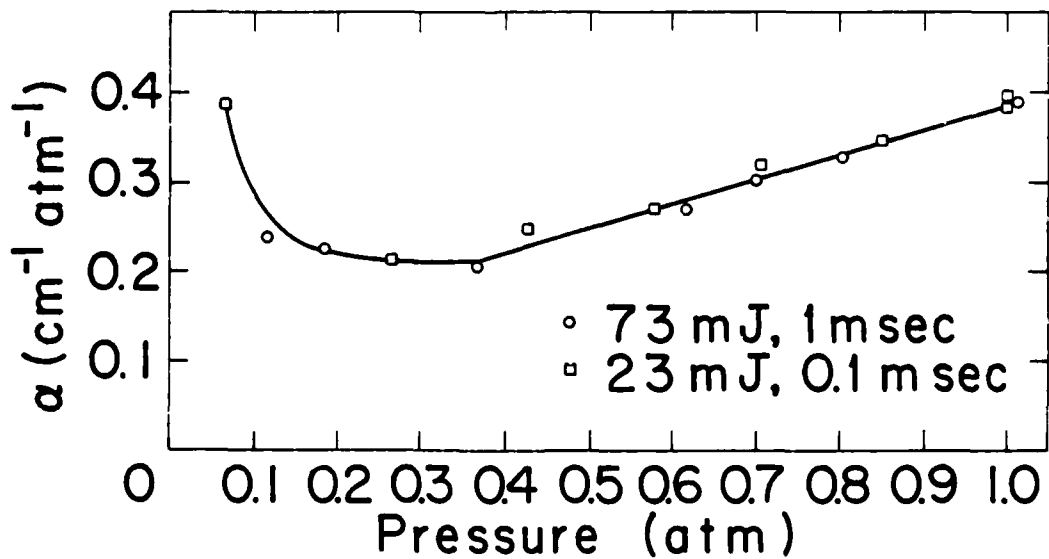
Figure 7. The absorption coefficients of NH_3 as a function of pressure for the P(18) and P(20) CO_2 laser lines.

weight hydrides ultimately condense to pure silicon, simultaneously giving off H_2. It is also suggested[15] that Si_3N_4 is formed by Si and N bearing polymers condensing to form the nitride.

There are several reasons to believe that the descriptions in the existing literature do not apply directly to this reaction. The most obvious reason is the lack of an accepted description of even, slow, highly controlled reactions. In hydrocarbon flames, it has been found that reaction schemes deduced from measurements on slow reaction (combustion) proceses cannot be applied to propagating flames with any sense of certainty.[5] The slow reactions are usually dominated by catalytic and other surface effects. Also, the reaction temperature in the flame is usually much higher than those measured in slow or spontaneous ignition experiments.[5] The laser heat source itself might also be suspected of affecting the reaction by various resonance effects in the molecules. For these reasons, the prior work on the chemistry of the reaction is useful background, but it is not directly applicable to the laser heated synthesis process. The temperature distribution is obviously unique to this process.

Two sources of emissions can be expected. Banded or line emissions can be expected from reaction intermediates and reaction products. Of the possibilities, SiH_2,[18] SiH_1,[19] NH_2,[5,20] and H_2,[19] have transitions which emit in the visible and ultra violet. The optical characteristics of the intermediate SiH_3 have not been studied because it is apparently too reactive. Continuous thermal emission can also be expected from hot Si and Si_3N_4 particles, whose wavelength dependence is determined by the high temperature real and imaginary indices of the particles, as well as size effects. The determination of local chemistry and temperature requires the identification, characterization and modeling of each source of emitted light.

Three spectrometers have been employed to characterize the emission from the reaction flame for wavelengths between 4000 and 8500 Å. Moderately high resolution (5 Å) spectra were measured with a 1/4 m Jarrell-Ash monochrometer coupled to an RCA C5 3050 photomultiplier. This apparatus was calibrated against a tungsten lamp to permit absolute intensities to be

measured over the wavelength range. Higher resolution measurements (0.5 Å) were made with a 1 m SPEX double monochrometer. Both instruments employed a PAR lock-in amplifier which yields a dynamic range of 10^4. Lower resolution (30 Å) measurements were also made with an optical multichannel analyzer (OMA) instrument which analyzes the entire spectrum simultaneously. The time-varient intensities of the flame make it extremely tedious to characterize the spectra using either of the monochrometer instruments with a confidence level which is superior to that of the lower resolution multichannel analyzer. The high resolution instrument was used to determine whether the broad spectrographic features consisted of a "forest" of lines that were spaced closer than resolution limits of other instruments.

Figure 8 illustrates spectra emitted from CO_2 laser heated SiH_4, NH_3, and NH_3/SiH_4 gases under typical process conditions. These specific results obtained wth 1/4 m Jarrell-Ash monochrometer at the denoted wavelengths. Equivalent results were also obtained with the multichannel analyzer instrument. At pressure levels of approximately 0.2 atmospheres or greater, the emitted spectra exhibited no spectral features. Overall, the intensity of the NH_3 + SiH_4 flame is approximately 1000 times higher than the NH_3 flame and 20-50 times higher than the SiH_4 flame. The NH_3 flame is fundamentally different from the other two since the latter produce hot particulate reaction products which contribute to the emission. Products from the NH_3 result only from gaseous reactant, intermediate and product species.

At low pressure, (P < 0.07 atm) band emissions were evident in SiH_4 and NH_3 + SiH_4 flames with the multichannel instrument for wavelengths between 0.4 and 0.5 μm. Typical flame emissions are shown in Figures 9 and 10. These peaks disappear completely into the continuous thermal emission by a pressure level of 80 torr (0.1 atm). Broad bands are also evident in the NH_3 flame at these low pressures. They persist to the higher pressures with progressive broadening and diminishing height relative to the background, to the point where the emission appears effectively continuous.

The weak peaks observed with the SiH_4 and NH_3 + SiH_4 flames have not been identified with any certainty. The high resolution spectrometer has shown that, within a resolution of 0.5 Å, these peaks do not consist of a

23
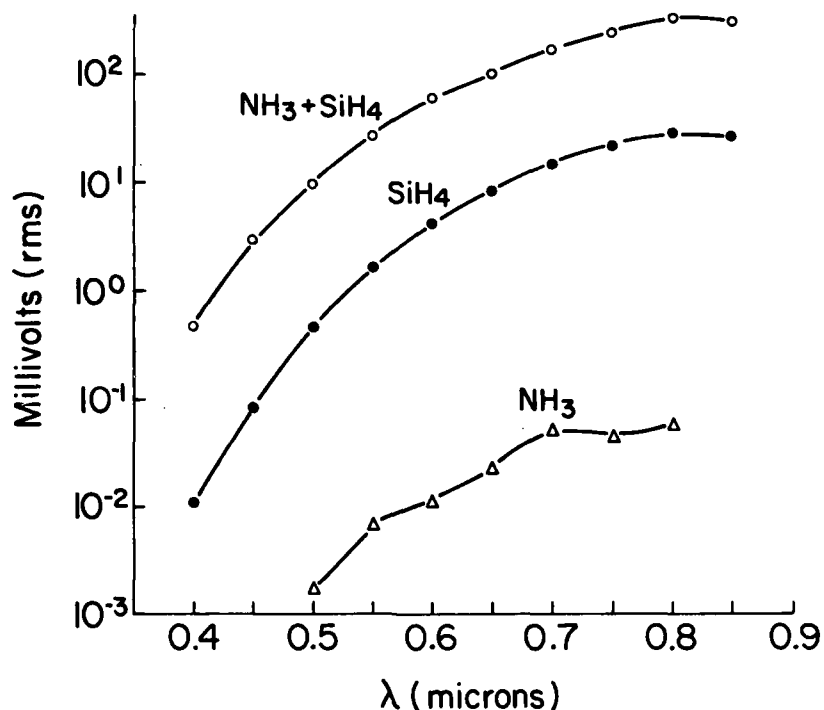
Figure 8. Emission spectra from reaction flame measured with a Jarrell-Ash monochrometer. Cell pressure was 0.2 atm and gas flow rates of SiH_4 and NH_3 were 11 cm^3/min and 110 cm^3/min respectively. Millivolt output from PMT amplifier was corrected for sensitivity of PMT at a particular wavelength. Thus values are proportional to intensity.

multitude of closely spaced lines. The band structure observed with the NH_3 flame is probably the ammonia α bands reported for NH_3-O_2 and CH_4-NO_2 flames.[21] No NH emission was detected although the multichannel analyzer is less sensitive in this region ($\lambda = 3360$ Å) and a strong thermally emitted background may have obscured it.

These results indicated that it will be very difficult to extract information about the chemical species in the flame under normal synthesis conditions because of the dominance of the emissions by the hot particles. Pressure and temperature broadening effects also contribute to the masking of this information. Lower pressure reactions must be studied to identify species which are present under those conditions and their existence verified at the higher pressures by appropriate modeling and analyses.
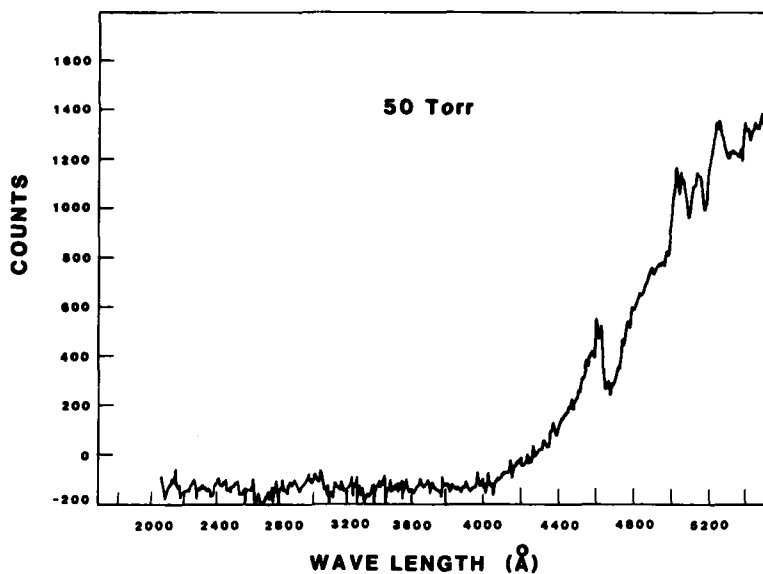
Figure 9. Continuous spectra from a SiH$_4$ reaction flame at 50 torr using a
flow rate of 11 cm^3/min. The spectra was measured with a
PAR OMA II multichannel analyzer. The abscissa is given as the
difference in counts between a scan of a flame and a background
scan.
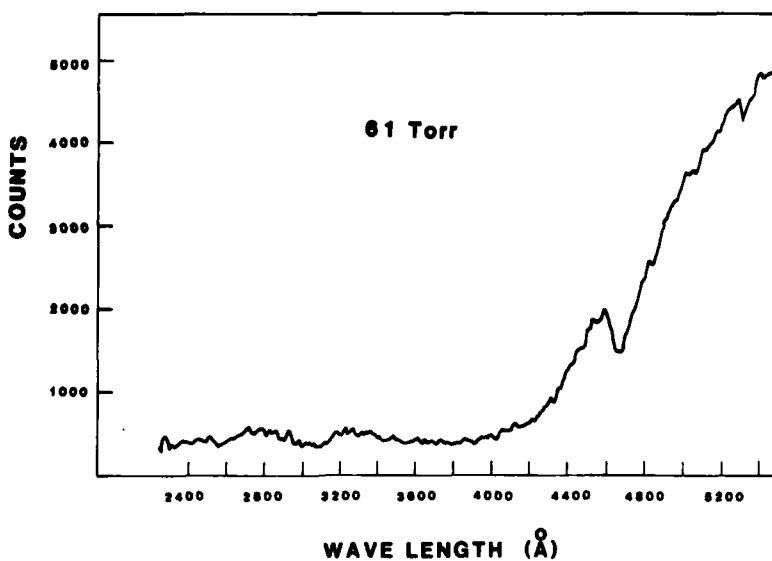
Figure 10. Continuous spectra from a SiH$_4$ reaction flame at 61 torr using
flow rates of 11 cm^3/min. The spectra was measured with a
PAR OMA II multichannel analyzer. The abscissa is given as the
difference in counts between a scan of a flame and a background
scan.

25

2. Temperature Measurements

a. Analytical and Measurement Techniques

Spectroscopic studies intended to determine the particle temperatures within the reaction flame are important both for modeling the reaction process and for providing a means of improving process control.

The relationship between the intensity of emitted radiation at a given wavelength and the temperature of the radiating body is described by Wein's approximation of Planck's law:[22]

$$I_\lambda = \frac{C_1 \epsilon_\lambda \; \exp(-C_2/\lambda T)}{\lambda^5} \; d\lambda d\Omega \qquad (7)$$

where ϵ_λ is the emissivity at wavelength λ, C_1 and C_2 are known radiation constants, and $d\lambda$ and $d\Omega$ are the wavelength and solid angle intervals of the detector. By combining the constants C_1, $d\lambda$, and $d\Omega$ into a new constant C' and rearranging, one obtains:

$$\ell n(I_\lambda \lambda^5) = \frac{-C_2}{\lambda T} + \ell n \; \epsilon_\lambda + \ell n \; C' \; . \qquad (8)$$

If ϵ_λ is independent of λ, then a plot of $\ell n(I_\lambda \lambda^5)$ versus $1/\lambda$ will yield a straight line with a slope of $-C_2/T$, thus permitting the temperature to be calculated. If ϵ_λ is dependent on λ, the functional relationship between these parameters must be determined before the absolute temperature can be calculated.

The emissivity of a flame containing small hot particles can be separated into two parts: the electronic emissivity, $\epsilon_{\lambda e}$, which is dependent on the chemical composition of the particles, and the aerosol emissivity, $\epsilon_{\lambda a}$, which is dependent on the size and the density of the

particles in the flame. Kirchhoff's law states that at radiative equilibrium, the emissivity of a body is equal to its absorptivity. The absorptivity, and thus the emissivity, of silicon increases very strongly from the red to the blue end of the spectrum.[23] The intensity of the flame will therefore be higher in blue than in red compared with that expected for an opaque black body at the same temperature. Thus, the color temperature of the flame, which depends on the distribution of intensity with wavelength rather than the absolute intensity at each wavelength, will be higher than its true temperature. A similar effect also results because the radiating particles are smaller than the wavelength of the light they are emitting. The absorption efficiency of a small particle can be derived from Mie scattering theory.[6] For small particles of a uniformly absorbing (black) material, the emissivity is proportional to $1/\lambda$; that is, ε_{λ_a} is greater at the blue end than at the red end of the spectrum.

It should be expected, therefore, that the relative emissivity of the SiH_4 flame will fall somewhere between following a $1/\lambda$ dependence and following the room temperature silicon particle absorption spectrum. Calculating the temperature from the spectral emittance of the flame with the first dependence results in the maximum calculated temperature and the second results in the minimum calculated temperature. Whatever the dependence of ε_{λ_e} with λ, it should remain constant as long as silicon is the dominant emitter. Since stoichiometric silicon nitride is transparent in the visible region of the spectrum, the silane-ammonia flame emittance probably will be due largely to the excess silicon in the particles. The temperature measurements for both silane flames and silane-ammonia flames therefore have been evaluated using the silicon emissivity corrections. The magnitude of the aerosol emissivity, ε_{λ_a}, will depend on the size of the particles and on their density in the flame as well as the wavelength. It will therefore depend on those reaction conditions that affect particle size and density such as mass flow rate and total pressure.

Measurements of the silicon particle absorption coefficient were made at room temperature using a well dispersed suspension of silicon powder in n-propanol. In these measurements, the particles were well separated and

expected to interact with light through Rayleigh scattering. It was assumed that light scattering is small compared to absorption and that absoprtion was not strongly affected by the n-propanol medium (although the absorption of n-propanol per se was subtracted out, Rayleigh scattering also considers the relative index of refraction and extinction coefficient between the particles and the media). The results of this measurement were used to calculate the electronic emissivity.

Temperature measurements of the reaction flame involve two related but distinct techniques. The first measures the emittance of the radiation from the flame at a single wavelength. The second measures the relative emittances of the flame at several wavelengths. The first technique requires a calibrated detector, and the detector constants, $d\lambda$ and $d\Omega$. An optical pyrometer avoids these specific problems by superimposing the image of the body on a heated filament. The temperature of the body is determined when it and the filament have equal intensities as observed by eye. ϵ_λ must

be determined to permit calculation of the true temperature. Without this emissivity correction, the temperature measured with the pyrometer underestimates the true flame temperature by as much as several hundred degrees. This is because this technique assumes ϵ_λ is equal to 1 at the

wavelength used, when, in fact, it is always substantially less than 1 due to the combined effects of electronic and aerosol emissivities.

The second technique involves measuring the relative emittance of the flame at several wavelengths. Only the relative emissivities and a detector calibrated with respect to wavelength are needed since the ratios of the emittances at different wavelengths are measured. We have made this second type of temperature measurement using three types of instrumentation.

The spectra[2,3] of silane and silane-ammonia flames were recorded with a monochromator-photomultiplier (PMT) combination. While each individual measurement can be made arbitrarily accurate, the flame intensity varies substantially in the thirty minute period required to measure the spectra. This method is too slow for routine temperature monitoring. An optical multichannel analyzer (OMA) provides a much more rapid means of collecting the flame spectrum. The OMA II disperses the flame spectrum onto a vidicon,

where the entire spectrum is recorded simultaneously, so any flame
fluctuations affect all wavelengths equally. However, the red edge of the
spectrum is limited by the vidicon sensitivity to around 0.650 µm, and the
complete system is too expensive to be used as a dedicated temperature
monitor.

The combined limitations of the PMT–monochromator system and of the
optical multichannel analyzer led to the development of a PMT-interference
filter detector system that allows routine monitoring of the reaction flame
temperature. The photomultiplier is an RCA C31034 QUANTACON which is
sensitive to 0.850 µm. A rotating wheel holding interference filters which
transmit at 0.449 µm, 0.548 µm, 0.658 µm and 0.801 µm is mounted on the
front of the PMT tube housing. This permits rapid monitoring of the flame
at these four wavelengths by observation of the PMT signal on a digital
voltmeter or a chart recorder. Typical data from three silane–ammonia
flames are presented in Figure 11. As with the other measurement techniques
and materials, near linear plots result when graphed in according to
Equation 8.
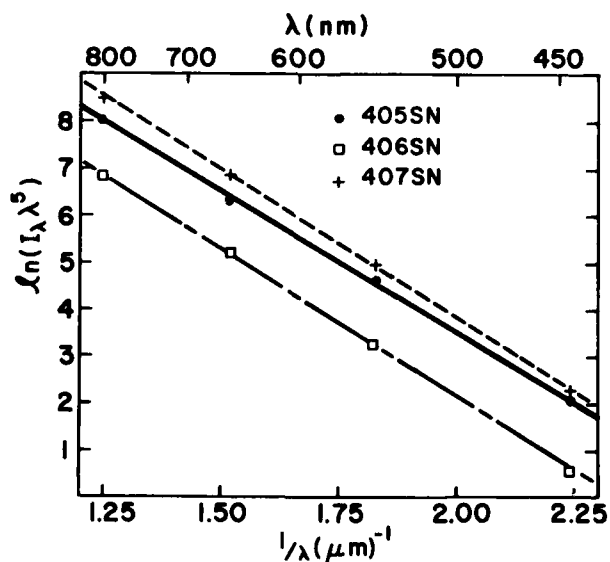
Figure 11. Emission spectra (plotted as $\ell n(I_\lambda \lambda^5)$ vs. $1/\lambda$) of reaction flame
measured with a photomultiplier–interference filter detector.

b. Results

An extensive study was conducted to determine the effect of reaction
conditions on flame temperature. This set of experiments compared the
accuracy of temperatures calculated by various means and correlated the
effect of temperature with particle characteristics. The following
parameters were systematically varied: pressure, gas flow rates, laser
intensity, and argon dilution of the reactant gas stream. For all runs, the
temperature was measured with both optical pyrometry and the PMT-
interference filter technique. The majority of these experiments were
carried out with SiH_4 flames and a few with NH_3-SiH_4 flames.

Figure 12 shows the effect of reactant gas flow rate on temperature for
Si synthesis runs made with a 150 W unfocused CO_2 laser beam at a total
pressure of 0.2 atm. The pyrometry temperature is uncorrected for
emissivity effects thus indicating a lower than actual temperature. The
PMT-filter temperature, calculated assuming a Si emissivity dependence
measured at room temperature, is lower than the pyrometer temperature except
at the lowest flow rates. This result demonstrates that this emissivity
dependence is not valid for elevated temperatures. The cross-over between
the pyrometer temperature and PMT-interference filter temperature (assuming
$\varepsilon = \varepsilon_{Si,RT}$) is probably due to a decrease in aerosol emissivity at low flow
rates, since the pyrometer temperature is dependent on particle size and
concentration. The large amount of variation resulted in the measured
temperature for a flame at a flow rate of 13 cm^3/min because of the inherent
flame instability with those run conditions. The maximum PMT-interference
filter temperatures, assuming a $1/\lambda$ emissivity dependence, for runs
performed with flow rates of 38 cm^3/min and 60 cm^3/min are greater than
1410°C, the melting point of Si. If this is a true temperature and the
particles were actually at this temperature long enough to melt or they
originally formed as liquid droplets, the internal structure of these
particles should be different from those formed at temperatures below the
melting point. Although the three temperature estimates differ

30

quantitatively, they all exhibit the same qualitative features. All three exhibit a maximum temperature at the same SiH_4 rate.

Figure 13 shows the results of temperature measurements for silicon powder produced at 0.6 atm. The temperature again goes through a maximum as the flow rate was increased, although the variation in temperature with flow rate is not as large as observed for runs made at 0.2 atm. The pyrometer temperature was nearly equivalent to the temperature calculated from the PMT-interference filter data assuming an emissivity dependence of $1/\lambda$. The convergence results because the aerosol emissivity increases as the silicon density within the flame increases.

When the flame emissivity throughout the visible region becomes close to one, the techniques give equal and equally accurate results. Under conditions where the emissivity is small, large corrections to the pyrometer measurements are required. However, since it is also impossible under these conditions to choose between a $1/\lambda$ or a $\alpha_{Si,RT}$ dependence for ϵ, the PMT-interference filter method is also imprecise. Some direct measurement of the flame emissivity will therefore be required before precise temperature measurements can be reported.

Figure 14 shows the effect of laser intensity on the reaction temperature. All runs were performed at a pressure of 0.35 atm, a silane flow rate of 66 cm^3/min and without dilution of the reactant gas stream. As expected, an increase in intensity resulted in a higher reaction temperature. Run 645S with a focused laser beam is also included on this curve. It was performed with identical reaction conditions as the other runs except a 170 W beam was focused to a spot size of approximately 2 mm. This should result in a laser power intensity that is almost an order of magnitude greater than that for an unfocused 170 W laser beam. The reaction temperature increased slightly with the focused beam but not to the extent expected by a tenfold increase in laser intensity, suggesting an upper temperature limit exists for the pyrolysis reaction. These results also show the temperature indicated for the focused beam run to be greater than the melting point of Si.

31
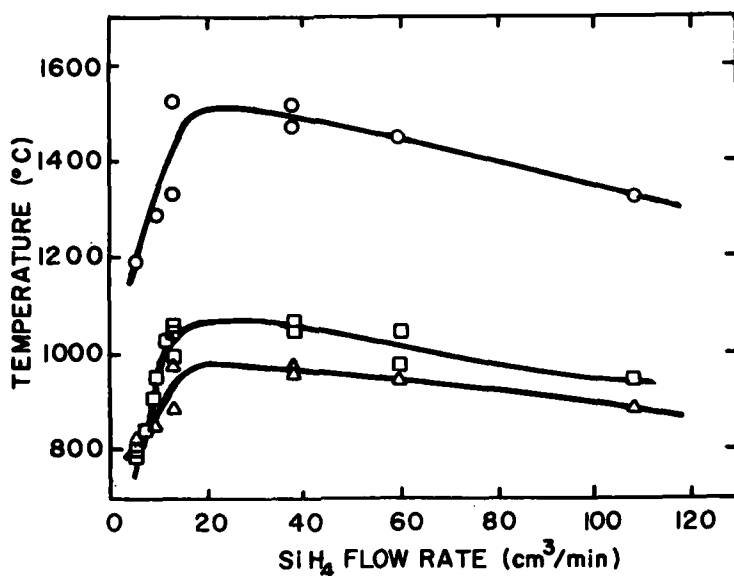
Figure 12. The effect of SiH_4 flow rate on the silicon synthesis reaction
temperature. O is calculated temperature from PMT-interference
filter technique assuming $\varepsilon = 1/\lambda$. □ is uncorrected pyrometric
temperature. Δ is calculated temperature from PMT-interference
filter technique assuming $\varepsilon = \varepsilon_{RT,Si}$ (reaction cell pressure of
0.20 atm.)
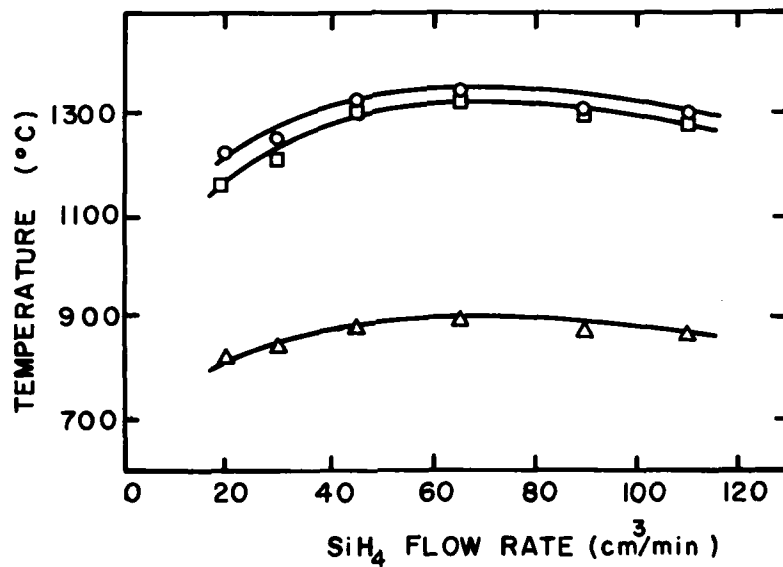
Figure 13. The effect of SiH_4 flow rate on the silicon synthesis reaction
temperature. O is calculated temperature from PMT-interference
filter technique assuming $\varepsilon = 1/\lambda$. □ is uncorrected pyrometric
temperature. Δ is calculated temperature from PMT-interference
filter technique assuming $\varepsilon = \varepsilon_{RT,Si}$ (reaction cell pressure of
0.60 atm.)

32

Figure 15 shows the effect of diluting the reactant gas stream with Ar on the reaction zone temperature. The addition of a low heat capacity gas, such as Ar, makes it easier to raise the silane gas to a temperature level sufficient to produce pyrolysis but, Ar is transparent to the CO_2 laser radiation and therefore acts as an optical dilutant, lowering the overall absorptivity of the reactant gas mixture. Thus, the overall reaction temperature will be determined by the net effect of these two competing processes. Figure 15 shows that the reaction temperature remained essentially constant up to a dilution of about 35 mole % Ar, and then decreased slightly with further dilution of the reactant gas stream. The uncorrected pyrometer temperature and the temperature calculated from the PMT-interference filter technique assuming $\varepsilon = \varepsilon_{Si,RT}$ intersected as the gas stream was increasingly diluted. This was expected since diluting the reactant gas stream produces a lower aerosol emissivity.

Similar temperature measurements were made of SiH_4-NH_3 flames. As with the SiH_4 flames the temperature indicated by optical pyrometer was lower than that calculated from specteral intensity measurements using $\varepsilon_\lambda = 1/\lambda$ dependence; e.g., 1230°C versus 1895°C. Temperatures caluclated using $\varepsilon_\lambda = \varepsilon_{Si,RT}$ were slightly higher than measured by pyrometer; e.g., 1239°C versus 1230°C.

Of the three techniques employed, we conclude that the calculated temperatures based on four color specteral intensity measurements and the $\varepsilon_\lambda = 1/\lambda$ approximation are the only ones which are accurate with respect to their relative levels. Sufficient information has not yet been derived to give a measure of their absolute accuracy but they are probably somewhat high for Si. As will be discussed in following sections, no unusual crystallographic or microstructural differences were evident between Si powders synthesized with temperatures above or below the melting point.

C. Effect of Process Variables on Powder Characteristics

One of the ultimate objectives of this program is to develop an understanding of the relationships, based on equilibrium thermodynamics and kinetics, between the laser heated gas phase reaction and the resulting

33
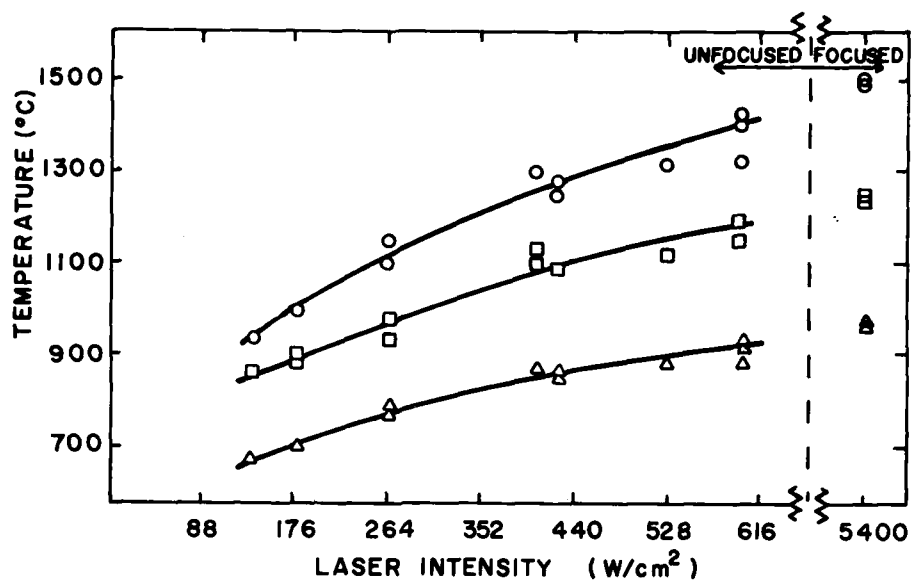
Figure 14. The effect of laser intensity on the silicon synthesis reaction temperature. O is calculated temperature from PMT-interference filter technique assuming $\varepsilon = 1/\lambda$. □ is uncorrected pyrometric temperature. Δ is calculated temperature from PMT-interference filter technique assuming $\varepsilon = \varepsilon_{RT,Si}$.
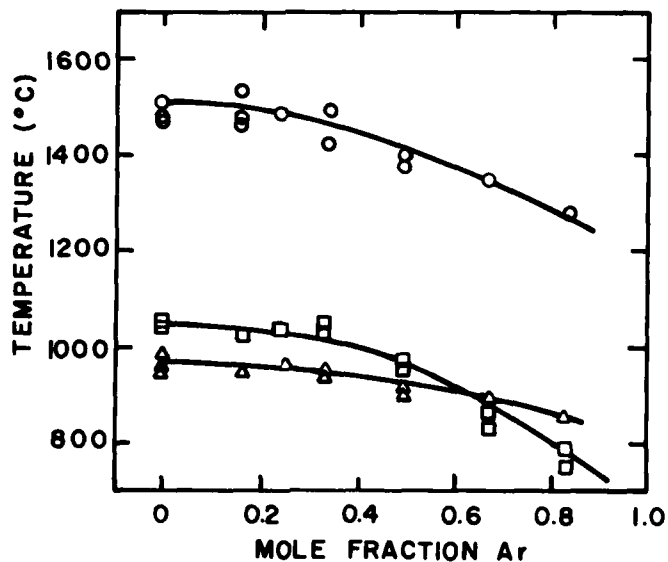
Figure 15. The effect of reactant gas dilution on the silicon synthesis temperature. O is calculated temperature from PMT-interference filter technique assuming $\varepsilon = 1/\lambda$. □ is uncorrected pyrometric temperature. Δ is calculated temperature from PMT-interference filter technique assuming $\varepsilon = \varepsilon_{RT,Si}$.

powder characteristics. The effects that process variables such as laser intensity, cell pressure, gas velocity and gas mixture, have on the reaction and resulting powder characteristics were studied for Si and Si_3N_4 powder synthesis. The process characteristics are summarized in Appendix I and the resulting powder characteristics are summarized in Appendix II. It is anticipated that the results of these studies along with an improved understanding of the reaction temperature and reactant gas absorptivities and velocities ultimately will permit a quantitative description of the synthesis process based on classical homogeneous nucleation and growth theory.

1. Silicon Powders

a. General Characteristics

The characteristics of the Si powders essentially are identical with those sought. They are small, spherically shaped, uniform in size and pure. A bright field TEM photomicrograph of a typical powder is shown in Figure 16. This illustrates that the powders were observed in chain-like agglomerates. The results of our studying the causes for agglomeration and the strength of the interparticle necks are discussed later in this report; however, we believe that the particles are not strongly bonded to one another.

The efficiency with which the SiH_4 gas is converted to powder ranged from 80-100%. The conversion efficiency exhibited no systematic dependence on process variables within the range examined.

The BET equivalent spherical diameter and the diameter measured from TEM micrographs have always been nearly equal as is illustrated in Figure 17. These results indicate that the particles have smooth surfaces, no porosity accessible to the surface, a relatively narrow size distribution, and nearly spherical shapes. Powder densities, measured by the pycnometry, indicated there was also no closed porosity.

Spectrographic analyses (Table 2) show that the powders are predominantly pure Si with the total cation impurities typically less than

TABLE 2

Chemical Analyses of Silicon Powders

Sample	Summary of Comparitive Spectrographic Analyses (ppm)												Other Analyses (wt %)				
	Al	Ag	Ba	B	Ca	Cu	Fe	Mg	Ni	Pb	Sn	Ti	O_2	C	Cl	S	F
01S	10	0	0	0	0	10	0	0	0	0	0	0	0.67	-	-	-	-
027S	30	0	0	30	20	10	100	5	20	0	10	0	0.22	-	-	-	-
033S	-	-	-	-	-	-	-	-	-	-	-	-	2.00	-	-	-	-
101S	-	-	-	-	-	-	-	-	-	-	-	-	0.14	-	-	-	-
102S	-	-	-	-	-	-	-	-	-	-	-	-	0.14	-	-	-	-
103S	30	3	<2	30	10	10	20	<2	0	0	<10	0	0.11	-	-	-	-
622S	-	-	-	-	-	-	-	-	-	-	-	-	<0.64	-	-	-	-
625S	30	0	0	30	20	7	30	5	5	0	<10	0	0.28	-	-	-	-
628S	20	0	0	0	30	10	10	3	3	0	10	0	-	-	-	-	-
631S	3	0	0	0	0.3	0	1	0	0	0	0	0	0.70	0.10	0.095	0	0
632S	3	0	0	0	0.3	0	1	0	0	0	0	0	0.68	0.03	0.140	0	0

200 ppm. The oxygen content is generally less than 1.0% by weight and some runs have produced powder with an O_2 concentration as low as 0.05 wt. %. The purity of the resulting powders varies somewhat from run to run, but it does not seem to be dependent on the nominal run conditions. Rather, it is related to specific experimental procedures such as outgassing time, vacuum tightness of the cell and post-production handling of the powder.

Except when synthesized under very low laser intensities, the Si powders were crystalline to both X-ray and electron diffraction. The crystallite size was determined from X-ray diffraction line broadening of the Si (220) peak at 47.34° using Cu-K_α radiation (λ = 1.542 Å). A large grained (> 10 μm) polycrystalline silicon specimen was used as a standard to determine the machine broadening. The Rachinger correction was used to separate the $K_{\alpha 1}$ and $K_{\alpha 2}$ peaks for both the Si powder and standard. The broadening due to small particle size was separated from the machine broadening by assuming both Guassian and Cauchy peak shapes, thereby giving

both a maximum and minimum crystallite size. In all cases, the crystallite size was substantially smaller than the BET equivalent diameter, indicating the individual particles are polycrystalline. The grain size was confirmed by bright field and dark field transmission electron microscopy. It was found that the particle size to grain size ratio depended on process conditions.

b. Powder Synthesis Experiments

i. Gas velocity

Three sets of experimental runs were performed with pure SiH_4 (Ar was used as the annuar and window gas streams) to examine the effect of reactant gas velocity. The powders were synthesized at either 0.20 atm, 0.35 atm, or 0.60 atm. The velocity was altered by changing the volumetric flow rate of SiH_4. Both the series of runs at 0.20 atm and 0.60 atm were produced with a 150 W unfocused laser beam, while the powders procuded at 0.35 atm utilized a 170 W unfocused beam. These runs are summarized in Table 3.

The effect of velocity on the reaction zone temperature was discussed in Section IIIB2b. Figures 18, 19, and 20 show the effect of gas velocity on the equivalent spherical diameter calculated from BET surface area measurements. All three curves exhibit an ascending-descending behavior with the largest sized particles resulting from reaction zones having the highest temperatures.

The X-ray line broadening results are shown in Figures 21, 22, and 23 for powders produced at 0.2 atm, 0.35 atm and 0.6 atm respectively. The results are plotted as the ratio of BET equivalent diameter to crystallite diameter versus the flow rate. Examination of Figures 12, and 21, shows that at 0.2 atm, the largest relative crystallite size (the smallest ratio of $\frac{d\ BET}{d\ X\text{-}ray}$) occured for powder produced at the highest reaction zone temperature. For powders produced at 0.35 atm, the relative crystallite size remained essentially constant ($\frac{d\ BET}{d\ X\text{-}ray,\ gaussian} = 3.0$) and independent of both the flow rate and the reaction zone temperature except at the

37

Figure 16. TEM photomicrograph of Si powders. Lot 634S. (Bar 500 Å)
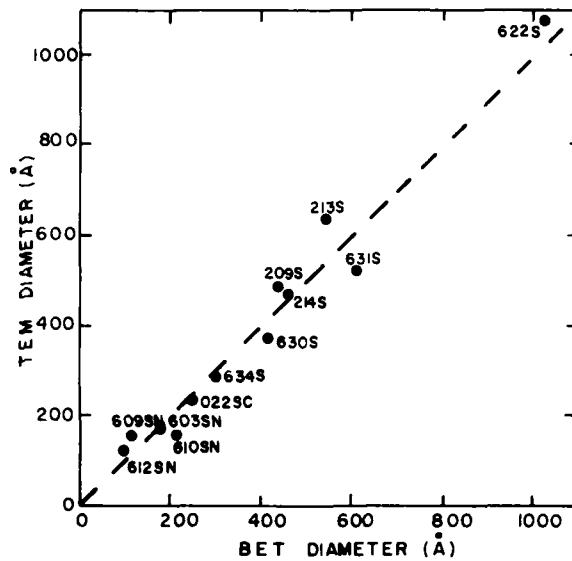
Figure 17. Comparison of BET equivalent spherical diameter and TEM measured diameter.
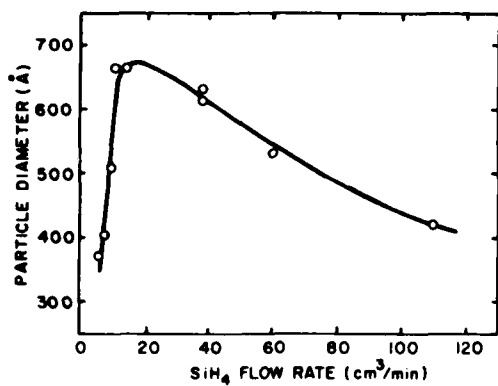
Figure 18. The effect of SiH_4 flow rate on the resulting Si powder particle size (reaction cell pressure of 0.2 atm).
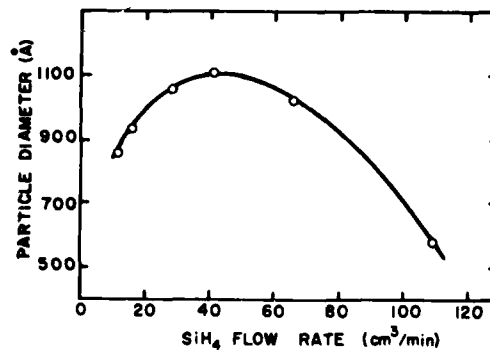
Figure 19. The effect of SiH_4 flow rate on the resulting Si powder particle size (reaction cell pressure of 0.35 atm).
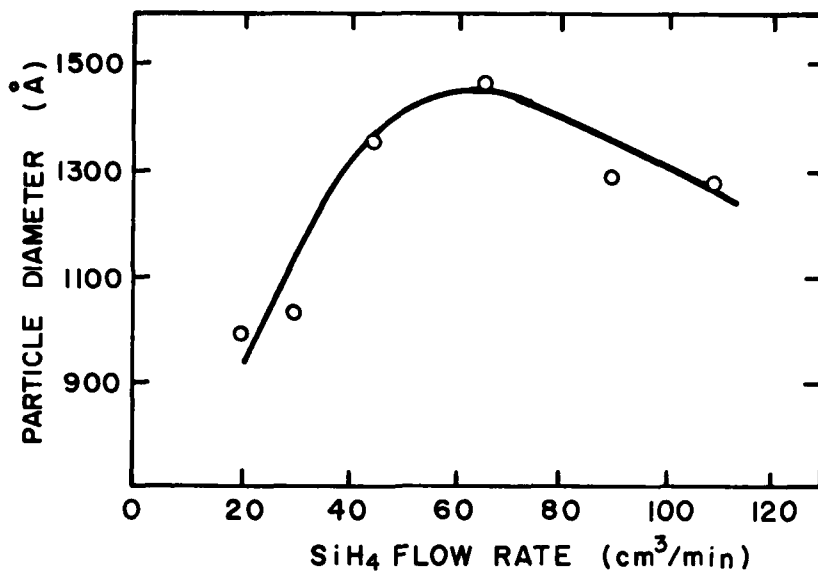
Figure 20. The effect of SiH₄ flow rate on the resulting Si powder particle
size (reaction cell pressure of 0.6 atm).

Figure 21. The effect of SiH₄ flow rate on the ratio of Si particle size to
crystallite size. 0 assumes Gaussian shaped X-ray diffraction
peaks. □ assumes Cauchy shaped X-ray diffraction peaks (reaction
cell pressure of 0.2 atm).

Figure 22. The effect of SiH_4 flow rate on the ratio of Si particle size to crystallite size. 0 assumes Gaussian shaped X-ray diffraction peaks. □ assumes Cauchy shaped X-ray diffraction peaks (reaction cell pressure of 0.35 atm).

Figure 23. The effect of SiH_4 flow rate on the ratio of Si particle size to crystallite size. 0 assumes Gaussian shaped X-ray diffraction peaks. □ assumes Cauchy shaped X-ray diffraction peaks (reaction cell pressure of 0.6 atm).

TABLE 3

The Influence of Flow Rate on the Reaction Temperature
and Si Particle Characteristics.

Run	Flow Rate	Temperature $\varepsilon=RT,Si$	Pyrom	$\varepsilon=1/\lambda$	BET Equivalent Diameter (Å)	Crystallite Size (Å) Gaussian	Cauchy	$\dfrac{d_{BET}}{d_{X-ray}}$ Gaussian	Cauchy
629S*	5.5	820	810	1200	367	75	91	4.9	4.0
627S*	7.5	–	850	–	402	86	107	4.7	3.8
628S*	8.8	860	930	1290	505	127	175	4.0	2.9
625S*	11	–	1030	–	660	162	242	4.1	2.7
626S*	13	940	1030	1440	660	202	331	3.3	2.0
631S*	38	960	1055	1490	599	200	334	3.0	1.9
632S*	38	960	1045	1490	628	191	305	3.3	2.1
653S*	38	–	–	–	612	191	305	3.2	2.0
633S*	60	950	1010	1460	526	144	206	3.7	2.6
630S*	104	890	950	1340	422	107	140	3.9	3.0
643S**	11	800	1130	1180	859	293	583	2.9	1.5
636S**	16	880	1215	1320	930	326	697	2.9	1.3
644S**	28	920	1270	1400	1059	335	723	3.2	1.5
624S**	40	910	1250	1390	1107	372	867	3.0	1.3
622S**	66	880	1055	1310	1027	348	721	3.0	1.4
623S**	109	830	1040	1230	583	171	261	3.4	2.2
649S**	109	840	1100	1250	583	197	317	3.0	1.8
659S**	19.5	830	1200	1230	945	333	698	2.8	1.4
652S***	30	850	1220	1260	1033	329	712	3.1	1.5
656S***	45	890	1340	1350	1469	414	1039	3.5	1.4
650S***	66	890	1340	1350	1469	414	1039	3.5	1.4
651S***	90	880	1290	1320	1290	405	1005	3.2	1.3
657S***	110	870	1280	1300	1284	353	794	3.6	1.6

* For each run: Pressure = 0.20 atm, Intensity = 531 W/cm^2
** For each run: Pressure = 0.35 atm, Intensity = 601 W/cm^2
*** For each run: Pressure = 0.60 atm, Intensity = 531 W/cm^2

highest flow rate, the ratio $\frac{d\ BET}{d\ X\text{-ray}}$ appeared to increase slightly. At 0.60 atm, the ratio $\frac{d\ BET}{d\ X\text{-ray}}$ was constant over the entire flow range. These results will be discussed further in Section IIIClciii.

Three runs (631S, 632S and 653S) were performed using identical process conditions to examine the reproducibility of the laser synthesis process. The reaction zone and resulting powder characteristics are summarized in Appendicies I and II. The reaction temperatures, conversion efficiencies, the equivalent size from BET surface area measurements and the crystallite size measured by X-ray line broadening are nearly identical for the three runs. These results show that the process is easily controllable and can produce powders with similar characteristics from run to run. It should be noted that many of the earlier Si powders were made with SiH_4 flow rates of about 10 cc/min. It is evident from Figures 12 and 18 that, in this regime, the reaction zone and particle characteristics exhibit large variations with small changes in flow rate. The differences previously reported[3] between powders synthesized with these lower, nominally identical, SiH_4 flow rates are probably attributable to inaccuracies in the measurement of the reactant gas flow rates.

ii. Laser Intensity

Several runs in which all process variables were held constant except laser intensity are summarized in Table 4. All these runs used an unfocused beam with a beam diameter of 0.6 cm except run 645S where the 170 W laser beam was focused to a spot size of 0.2 cm. The average intensity for the unfocused beam runs ranges from 134 W/cm^2 (658S) to 601 W/cm^2 (622S). The effect of intensity on the reaction zone temperature was summarized in Section IIIB2b. The particle size increased significantly as the intensity was increased, as shown graphically in Figure 24. This behavior is directly opposite to the results of the Si_3N_4 powders synthesized from NH_3-SiH_4 gas mixtures where the particle size decreased with increasing laser intensity.

TABLE 4

The Influence of Laser Intensity on the Reaction Temperature and Si Particle Characteristics

Run	Laser Intensity	Temperature $\varepsilon=RT,Si$	Pyrom	$\varepsilon=1/\lambda$	BET Equivalent Diameter (Å)	Crystallite Size (Å) Gaussian	Cauchy	$\dfrac{d_{BET}}{d_{X-ray}}$ Gaussian	Cauchy
643S	5411	960	1230	1490	1106	353	789	3.1	1.4
622S	601	970	1130	1380	1027	348	781	3.0	1.3
635S	531	870	1120	1310	932	338	741	2.8	1.3
646S	424	850	1090	1260	755	254	468	3.0	1.6
648S	407	870	1100	1290	689	217	368	3.2	1.9
638S	265	770	950	1120	380	71	86	5.4	4.4
640S	177	700	890	990	352	62	72	5.7	4.9
658S	134	670	870	940	321	Amorphous		Amorphous	

TABLE 5

The Influence of Reactant Gas Dilution on the Reaction Temperature and Si Particle Characteristics

Run	SiH_4/Ar Ratio	Temperature $\varepsilon=RT,Si$	Pyrom	$\varepsilon=1/\lambda$	BET Equivalent Diameter (Å)	Crystallite Size (Å) Gaussian	Cauchy	$\dfrac{d_{BET}}{d_{X-ray}}$ Gaussian	Cauchy
631S	1/0	960	1055	1490	599	200	334	3.0	1.9
632S	1/0	960	1045	1490	628	191	305	3.3	2.1
653S	100	–	–	–	612	191	305	3.2	2.0
662S	5/1	940	1030	1470	625	204	330	3.1	1.9
661S	3/1	970	1030	1490	609	222	372	2.7	1.6
639S	2/1	940	1030	1440	709	224	397	3.2	1.8
642S	1/1	910	960	1380	586	188	297	3.1	2.0
637S	1/2	890	860	1350	349	83	102	4.2	3.4
634S	1/5	860	770	1280	294	68	82	4.4	3.6
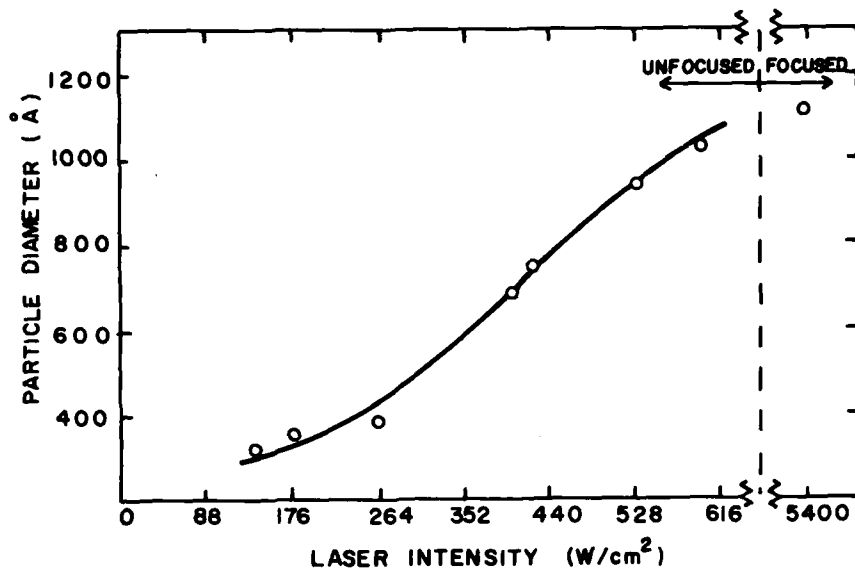
Figure 24. The effect of laser intensity on the resulting Si powder particle
         size.
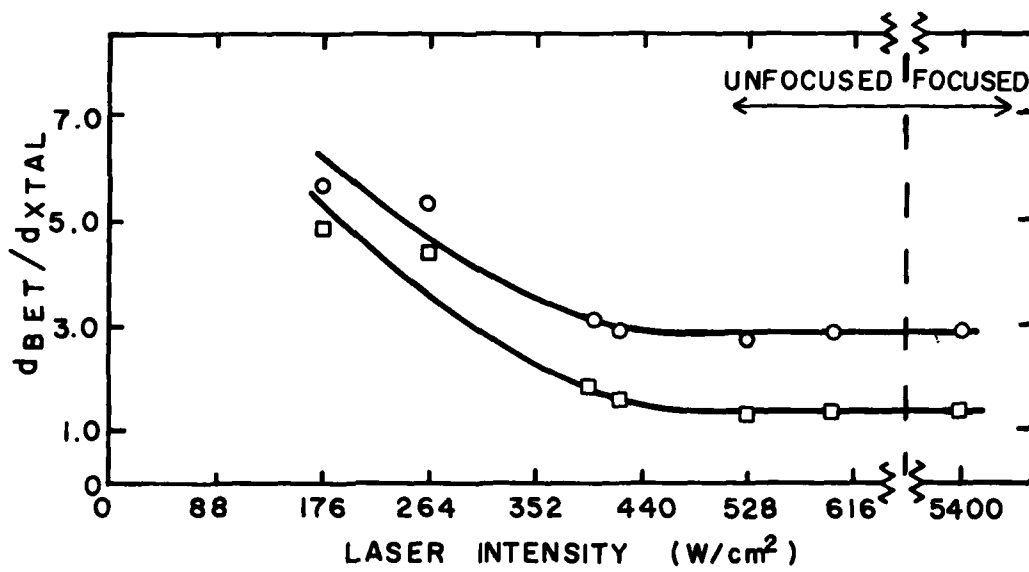
Figure 25. The effect of laser intensity on the ratio of Si particle size to
         crystallite size. O assumes Gaussian shaped X-ray diffraction
         peaks. □ assumes Cauchy shaped X-ray diffraction peaks.

The results of X-ray diffraction line broadening are shown in Figure 25. The $\frac{d\ BET}{d\ X\text{-ray}}$ ratio was approximately constant and equal to 3.0 for powders produced with intensities greater than 400 W/cm^2. The powder produced with the focused laser beam (run 645S) had a similar crystal structure. As the laser intensity was decreased, the $\frac{d\ BET}{d\ X\text{-ray}}$ ratio increased suggesting the dependence on temperature was similar to that observed for powders synthesized at 0.2 atm and a 150 W unfocused beam (see previous section). The X-ray diffraction pattern of the powder produced at 38 W (658S) showed a very broad peak with too much scatter to extract a crystallite size. This pattern suggested an amorphous Si powder which is consistent with our earlier work where lower intensities produced amorphous powders.

iii. Ar Dilution

A series of runs were made to examine the effect of diluting the reactant gas stream with argon. Runs 631S, 632S, and 653S were made under identical conditions with the reactant gas stream comprised of pure SiH_4 to serve as a benchmark from which the effect of dilution could be compared. In the other runs, the argon dilution ranged from a 1/5 Ar/SiH_4 mixture (run 662S) to a 5/1 mixture (634S). The process conditions for these runs as well as the resulting reaction zone and powder characteristics are summarized in Table 5.

The effect of dilution on the reaction zone temperature was discussed in Section IIIB2b. Figure 26 shows the equivalent spherical diameter determined from the BET surface area measurements as a function of the Ar dilution. The particle size appeared to be fairly constant below 50 mole % Ar dilution. Further dilution of the reactant gas stream resulted in a decrease in the BET equivalent particle size.

All these powders were crystalline to X-ray diffraction. The ratio of $\frac{d\ BET}{d\ X\text{-ray}}$ versus the mole fraction Ar is plotted in Figure 27. This ratio is constant up to 50 mole % dilution and then increases as the reactant gas
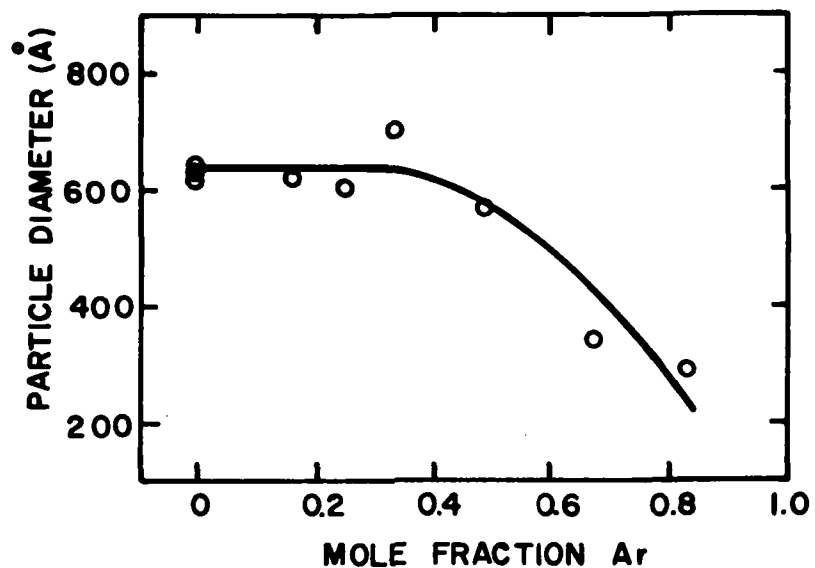
Figure 26. The effect of reactant gas dilution on the resulting Si powder particle size.
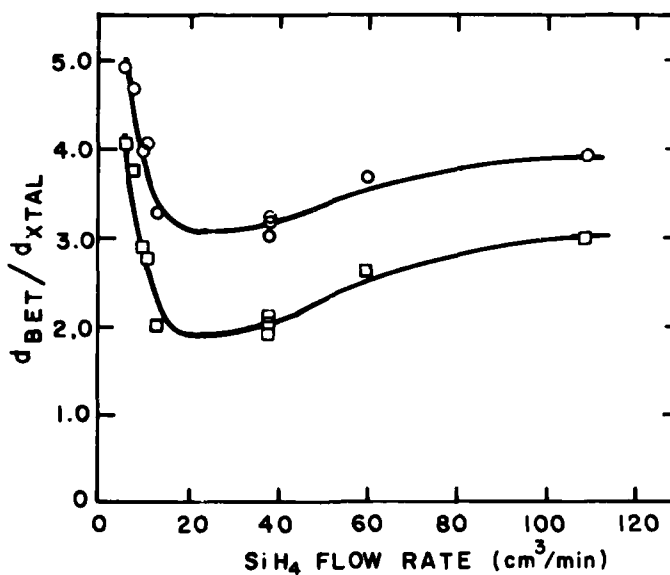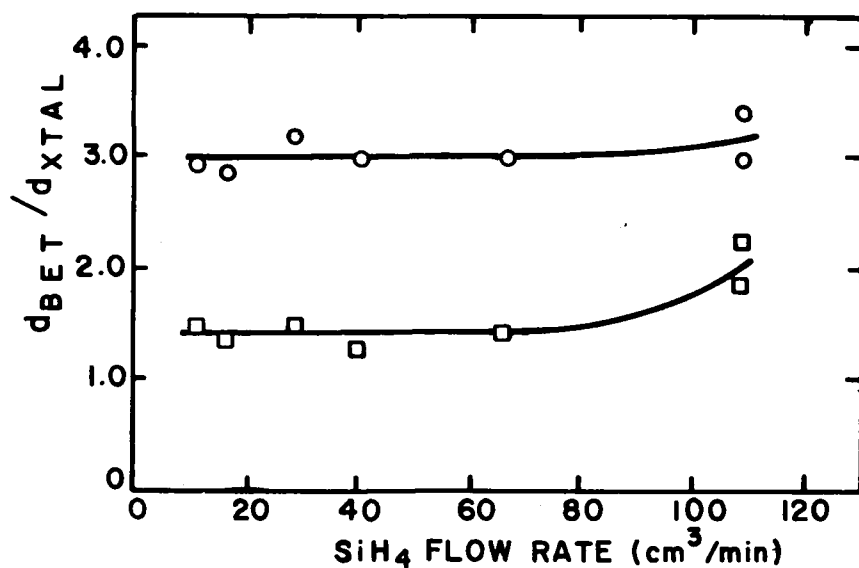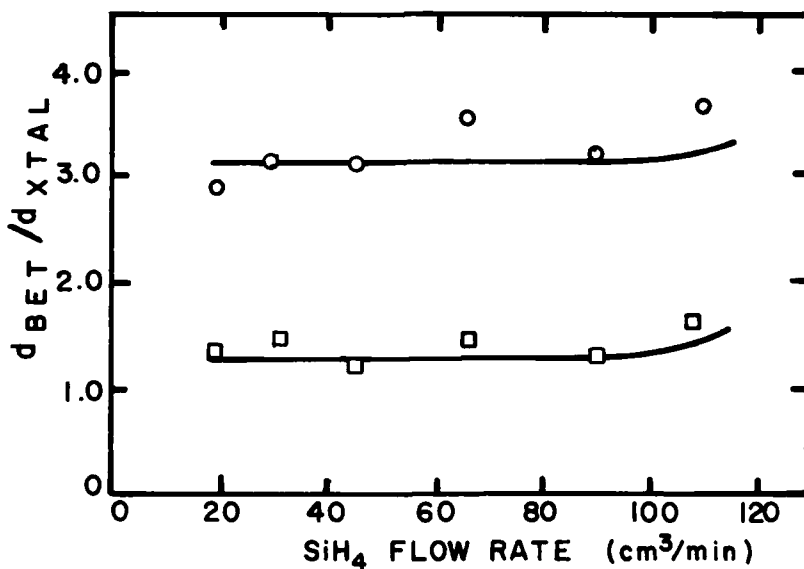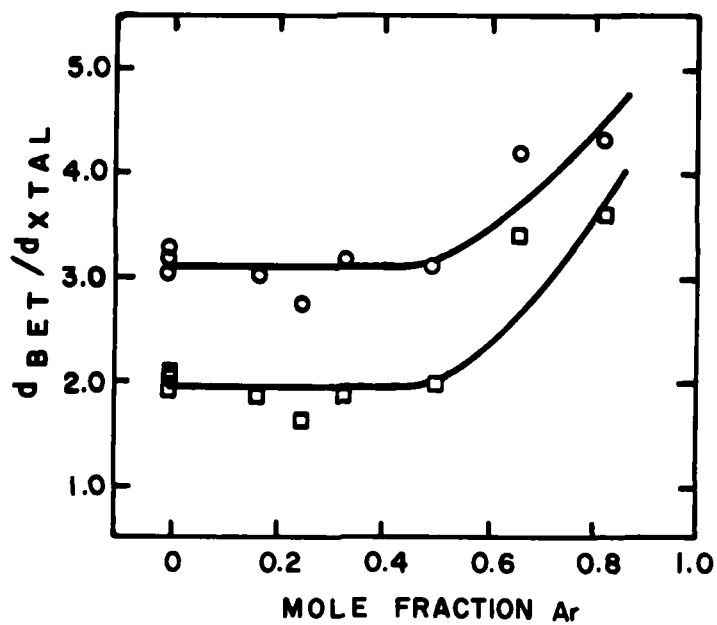

Figure 27. The effect of reactant gas dilution on the ratio of Si particle size to crystallite size. O assumes Gaussian shaped X-ray diffraction peaks. □ assumes Cauchy shaped X-ray diffraction peaks.

stream is further diluted. Once again the larger ratio of $\frac{d \ BET}{d \ X\text{-}ray}$ appears to be related to a decrease in the reaction zone temperature (see Figure 15).

Figure 16 shows a TEM micrograph of powder 634S (5/1 Ar/SiH$_4$ ratio). The average particle size measured from this micrograph is 275 Å, which is in close agreement with the BET equivalent diameter of 294 Å. The particle size appears to be quite uniform, ranging from 189 Å to 355 Å. It was anticipated that diluting the gas stream with Ar would decrease the probability of collision between particles and thus reduce the particle agglomeration. Figure 16 shows that the powder produced with this dilution still exhibits the typical two-dimensional chain-like agglomerates, with significant necking between particles. Agglomerates are discussed more fully in Section IIIC4.

Two additional runs (655S and 660S) were made in which the reaction zone was diluted with Ar. In addition these runs were produced at lower laser intensities than the runs described above. It was anticipated that the combined effects of lowering the laser intensity and diluting the reactant gas with Ar would result in a low reaction zone temperature thereby producing an amorphous Si powder. These runs are also summarized in Table 5. The powder produced with a 75 W unfocused beam and a 1/1 Ar/SiH$_4$ gas mixture did not appear totally amorphous but had a particle diameter of 289 Å (from BET surface area measurements) with small crystallites (58 Å). Run 660S, with a 50 W unfocused beam and a 2/1 Ar/SiH$_4$ gas mixture, produced powder with a very large BET surface area, 136 m^2/g (equivalent spherical diameter of 190 Å). X-ray diffraction revealed only very broad peaks corresponding to Si(111) and Si(220) suggesting an amorphous structure. The reaction flame was too dim for a temperature to be measured. Bright field – dark field transmission electron microscopy will have to be done to determine conclusively whether the structure is truly amorphous or comprised of very fine crystallites.

iv. Pressure

The effect of pressure on the reaction zone and powder characteristics was examined by comparing the two series of runs produced at 0.2 atm and 0.6 atm. It is difficult to make a run to run comparison because of the difficulty of maintaining constant flow conditions while changing the total cell pressure. An increase in cell pressure resulted in a decrease in the reaction zone temperature as was described in Section IIIB2b. Comparison of Figures 18 and 20 shows that increased pressure leads to a larger particle diameter. The same trend was observed for the powders produced at 0.35 atm, although since these powders were synthesized with 170 W power instead of 150 W, a direct comparison with the runs synthesized at 0.2 atm and 0.6 atm is not valid.

Examination of Figures 21, 22 and 23 suggests that changes in total reaction cell pressure effects the crystallinity of the powders. For powders produced at 0.6 atm, the ratio of the BET equivalent diameter to the crystallite size measured by X-ray line broadening is constant, while this ratio is dependent on reaction temperature for powders produced at 0.2 atm. The ratio of the BET diameter to the crystallite diameter as related to the crystal structure of the individual particles is discussed more fully in Section IIIC1ciii.

v. Boron Doping

It has been reported[24] that the addition of small amounts of boron increases the sinterability of silicon. It is difficult to add amounts typically less than 0.5 wt. % in the solid state and achieve a uniform dopant distribution. The laser synthesized process offers a unique method to add the dopant. A gas species containing the wanted dopant is added directly to the reactant gas stream. Since it appears this process is in the thermal domain, it is not necessary for the dopant gas to absorb the laser energy. By this method the dopant can be uniformly distributed throughout the powder and can be actually incorporated into the silicon particles.

48

Diborane, B_2H_6, was used as the boron source. Because of the toxicity of this gas, we used the B_2H_6 in mixture with Ar. For most of these runs, a 1.0% B_2H_6 + Ar mixture was used. The run conditions and resulting powder characteristics are shown in Table 6. Also shown in this table are runs made under identical conditions except pure Ar was used instead of the 1 % B_2H_6 + Ar mixture. If the dopant is fully incorporated, a 2/1 SiH_4/B_2H_6 + Ar+ 1.0% mixture will result in a Si powder containing 0.328 wt. % boron. The particle size and reaction temperature shown are the average of 10 undoped runs and 9 doped runs. The particle size remained essentially unchanged. It appears the reaction temperature, measured by both the pyrometer and PMT-interference filter technique, increased slightly for the B-doped runs. Chemical analyses indicated that 0.47 wt. % boron was incorporated into the powders, showing 100% reaction of the dopant gas. TEM revealed the doped powders were badly necked probably as a result of increased reactivity.

c. Analysis and Discussion

i. Heating Rates

The time-temperature history of the reactant gases as they travel through the laser beam have been calculated.[3] For this calculation, the path of a gas element which passes through the laser beam is divided into a

TABLE 6

Comparison of B_2H_6/SiH_4 and Undoped SiH_4 Runs*

Run Type	BET Equivalent Size (Å)	Temperature (°C)		
		$\epsilon = _{RT,Si}$	Pyrom	$\epsilon = 1/\lambda$
SiH_4/Ar	551±45	980±6	1433±39	935±14
SiH_4/Ar + 1%B_2H_6	549±23	1012±10	1494±21	966±10

* For all runs: Pressure = 0.2 atm, Laser Intensity = 531 W/cm^2, SiH_4 Flow Rate = 50 cm^3/min, Ar or Ar 1%B_2H_6 = 25 cm^3/min

number of intervals. In each interval, the gas element is assumed to have a constant velocity and is subjected to a constant laser beam intensity. The laser beam intensity in each interval is calculated from a Gaussian-shaped distribution and the gas velocity at any point is determined by a gas flow model. The volume element absorbs power proportional to the local intensity and optical absorption. The temperature rise is calculated from the residence time which is inversly proportional to the local velocity of the volume element. It is assumed that there is no dilution of the gas stream by the annular Ar stream. Thus, the gas volume consists of only the reactant in porportions defined by the volumetric flow rates. In this manner, the heating rate within the interval as well as a temperature-time history for the entire path of this volume element through the laser beam can also be calculated. After reaction occurs, it is assumed that the residual gas stream and particles produced by the reaction are transparent to the laser beam.

Figure 28 shows the calculated effect of velocity on heating rates for gas volume elements traveling along the central axis of the gas stream through the maximum laser intensity. The four curves correspond to run 629S (silane flow rate = 5.5 cm^3/min), 625S (11 cm^3/min), 631S (38 cm^3/min) and 630S (104 cm^3/min) at a cell pressure at 0.2 atm. An average value was used for the SiH_4 absorption coefficient (7.5 $(atm-cm)^{-1}$) and it was assumed to be independent of temperature. We have evidence that this may not be an entirely accurate assumption (see Section IIIA), but at present there is insufficient data to determine the actual dependence of the absorptivity on temperature.

For all of these velocities, the heating rate analysis predicts that the gases should reach temperatures in excess of 1000°C before reaching the maximum laser intensity at the center of the laser beam. For run 629S (having a SiH_4 flow rate of 5.5 cm^2/min), the reactant gas is heated to 1200°C after it has traveled only 0.025 cm into the 0.5 cm diameter laser beam. For run 630S (104 cm^3/min SiH_4), the reactant gas is heated to 1200°C after traveling 0.20 cm into the 0.5 cm diameter beam. For this run, the reaction flame had a shape similar to that shown in Figures 3 and 4 with the
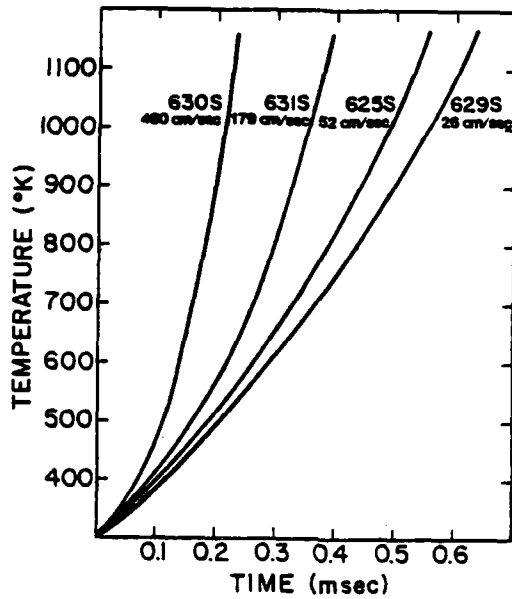
Figure 28. The effect of velocity on the calculated temperature of the reactant gases during synthesis.
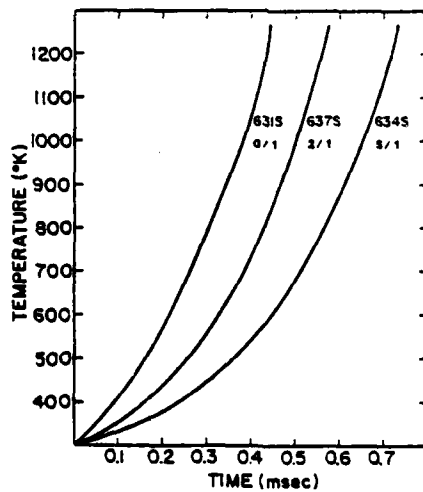
Figure 29. The effect of Ar/SiH_4 ratio on the calculated temperature of the reactant gases during Si synthesis.

51

upper cusp of the flame located at approximately 0.2 cm into the laser beam. For the lower flow rates, the flame did not exhibit the characteristic cusp. It appeared that the lower flame boundary was coincident with the beginning of the laser beam. In all cases, the reaction was initiated before the reactant gases penetrated to the centerline of the laser beam where the intensity reaches its maximum.

Figure 28 shows that both average heating rates and instantaneous heating rates at the temperature level where silane pyrolyzes rapidly, approximately 1000K, increase with increasing reactant gas flow rate. It would be anticipated that higher instantaneous heating rates will force the reaction temperature to higher levels, so the faster SiH_4 flow rates should produce a higher reaction temperature. This is not in agreement with the ascending-descending temperature dependence on reactant gas flow shown in Figure 12.

Figure 29 shows the calculated heating rates for gas elements traveling along the gas stream axis for run conditions corresponding to runs 631S, 634S and 637S. These illustrate that diluting the reactant gas stream with Ar affects two critical parameters which determine the gas heating rate. First, it decreases the absorption coefficient of the gas stream since Ar is essentially nonabsorbing at a wavelength of approximately 10.6 μm. Second, the heat capacity is changed significantly since the heat capacity of SiH_4 is 3 to 4 times greater than that of Ar. These two effects act in opposite directions. Combined, they produce a less pronounced effect than if the reactant gas stream was diluted with a non-absorbing species having a heat capacity similar to that of SiH_4. Figure 29 shows that both the average heating rate and the instantaneous heating rate decrease as the reactant gas stream is diluted with argon. The instantaneous heating rates do not change as much because the diluted reactants penetrate to a point closer to the centerline of the laser beam when they reach the reaction temperature, therefore, the local laser intensity is higher.

The analysis showed the gas heating rate will be independent of pressure[3] for gas streams that are optically thin. In a highly absorbing gas stream, the laser beam will be progressively absorbed as it passes

52

through the gas stream, causing differences in thermal histories between gas elements on the entering and exiting sides of the gas stream. This heating rate analysis also assumed that the optical absorptivities are independent of pressure. This is not precisely valid as shown in Section IIIA. The data required to provide a more accurate model is not yet available, so it is not possible to predict pressure effects on heating rates with any more accuracy.

These heating rate analyses do not include the effect of latent heat associated with the pyrolysis of SiH_4 to form Si powder. In fact, they are thermal analyses of the process up to the point that the reaction just begins. The following simple calculations permit conclusions to be made regarding both the possibility of a self-sustaining reaction without continued input of energy from the laser as well as the anticipated maximum temperature rise in the reaction products.

To a first approximation, a reaction can be self-sustaining only if the latent heat released during the reaction exceeds the sensible heat required to raise the reactants to a temperature level where the reaction proceeds rapidly. For the silane pyrolysis reaction

$$SiH_4(g) \rightarrow Si(s) + 2H_2(g) \tag{9}$$
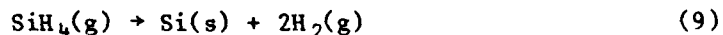
at 1100K, the latent heat is $\Delta H = 2.14 \times 10^4$ J/mole[25] and the sensible heat required to raise the gas to this temperature is 5.76×10^4 J/mole. With 90% conversion efficiency, the effective latent heat (1.93×10^4 J/mole) is less than the sensible heat. This reaction cannot be self sustaining unless the reaction is induced at a much lower temperature. With the same conversion efficiency, we estimate that the adiabatic temperature rise in the excess reactants and reaction products would be approximately 180°C.[3]

ii Nucleation and Growth for Si Powder Synthesis

● Theoretical

The formation of silicon particles via vapor phase reactions occurs by homogeneous nucleation and growth processes. The four stages of a phase

transformation are development of a supersaturated state, generation of
nuclei of the new phase, growth of the nuclei to form larger particles and
relaxation processes, such as coarsening and agglomeration.

Unimolecular[26,27] and chain[28,29] mechanisms have been reported for
monosilane decomposition. The unimolecular decomposition leads mainly to
the formation of silicon and hydrogen while chain decomposition occurs with
the participation of radicals (SiH_4, SiH_3, Si_2H_5) and can result in the
formation of higher silanes (Si_2H_6, Si_3H_8, etc.).

An early study of the laser induced decomposition by Oraevskii et al.[30]
showed the only gaseous product was hydrogen suggesting that the
decomposition occured by a unimolecular mechanism. In a detailed study of
the infrared laser photochemistry of silane, Deutsch[31] defected SiH_2 and a
number of unidentified peaks with masses between 32 and 44, however there
was no evidence of the higher silanes. These results are not sufficient to
determine the mechanism for decomposition, although the absence of the
higher silanes suggests that the laser induced pyrolysis may occur by a
simple decomposition reaction.

If we assume that the decomposition occurs by a unimolecular mechanism,
then the supersaturation within the reactant gas stream can be calculated as
a function of temperature and the gas concentration from classical
thermodynamics. The formation for a silicon cluster occurs via the
following reactions:

$$SiH_4(g) \xrightarrow{h\nu} Si(g) + 2H_2(g) \qquad (10)$$

$$n\ Si(g) \rightarrow Si_n(s) \qquad (11)$$
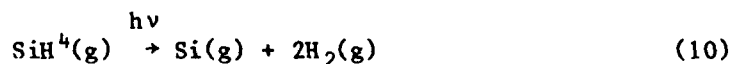
A cluster Si_n is stable if it reaches a critical size of radius r^*. The
supersaturation ratio, SS, is determined by the quotient of the partial
pressure of Si(g) in the reactant gas stream P_{Si}, divided by the equilibrium
vapor pressure of Si, P_{Si}°.

$$SS = \frac{P_{Si} \text{ (reacting)}}{P_{Si}^{\circ} \text{ (equilibrium)}} \qquad (12)$$

The overall driving force for nucleation is the reduction in free energy accompanying the formation of solid silicon:

$$SiH_4(g) \rightarrow Si(s) + 2H_2(g) \qquad k_1 \qquad (13)$$
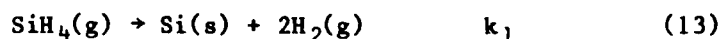
which is the sum of the following reactions:

$$SiH_4(g) \rightarrow Si(g) + 2H_2(g) \qquad k_2 \qquad (14)$$

and

$$Si(g) \rightarrow Si(s) \qquad k_3. \qquad (15)$$
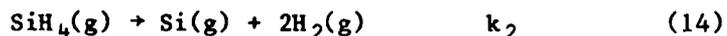
Under equilibrium conditions:

$$P_{Si}^{\circ} = 1/k_3 \qquad (16)$$

and

$$k_2 = \frac{P_{Si} \text{ (react)} P_{H_2}^{2}}{P_{SiH_4}} . \qquad (17)$$

Therefore:

$$SS = \frac{k_2 P_{SiH_4}}{P_{H_2}^{2}} \cdot k_3 = k_1 \frac{P_{SiH_4}}{P_{H_2}^{2}} . \qquad (18)$$

Thus, the supersaturation ratio at a given temperature can be calculated from the amount of SiH_4.

Figure 30 shows the effect of temperature and percent reaction on the supersaturation ratio assuming P_{SiH_4}(initial) = 0.2 atm, corresponding to a total reaction pressure of 0.2 atm and assuming no dilution of the reactant gas stream with argon prior to reaction. Figure 30 shows that the supersaturation ratio decreases with increasing temperature. The overall driving force for nucleation increases with temperature since the free

55
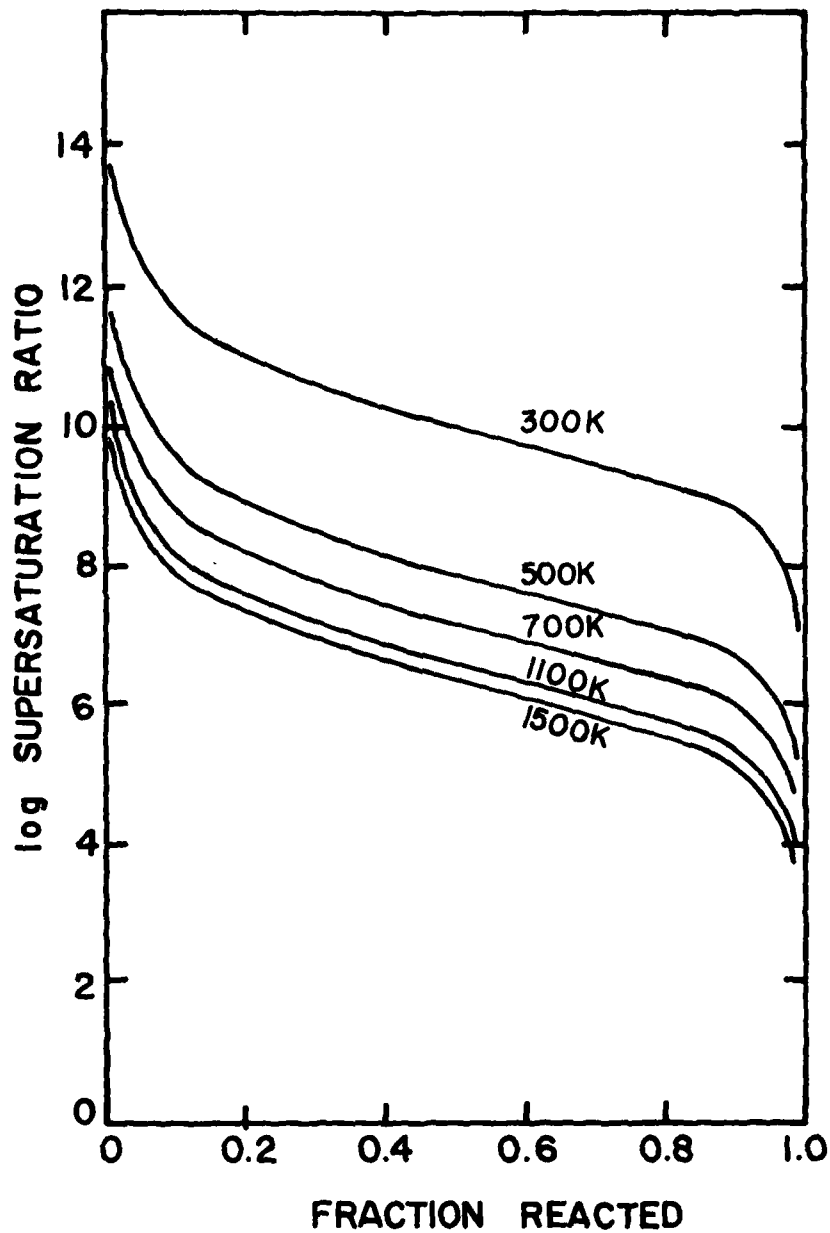
Figure 30. The effect of temperature and percent reaction on the supersaturation ratio for SiH_4 pyrolysis.

energy change increases with increasing temperature.[25] Since $\Delta G_v = \frac{-RT}{V_{Si}} \ln(SS)$, where ΔG_v is the change in free energy per unit volume of Si(s) formed and V_{Si} is the molecular volume of Si(s), the increase in ΔG_v with temperature indicates that $\ln SS$ decreases at less than a linear rate with increasing temperature.

A critical radius size, r^*, can be approximated by the application of homogeneous nucleation theory to a supersaturated vapor:[32]

$$r^* = \frac{-2\sigma}{\Delta G_v} \qquad (19)$$

where σ is the surface free energy of Si(s) and ΔG_v is the volume free energy change in forming Si(s). There is some question as to what value of σ should be used when referring to nuclei with size on the order of 10's of Angstroms. Calculations from SS data in Figure 30 indicate that the volume free energy changes, ΔG_v, are large even at low temperatures. Using these values and a value of 900 erg/cm^2 for σ, it was found that r^* was very small, for example on the order of 1.2 Å at 1100K and assuming 10% conversion of SiH_4. With the atomic volume of Si equal to 20.1 Å^3, a cluster of diameter 2.4 Å would have a volume less than the atomic volume of solid silicon indicating that there is essentially no barrier toward nucleation. These calculations show that the nucleation process is kinetically limited, that is nucleation will not proceed at a significant rate at low temperatures because the extent of reaction is small until a critical temperature is reached.

There are various possible mechanisms by which a nucleus having reached critical size can grow. If growth is limited by transport of vapor to the particle surface, the rate can be determined from diffusion theory. For the continuum range, that is if the particle size is much larger than the mean free path in the gas, the growth rate is given by:[33]

$$\frac{dv}{dt} = \frac{2\pi\, D d_p V_{Si}}{kT} (P_{Si} - P_{Si}^\circ) \qquad (20)$$

57

where v is the particle volume, t is time, D is the gaseous diffusion coefficient, d_p is the particle diameter, V_{Si} is the molecular volume of Si, k is Boltzmann's constant, T is temperature, and the presures have the same meaning as Equation 12. For particles much smaller than the mean free path of the gas, the growth law is derived from the kinetic theory:[33]

$$\frac{dv}{dt} = \frac{\pi d_p^2 V_{Si} (P_{Si} - P_{Si}^{\circ})}{(2\pi mkT)^{1/2}} \tag{21}$$

where m is the mass of a Si atom.

The particle may grow by a chemical reaction at the surface. If the reaction rates are slow compared to vapor transport, the concentration of reactant species near the particle surface is essentially the same as in the bulk of the gas, and the particle growth rate is then given by:[33]

$$\frac{dv}{dt} = \frac{\alpha P_{Si} \pi d_p^2 V_{Si}}{(2\pi mkT)^{1/2}} \tag{22}$$

where α, the general condensation coefficient is the probability that such an impinging molecule will be adsorbed, thermally equilibrated and incorporated into the surface. α is usually much less than 1 and may be a function of both temperature and pressure.

● Experimental

Once the reactant gases reach the reaction temperature, particles begin to nucleate and grow within the gas stream. Mass balance measurements have shown that the silane is almost completely depleted from the reactant gases. Thus, the particle growth is not limited by the elapsed growth time, but by the impingement of the depletion volumes of the growing particles. The depletion volume, V_{DEP}, is calculated by comparing the mass of silicon in

58

the particles with the mass density of silicon atoms in the reactant gas stream and the measured conversion efficiencies.

The calculated depletion volumes for silicon synthesis runs are summarized in Figures 31, 32, 33, and 34. In general, the depletion volumes range from about 1.4×10^{-11} cm^3 to 6.84×10^{-13} cm^3, corresponding to entrained particle densities in the gas stream of 7.14×10^{10} to 1.46×10^{12} particles/cm^3 depending upon the specific run conditions. The particle density is a direct measure of the number of nucleation events which occur before impingement of depleted gas volumes.

Figures 31 and 32 show the effect of flow velocity on the depletion volume for the runs corresponding to pressures of 0.20 and 0.60 atm, respectively. The similarity of these curves with those in Figures 12 and 13 suggests that lower temperatures produce smaller depletion volumes and thus a smaller particle size.

Figure 33 shows the effect of argon dilution on the depletion volume. Once again lower reaction temperatures produced smaller depletion volumes. As the Ar/SiH$_4$ ratio increases the depletion volume decreases. Also, the density of silane molecules in the gas stream decreases by a factor of 3 for run 637S (2/1 AR/SiH$_4$) and by a factor of 6 for run 634S (5/1 Ar/SiH$_4$). The combination of these effects indicates why the particle size decreased with argon dilution as shown in Figure 26.

Figure 34 shows the effect of laser intensity on the depletion volume. Laser intensity produced the greatest effect on this characteristic of the process. Powder made with an intensity of 265 W/cm^2 (638S) had a depletion volume of 6.84×10^{-13} cm^3 while that produced with 601 W/cm^2 (622S) had a volume of 1.73×10^{-11} cm^3.

The effect that pressure has on the depletion volume is indicated by comparing Figures 31 and 32. The depletion volume increased by approximately a factor of 5 as the reaction cell pressure was increased from 0.20 atm to 0.60 atm. If the depletion volume was not significantly changed by small variations in pressure with all other process parameters held constant, we would expect the particle volume to be directly proportional to
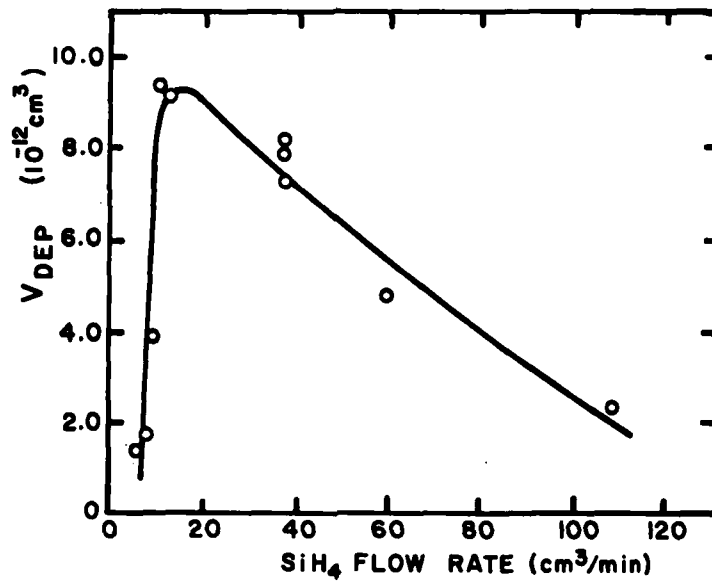
Figure 31. The effect of SiH₄ flow rate on the calculated gas depletion
volume for Si synthesis (reaction cell pressure of 0.2 atm).
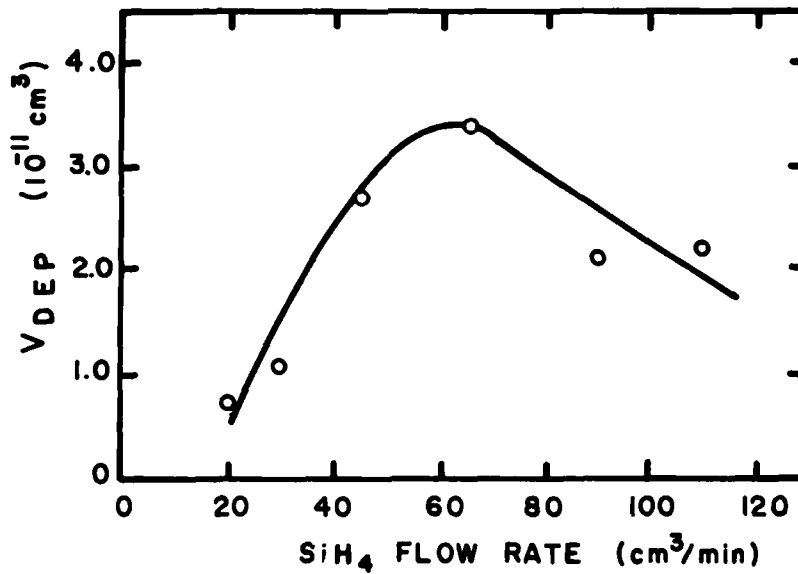
Figure 32. The effect of SiH₄ flow rate on the calculated gas depletion
volume for Si synthesis (reaction cell pressure of 0.6 atm).
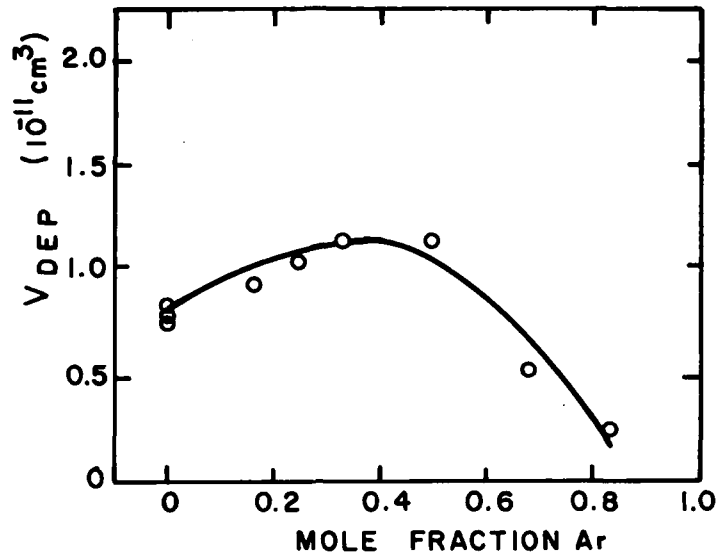
Figure 33. The effect of reactant gas dilution on the calculated gas
depletion volume for Si synthesis (reaction cell pressure of
0.2 atm).
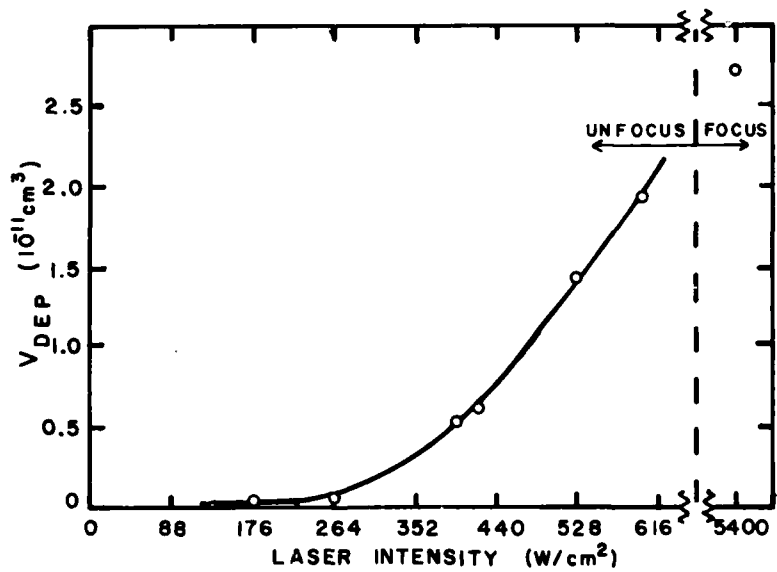
Figure 34. The effect of laser intensity on the calculated gas depletion
volume for Si synthesis.

the pressure, since the density of silane molecules in the reactant gas stream is directly proportional to the pressure.

The depletion volume can be related to the relative nucleation and growth rates within the gas stream by the following expression:

$$V_{DEP} \propto \left(\frac{R_G}{R_N}\right)^{3/4} \qquad (23)$$

where V_{DEP} is the depletion volume, R_G is the radial particle growth rate, and R_N is the nucleation rate. Both the nucleation and growth rates are expected to be dependent on reactant gas pressure and temperature. For silane pyrolysis, this dependence can be represented[34] empirically by:

$$R_G = k_G \, P_{SiH_4}^x \, \exp\left(-E_G/kT\right) \qquad (24)$$

and

$$R_N = k_N P_{SiH_4}^y \, \exp\left(-E_N/kT\right) \qquad (25)$$

where k_G and k_N are constants, P_{SiH_4} is the SiH_4 partial pressure in the gas stream, x and y are empirical constants describing the dependence of the growth and nucleation on reactant gas pressure, and E_G and E_N are the activation energies for particle growth and nucleation. Therefore, the dependence of the depletion volume on the reactant gas pressure and temperature can be emipirically represented by:

$$V_{DEP} \propto \left(\frac{k_G}{k_N}\right)^{3/4} \cdot P_{SiH_4}^{\frac{3(x-y)}{4}} \cdot \exp\frac{-3(E_G - E_N)}{4kT} \, . \qquad (26)$$

By comparing the calculated depletion volumes for the various silicon

synthesis runs, the relative dependencies of the nucleation and growth rates on the reactant partial pressure and temperature were investigated.

Figure 35 shows a plot of log V_{DEP} versus 1/T for synthesis runs in which only the laser power was varied. The temperature used was calculated from the PMT-interference filter results assuming an emissivity dependence of $1/\lambda$ (see Section IIIB2b. The data exhibits a linear dependence with some scatter especially for the results of run 638S. The slope of this line should equal $\frac{-3(E_G - E_N)}{4kT}$. The negative slope indicates that $(E_G - E_N)$ isgreater than zero, that is the growth rate exhibits a stronger temperature dependence than the nucleation rate.

Figure 36 shows the effect of temperature on the depletion volume for runs performed at pressures of 0.2 atm and 0.6 atm. The reactant gas velocity was the only parameter varied for each series of runs. Again the slope of the lines is negative indicating that $(E_G - E_N)$ is greater than zero. The difference in the slopes of 0.2 atm and 0.6 atm may or may not be significant. Two least squares lines were drawn through the experimental points for runs performed at 0.2 atm. Line A corresponds to runs with SiH_4 flow rate less than 13 cc/min while line B is from runs made at higher flow rates. This difference may result from varying dilution of the reactant gas stream by the outer annular flow of argon. All depletion volumes were calculated assuming that the reactant gas stream was comprised of only SiH_4 gas without taking into account any dilution by argon.

At a constant temperature, the difference in the depletion volume is related to the partial pressure of reactant gas and the relative dependence of the nucleation and growth rates on the partial pressure. This assumes that the activation energies for particle nucleation and growth are independent of the partial pressure of the reactant gas. Figure 36 indicates that the depletion volume increased with an increase in reaction pressure. From reference to Equation 26, $(E_G - E_N)$ is positive, suggesting that the nucleation rate is less dependent to changes in the reactant gas concentration than the rate of particle growth.

In this experimental configuration, the inception of the nucleation events and the growth process can be monitored directly with respect to
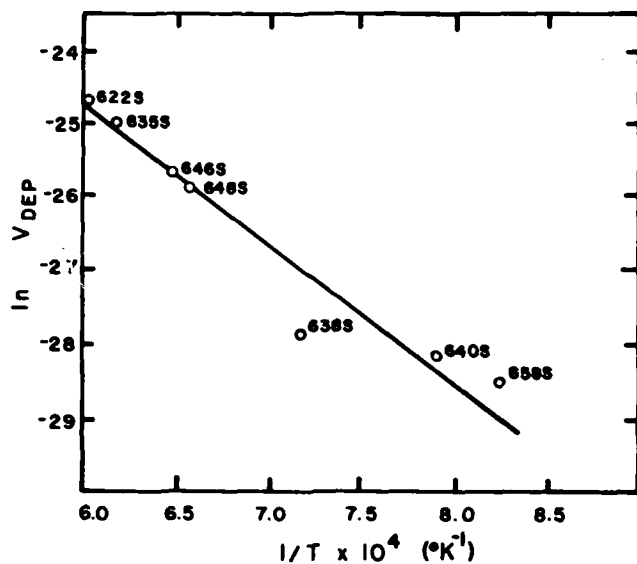
Figure 35. The effect of reaction temperature on the calculated gas depletion volume for Si synthesis at various laser intensities. The temperature was calculated from the PMT-interference filter technique assuming $\epsilon = 1/\lambda$.
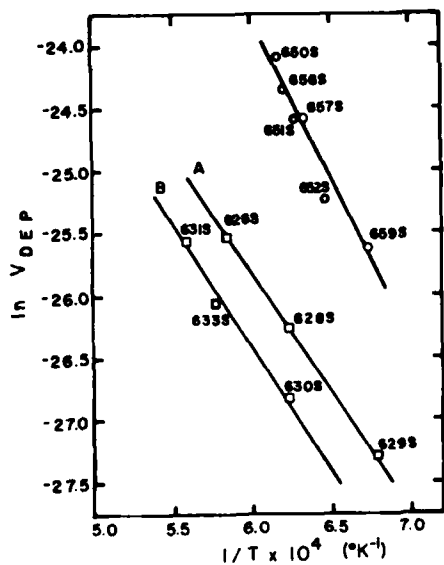
Figure 36. The effect of reaction temperature on the calculated gas depletion volume for Si synthesis at various flow rates. 0 represents runs with a cell pressure of 0.6 atm. □ represents runs with a cell pressure of 0.2 atm. The temperature was calculated from the PMT-interference filter technique assuming $\epsilon = 1/\lambda$.
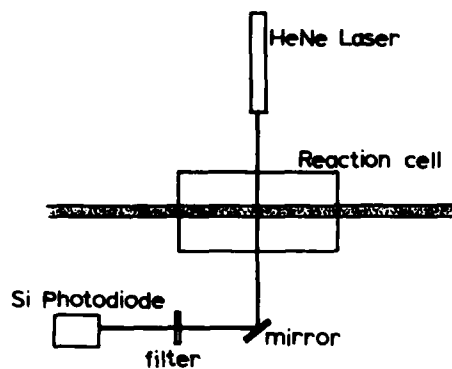
Figure 37. Schematic of equipment used for light extinction experiments.

position in the reaction flame. These observations were made by measuring the extinction of a He-Ne laser beam ($\lambda = 6328$ Å) through the flame. Figure 37 shows the experimental apparatus used. The He-Ne laser beam was transmitted through the reaction zone at various positions above the gas inlet nozzle. The transmitted intensity was measured using a silicon photodiode. Since the He-Ne laser was mounted on an x-y stand, the path length could be measured assuming the flame had a circular cross-section.

The transmitted intensity through the flame, I, was compared to unattenuated transmitted intensity, I_o. The ratio of these intensities can be related to the extinction cross-section of the particles by the following relations:[6]

$$I/I_o = \exp(-\tau \ell) \tag{27}$$

$$\tau = NC_{EXT} \tag{28}$$

where τ is the turbity, ℓ is the path length, N is the number density of particles and C_{EXT} is the particle extinction cross-section. These relations assume that there is no multiple scattering and the scattering is elastic, that is the wavelength of the incident and scattered beam are the same.

The extinction cross-section, C_{EXT}, is equal to the sum of the scattering cross-section, C_{SCA}, and the absorption cross-section, C_{ABS}. The particle volume can be related to the scattering and absorption cross-sections.[6] If we assume that Rayleigh scattering is dominent, that is the particle diameter is small compared to the wavelength of light,

$$C_{SCA} = \frac{24\pi^3}{\lambda^4} V^2 \left| \frac{m^2 - 1}{m^2 + 2} \right|^2 \tag{29}$$

$$C_{ABS} = -4V \frac{2\pi}{\lambda} \, \text{Im} \left\{ \frac{m^2 - 1}{m^2 + 2} \right\} \tag{30}$$

where m is the complex refractive index, $(m = n - in')$, V is the particle volume, λ is the wavelength of incident light and $Im \left\{ \dfrac{m^2 - 1}{m^2 + 2} \right\}$ is the imaginary part of the complex quotient $\dfrac{m^2 - 1}{m^2 + 2}$. To calculate the particle size from the transmission results it is necessary to know N, the density of particles, and both the real and imaginary parts of the refractive index.

Figures 38, 39, and 40 show the particle diameter, calculated from extinction results, as a function of position in the flame for runs 653S, 663S, and 654S. These runs were made under the same conditions as run 631S, 642S and 637S in which the reactant gas stream was diluted with Ar. The run conditions were summarized in Appendix I. The two most important results revealed by the transmission experiments are:

1. No scattering was detected below the visible region of the flame.
2. Most of the particle growth occurs in the hot region of the flame.
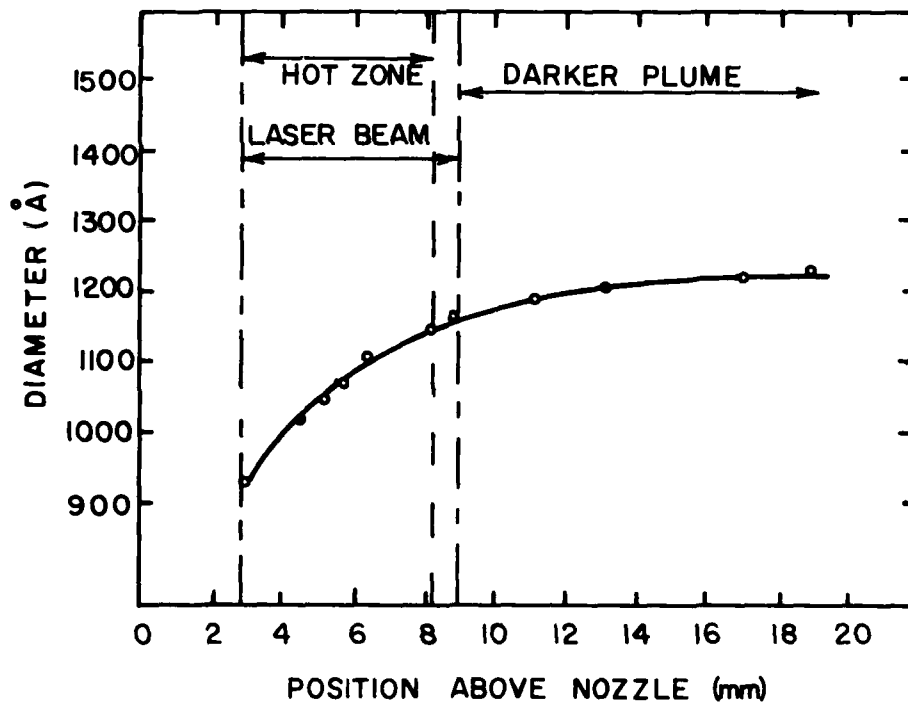
Figure 38. Particle diameter as a function of position in reaction zone for Si synthesis as measured by light extinction (Ar/SiH$_4$ ratio of 0/1).

66
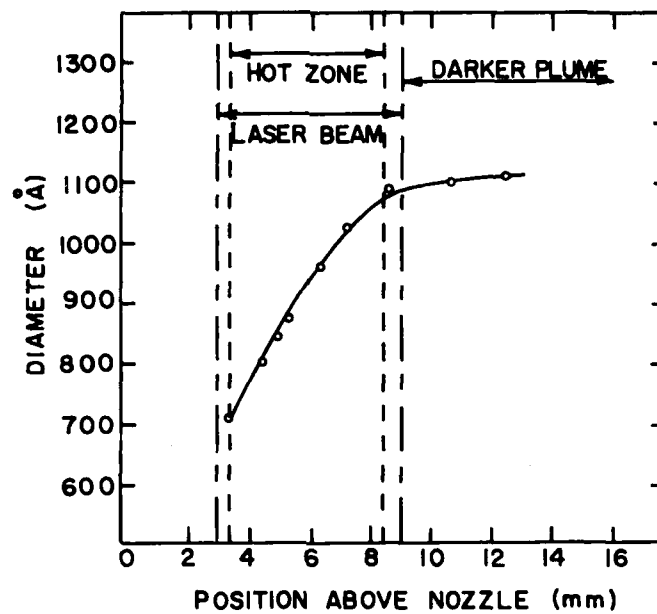
Figure 39. Particle diameter as a function of position in reaction zone for Si synthesis as measured by light extinction (Ar/SiH$_4$ ratio of 1/1).
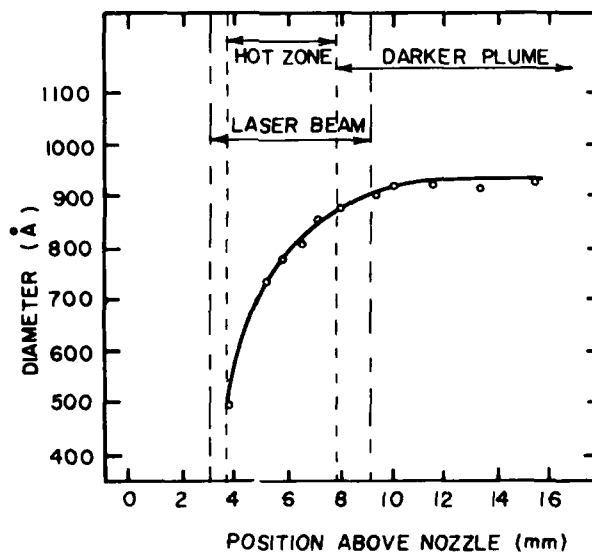
Figure 40. Particle diameter as a function of position in reaction zone for Si synthesis as measured by light extinction (Ar/SiH$_4$ ratio of 2/1).

67

Comparison of Figures 38, 39, and 40 show that the final diameter
calculated from the scattering results decreases as the reactant gas stream
was diluted with Ar, as was confirmed from BET surface area measurements
(see Section IIIClb). The average radial growth rate ranged from
approximately 1300 $\mathring{A}$/sec for run 653S (no Ar dilution) to 2300 $\mathring{A}$/sec for run
654S (2/1 Ar/SiH$_4$ ratio). The beginning of the reaction zone, as evidenced
by the visible emission from the particles and the onset of the He-Ne
scattering, occurred further into the CO_2 laser beam as the gas stream was
increasingly diluted. In all cases, the final diameter predicted from the
scattering results is about a factor of two larger than the particle
diameter measured from BET surface area for powders synthesized under these
run conditions. The causes of this descrepency may be that incorrect values
were used for the real and imaginary indices of refraction, the particles
may be agglomerated and the agglomerate size is being measured, or there may
be deviation from ideal Rayleigh scattering behavior. It should also be
noted that in order to actually separate the particle diameter and number
density from the scattering results, it is necessary to measure the
scattered intensity. These experiments are underway.[35]

iii. Crystal Structure of the Silicon Particles

Almost all of the Si powders have been polycrystalline, that is the
crystallite size is smaller than the particle size. This has been confirmed
by BET surface area measurements, X-ray line broadening and both bright and
dark field TEM. The surface area and line broadening results were presented
in Section IIIClb. The following discussion describes briefly the possible
silicon formation processes that could lead to polycrystalline particles.

Individual crystals may be formed from the vapor phase, and these
crystals may coalesce and sinter to form the final particles. The close
agreement of the particle diameter measured by the BET surface area
technique and electron microscopy indicates that there is no void space
between the crystallites in the particles that is accessible to the N_2
absorbate gas. He gas pycnometry has revealed the density of the powder to

be near the density of crystalline silicon indicating that there is no internal porosity in the individual particles. These observations make it unlikely that the polycrystalline particles formed from individual crystallites.

The nucleation and growth process may involve the formation of liquid silicon droplets which then solidify upon cooling. It is possible that if the cooling rate is very rapid, the liquid would solidify as an amorphous material. It is more likely that the silicon will crystallize upon cooling. Depending upon the kinetics of the transformation process, the droplets might crystallize as single or polycrystalline particles. The temperature results discussed in Section IIIB2, showed that under certain conditions the reaction temperature was above the melting point of silicon. It is anticipated that powder synthesized under conditions where the temperature was higher than the Si melting point would have a different microstructure than powder synthesized at temperatures below the melting point. TEM analysis did not indicate any noticeable microstructural differences, suggesting the powders did not form from liquid droplets.

The particles may have formed as an amorphous solid and crystallized while they were still in the hot zone of the flame. If the reaction temperature is below a certain level it is anticipated that the particles could remain amorphous. This was observed with some powders although bright field - dark field TEM should be done to verify whether the powders are truly amorphous or if the degree of crystallinity is below the sensitivity of the X-ray diffractometer. If the particles are transformed from an amorphous solid, the degree of crystallinity will be related to the flame temperature and the particle cooling rate. The results of the ratio of the BET particle size to the X-ray crystallite size suggests that some of the powders are not fully crystalline. This occurs with powders synthesized at low pressures and with low reaction temperatures. At present, crystallization of the powder from amorphous particles appears to be the most likely explanation for the observed particle microstructures.

2. Silicon Nitride Powders

    a. General Characteristics

The characteristics of the Si_3N_4 powders match those which were sought
and are similar to the Si powders. The particles are smaller and more
uniform in diameter than was generally observed for Si powders. Like the Si
powders, the particles are spherically shaped and were found in chain-like
agglomerates. Generally purity levels are exceptionally high.

Under all process conditions examined, the SiH_4 conversion efficiency
exceeded 90% and was typically closer to 100%. Synthesis runs employed
excess NH_3 which was not recycled or captured.

Silicon nitride powders are fully dense and have smooth surfaces based
on BET/TEM analyses and He pycnometric density measurements. The directly
measured density (2.73 g/cm^3) agrees sufficiently with the calculated
density (2.8 g/cm^3) of non stoichiometric, amorphous Si_3N_4 to conclude the
particles have very little internal porosity. Additionally, no
microstructural features were observed by TEM which could be interpreted as
porosity. As was the case with Si powders, equivalent spherical diameters
calculated from BET measurements agreed closely with directly measured
diameters. Besides indicating that the particles are smooth, have no
externally accessable porosity and are round, this result qualitatively
shows that a narrow particle size distribution exists in agreement with TEM
observations.

Chemical analyses, Table 7 and Appendix II, show that the Si_3N_4 powders
are very pure. Total impurities revealed by emission spectroscopy are in
the range of 60 ppm by weight. The oxygen content usually varies from
0.3 to 2.0 wt % compared to a monolayer per particle which corresponds to
approximately 4.0 wt %. As for the Si powders, the oxygen contamination was
introduced during synthesis and handling and was thus subject to the
peculiarities of an individual run. Oxygen levels as low as 0.1 wt % were
achieved. Small amounts of H_2 from the reaction products were retained in
the powders.

TABLE 7

Chemical Analyses of Si_3N_4 Powders

Major Element (weight % of element)	Powder Lot	
	402SN	405SN
Si	62.40	57.30
N	30.55	37.95
Excess Si (weight % of total)	17.83	0.39
Impurity (ppm by weight)		
Al	10	10
Mg	5	3
Fe	10	5
Ca	20	15
Ni	5	3
Sn	10	5
Cu	5	2
O[*]	3397	3166

[*]Oxygen by Union Carbide, Tuxedo, N.Y., all others by Luvak, Boylston, MA.

The stoichiometry of the powders varied substantially depending on process conditions used. Initial powders produced contained 72 wt. % Si and 26 wt. % N compared with stoichiometric Si_3N_4 which contains 60 wt. % Si and 40 wt. % N. Process conditions which caused the powder composition shift toward the stoichiometric value are increased laser intensity, increased pressure and lower gas steam velocities. Variable NH_3/SiH_4 reactant ratios and Ar dilution had lesser effects on stoichiometry. Although these powders tend to be rich in Si, process conditions were defined which produced essentially stoichiometric powders. Based on extensive TEM characterization of as-synthesized and heat treated powders, it appears that the excess Si is distributed uniformly throughout the individual particles.

Virtually all process conditions produced Si_3N_4 powders which were amorphous to TEM and X-ray diffraction analyses. High laser intensities and high reactant gas pressures (run 221SN) resulted in stoichiometric, crystalline Si_3N_4 powders.

b. Powder Synthesis Experiments

i. Gas Velocity

Three experimental runs (4113SN, 4114SN and 4115SN) were performed to examine the effect of reactant gas velocity on the Si_3N_4 synthesis process and the resulting powder characteristics. In these runs, the cell pressure (0.75 atm), laser intensity (531 W/cm^2) and NH_3/SiH_4 ratio (2/1) were held constant. The total reactant gas flow rate was changed from 21.5 to 198 cm^3/min. The process conditions and resulting reaction zone and powder characteristics are summarized in Table 8.

As the reactant gas stream velocity was increased, the reaction zone temperature (by optical pyrometry) also increased, the BET equivalent particle size decreased slightly and the powders became more Si rich. Velocity had no effect on crystallinity.

ii. NH_3/SiH_4 Ratio

Synthesis runs were performed to investigate the effect of the NH_3/SiH_4 gas ratio on the reaction zone and particle characteristics. Earlier studies[3] (runs 614SN, 603SN and 615SN) examined only a small range of NH_3/SiH_4 ratios (5/1, 10/1 and 20/1, respectively). In later runs (4113SN, 4112SN, and 4111SN), the NH_3/SiH_4 ratio was changed from 2/1 to 43/1 while all other process parameters were held constant, e.g. cell pressure (0.75 atm), laser intensity (531 W/cm^2) and total reactant gas flow rate (198 cm^3/min). These runs are summarized in Table 9.

One of the major effects of changing the NH_3/SiH_4 ratio is to alter the absorptivity within the reactant gas stream since the absorption coefficient for SiH_4 at the wavelength of the laser emission is much larger than that for NH_3 (see Section IIIA). This effect will be discussed in terms of reactant gas heating rates in the following section. The reaction zone temperature, as determined by optical pyrometry, decreased as the NH_3/SiH_4 ratio was increased. The particle size also decreased as the NH_3/SiH_4 ratio

72

TABLE 8

The Influence of Reactant Gas Velocity on the Reaction Temperature
and Si_3N_4 Particle Characteristics*

Run	Total Reactant Gas Flow Rate (cm^3/min)	Av. Reactant Gas Velocity at Nozzle (cm/sec)	Temp.[≠] (°C)	Surf. Area (m^2/g)	Particle Diameter (Å)	Depletion Volume (cm^3)
4113SN	198	248	1400	79.8	268	2.3×10^{-13}
4114SN	66	83	1310	73.9	289	2.9×10^{-13}
4115SN	21.5	27	1260	68.4	312	3.7×10^{-13}

* For each run: Pressure = 0.75 atm, NH_3/SiH_4 ratio = 2/1,
Intensity = 531 W/cm^2.

≠ Uncorreted Pyrometric Temperature

TABLE 9

The Influence of NH_3/SiH_4 Ratio on the Reaction Temperature

and Si_3N_4 Powder Characteristics*

Run	NH_3/SiH_4 Ratio	Temperature[≠] (C°)	Surface Area (m^2/g)	Particle Diameter (Å)	Depletion Volume (cm^3)
4111SN	43	850	138	156	7.3×10^{-13}
4112SN	10	1030	87.5	244	6.4×10^{-13}
4113SN	2	1400	79.8	270	2.3×10^{-13}

* For each run: Pressure = 0.75 atm, Intensity = 531 W/cm^2,
Reactant Gas Flow Rate = 198 cm^3/min.

≠ Uncorrected Pyrometer Temperature

TABLE 10

The Influence of Laser Intensity on the Reaction Temperature
and Si_3N_4 Particle Characteristics

Run #	Laser Intensity (W/cm^2)	BET Particle Size (Å)	Free Si (wt %)	Reaction Temperature (°C)	Crystallinity	Depletion Volume (cm^3)
603SN	531	176	35	867	amorphous	1.1×10^{-12}
609SN	2×10^4	114	2	985 - 1020	amorphous	2.7×10^{-13}
621SN	1×10^5	98	very low	>1020	amorphous	6.5×10^{-14}

Uncorrected Pyrometric Temperature

TABLE 11

The Influence of Pressure on the Reaction Temperature
and Si_3N_4 Particle Characteristics

Run #	Pressure (atm)	BET Particle Size (Å)	Free Si (wt %)	Reaction Temperature (°C)	Crystallinity	Depletion Volume (cm^3)
611SN	0.08	167	60	-	amorphous	1.5×10^{-12}
603SN	0.2	176	35	867	amorphous	1.1×10^{-12}
610SN	0.5	211	14	1060 - 1080	amorphous	0.8×10^{-12}
023SN	0.75	220	23	1050 - 1125	amorphous	0.6×10^{-12}
021SN	0.75	221	15.6	-	amorphous	0.6×10^{-12}

Uncorrected Pyrometric Temperature

was increased. The relationship between the final particle size and both the density of silane molecules in the reactant gas stream and gas depletion volume will be discussed in the next section since the general correlation between Si_3N_4 particle size and reaction temperature is not followed in this case.

iii. Laser Intensity

Table 10 shows the effect of varying the laser intensity from 531 to 1×10^5 W/cm^2 on the powder size, reaction temperature, stoichiometry, and depletion volume. The higher intensities were achieved by focusing the beam with a 13 cm focal length lens. An increase in intensity caused a decrease in particle size measured by BET surface area and an increase in reaction zone temperature measured by optical pyrometry. It will be shown below that increased pressure raises the particle size; therefore the observed trend can be attributed to laser intensity. A direct comparison of the reaction temperatures is probably not valid since the change in aerosol emissivity from run to run has not been accounted for. The higher laser intensities resulted in a more stoichiometric powder. All Si_3N_4 powders produced under these conditions were amorphous to both X-ray and electron diffraction, despite significantly different reaction temperatures.

Changes in laser intensity had a large effect on the gas depletion volume. The decrease in V_{DEP} with increasing intensity, and therefore temperature, suggests that the nucleation rate exhibits a larger temperature dependence than the growth rate. The reduced depletion volume, with increasing intensity, results in a decrease in particle size. This behavior was directly opposite to that exhibited for silicon synthesis (see Section IIIClbii).

iv. Cell Pressure

The effects of variations in the cell pressure on the Si_3N_4 synthesis are shown in Table 11. An increase in pressure caused the Si_3N_4 particle

size to increase. This can be understood in relation to the depletion volume analysis. Over the pressure range examined, the distance between nuclei was shown to be approximately constant. The observed particle volumes are directly proportional to the mass of reactant gas within the depletion volumes and thus are directly proportional to pressure if the relative ratio of growth to nucleation rate remains constant. Direct comparison of the reaction temperatures is invalid since these temperatures were measured by optical pyrometry and therefore are related to density of particles and the particle volume within the reaction zone. The powder stoichiometry improved as the pressure was increased from 0.08 to 0.50 atm. All of these powders were amorphous to both X-ray and electron diffraction.

v. Amorphous and Crystalline Powders

The results discussed above indicated the powders became more nearly stoichiometric with increased laser intensity and pressure. It was anticipated that the high reaction temperature with a 2/1 NH_3/SiH_4 ratio should also result in improved stoichiometry. A run (221SN) was made specifically to test this projection. The run conditions were a pressure of 0.75 atm, a 170 W laser beam focused to an intensity of 2×10^4 W/cm^2, a 2/1 NH_3/SiH_4 ratio and a total reactant volumetric flow rate of 120 cm^3/min. This resulted in a very intense flame with a temperature of 1370 - 1410°C by pyrometry and 2140°C by the PMT-interference filter technique assuming an emissivity dependence of $1/\lambda$. X-ray diffraction indicated the powder was crystalline containing 38.0 wt. % α-Si_3N_4, 54.7 wt. % β-Si_3N_4 and 7.2 wt. % Si. A crystallite size of 250-360 Å was calculated from X-ray line broadening of the $\alpha(321)$, α (301), $\beta(320)$ and $\beta(002)$ Si_3N_4 peaks assuming Guassian peak shapes. The equivalent spherical particle size calculated from a BET surface area of 36.4 m^2/g was 517 Å, a much larger diameter than was observed for the amorphous Si_3N_4 powders. Chemical analysis revealed that the powder contains 55.3 wt. % Si, 35.3 wt. % N and 1.8 wt. % O.

Run 222SN was performed under identical conditions as Run 221SN except the NH_3/SiH_4 ratio was changed from 2/1 to 5/1. The reaction temperature

76

decreased to 1095-1120°C by pyrometry and 1928°C from the PMT-interference filter data assuming a $1/\lambda$ emissivity. The larger decrease in the pyrometer temperature is probably a result of a decrease in aerosol emissivity with a more dilute reaction zone. As in other runs, the decrease in reaction temperature resulted in a powder that was amorphous to X-ray diffraction. The BET surface area of 112 m^2/g (equivalent spherical diameter of 168 Å) is similar to other amorphous powders. The chemistry of this was virtually identical to the crystalline powder: 55.5 wt. % Si, 37.0 wt. % N and 1.9 wt. % 0.

The results of these two runs reveal the crystallinity of the powder is largely dependent upon the reaction temperature. The physical powder characteristics vary to a large degree depending on whether the powder is amorphous or crystalline.

c. Analysis and Discussion

i. Heating Rate

Figure 41 shows the effect of the NH_3/SiH_4 ratio on the calculated heating rates for reactant gas volume elements traveling along the central axis of the gas stream through the maximum laser intensity. The three curves correspond to run conditions 4111SN, 4112SN and 4113SN (Table 9). Both the instantaneous gas heating rate at the point where the reaction was initiated (estimated by measuring the position in the laser beam where the reaction flame begins) and the average gas heating rate up to this point increased as the NH_3/SiH_4 ratio is decreased. The position in the beam where the reaction was first observed was not measured for run 4111SN, but the heating rate analysis suggests that the reaction temperature for this run cannot be higher than 900K.

All of the calculated reaction temperatures for the Si_3N_4 synthesis process predicted by this heating rate analysis are lower than both the measured temperature (by optical pyrometry) and the spontaneous reported[21] reaction temperature of SiH_4/NH_3 gas mixtures. Our analysis does not
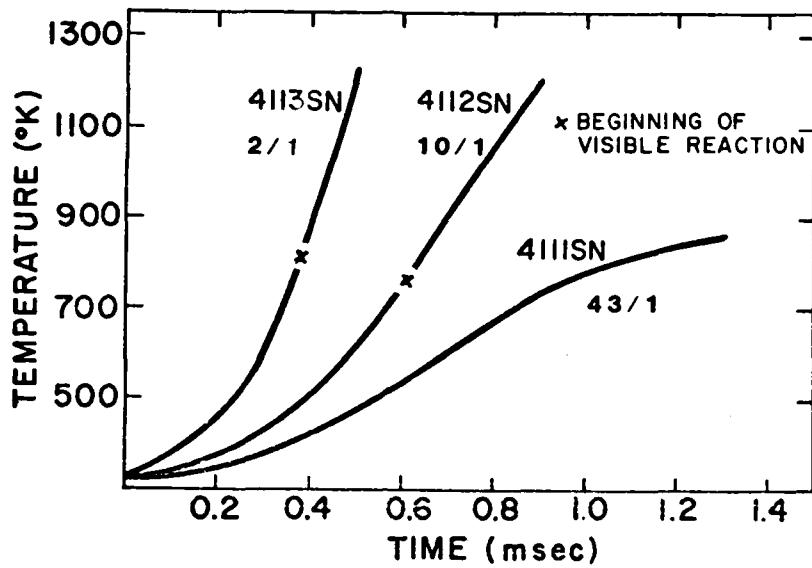
Figure 41. The effect of NH_3/SiH_4 ratio on the calculated temperature of the reactant gases during Si_3N_4 synthesis.
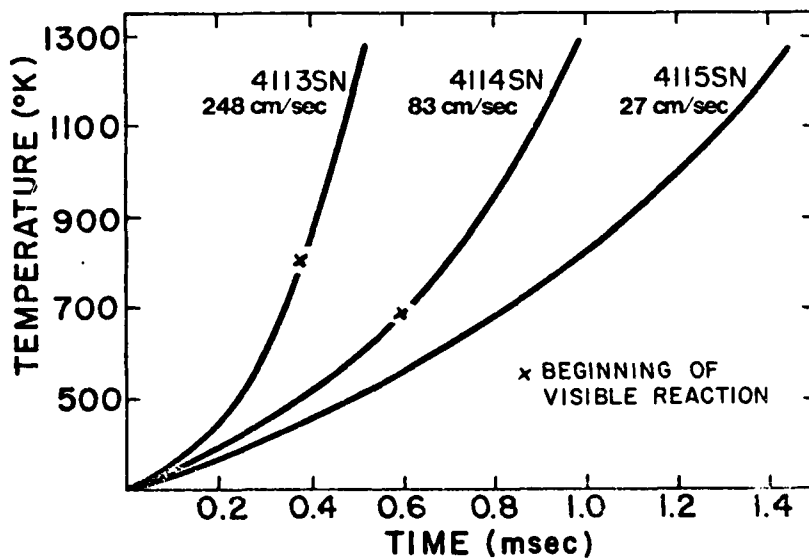
Figure 42. The effect of velocity on the calculated temperature of the reactant gases during Si_3N_4 synthesis.

include the effect of exothermic heat released during the reaction. Also, the quantitative validity of this analysis is limited primarily by the uncertainty in the values used for the reactant absorptivities. Nonetheless this analysis provides useful qualitative insight into the effect the process parameters have on the reactant gas heating rates.

Figure 42 shows the calculated effect of gas velocity on heating rates for reactant gas volume elements traveling along the central axis of the gas stream. Increasing velocity causes increases in both the average heating rate and instantaneous heating rate at the point where the reaction is initiated. In fact, for the slowest velocity (run 4115SN), the reaction was initiated so soon after the reactant gas entered the laser beam, that the beginning of the flame and the laser beam were nearly coincident. Thus, in this case, the gas was heated to the reaction temperature well before it experienced the maximum laser intensity.

In both sets of data, the calculated reation temperature was qualitatively consistent with the temperature measured by optical pyrometry. That is, the reaction temperature increased as the reactant gas velocity was increased or as the NH_3/SiH_4 ratio was decreased. Including the temperature increase due to the exothermic reaction and developing a better understanding of the reactant gas stream velocities and absorptivities should resolve the quantitative differences between the measured and calculated reaction temperatures.

ii. Depletion Volume

The calculated depletion volumes for two sets of Si_3N_4 synthesis runs are shown in Tables 8 and 9. These volumes were calculated by relating the mass of silicon in a single particle to the mass density of silicon atoms in the reactant gas stream. The particle density within the gas stream is inversely proportional to the depletion volume. If we assume that each nucleus grows independently, then the particle density is equal to the nucleus density providing a direct measure of nucleation rate within the reactant gas stream.

79

Examination of Table 8 shows that the depletion volume decreased slightly as the reactant gas stream velocity was increased. This result suggests that the nucleation rate increased slightly with increased velocity and the correspondingly increased reaction temperature.

Table 9 shows that the depletion volume increased as the NH_3/SiH_4 ratio was increased. Since the NH_3/SiH_4 ratio was changed at constant pressure, the density of silane molecules in the reactant gas stream was altered for each of these runs. This explains the observed particle size dependence. Even though the gas depletion volume increased with an increase in the NH_3/SiH_4 ratio, the molar density of silane in the gas stream decreased by a proportionally larger amount and thus the final particle size decreased.

Examination of Tables 8 and 9 shows that an increased reaction temperature produces a decrease in the depletion volume. This suggests that the nucleation rate increases at a proportionally larger amount than the growth rate as the reaction temperature is increased. This is the same as was observed previously[3] with Si_3N_4 and is opposite to that observed for the synthesis of silicon from pure SiH_4 and SiH_4/inert gas mixtures (see Section IIIC1c).

3. Silicon Carbide Powders

Synthesis experiments have been carried out to determine the feasibility of producing SiC powders from laser heated reactant gases. Silane was used as the silicon source as with other powders. Methane (CH_4) and ethylene (C_2H_4) were used as carbon sources. The proposed reactions for these experiments were:

$$SiH_4(g) + CH_4(g) \xrightarrow{h\nu} SiC(s) + 4H_2(g) \qquad (31)$$

and

$$2SiH_4(g) + C_2H_4(g) \xrightarrow{h\nu} 2SiC(s) + 6H_2(g) \ . \qquad (32)$$
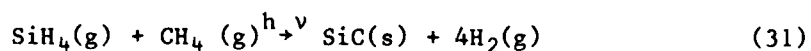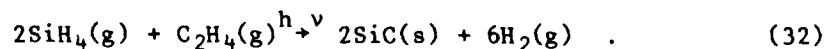
Methane was expected to react more readily than ethylene because of its simple molecular structure even though it has no absorption bands in the vicinity of 10.6 μm. More complete information suggests that methane pyrolyzes via an ethylene intermediate[36] so the initial hypothesis may not, in fact, be valid. Ethylene was selected because it was reported[37] to exhibit high absorptivity to the P(20) line of $00^\circ1 - 10^\circ0$ band in a CO_2 laser. They reported an absorptivity of 1.64 cm^{-1} atm^{-1} for dilute concentrations of ethylene in air. We measured an absorbtivity of 2.0 for pure ethylene. This absorptivity level is intermediate between measured levels of SiH_4 and NH_3 and is a very high absorptivity by comparison with other gases.

The process conditions used in these synthesis experiments are summarized in Table 12 along with the characteristics of resulting powders. In general, the process conditions were nearly the same as the reference conditions used for Si and Si_3N_4 powders. The gas mixtures had nearly stoichiometric silicon to carbon ratios.

TABLE 12

Summary of SiC Process Conditions and Powder Characteristics

Gases	$SiH_4 + CH_4$	$SiH_4 + C_2H_4$
Cell Pressure (atm)	0.2	0.2
Laser Intensity (W/cm^2)	561	601
Reaction Temperature ($^\circ$C)$^{\neq}$	710	865
Powder Chemistry (wt%)		
Si	99	80
C	0.2	14
O_2	0.3	1.4
Powder Size		
BET Equivalent (Å)	305	274
TEM (Å)	–	230
Powder Crystallinity		
X-ray	crystalline Si	p .
Electron Diffraction	crystalline Si	

$^{\neq}$ Uncorrected Pyrometric Temperature

The physical characteristics of resulting powders are similar to those observed with Si and Si_3N_4 powders. TEM analysis showed them to be small, uniform, loosely agglomerated spheres. The particles ranged from 180 Å to 260 Å with an average size of 210 Å. BET equivalent diameters and directly measured diameters were essentially equal to each other; again, indicating an absence of internal porosity which was open to the surface of the particles.

Chemical analysis showed that the powders formed with CH_4 contained virtually no carbon. The methane apparently did not react with the time-temperature history caused by exposure to the laser beam. Those formed with C_2H_4 were primarily SiC with up to 10 wt. % C and/or Si. IR spectral analysis indicated that carbon combined as SiC in these powders, although we have not determined whether all of the carbon was combined in this manner.

The powders made from SiH_4 and CH_4 (613SC) were crystalline to both X-ray and electron diffraction. The diffraction patterns were identical to those for Si powder made from SiH_4. The powders from SiH_4 and C_2H_4 runs showed evidence of crystallinity in both electron and X-ray diffraction. The patterns correspond to predominantly β-SiC and in some cases small amounts of crystalline Si. The crystallite size for these powders, determined from X-ray line broadening, is generally smaller than the BET equivalent spherical diameter $\frac{d \text{ BET}}{d \text{ X-ray}} \approx 2$.

It is not known whether the higher reactivity of the C_2H_4 gas resulted primarily because of its higher optical absorptivity, an intrinsically high reactivity with silane, or some combination of factors. It is interesting to speculate whether resonance effects between the photons and the gas molecules enhanced the reaction. The optical absorptivity of the gas containing ethylene improved the coupling efficiency relative to the CH_4/SiH_4 gas mixture in which the CH_4 acted as an optical dilutant and as shown in Table 12, the measured reaction temperature was higher with C_2H_4 than with CH_4. Although the measured temperature levels probably are not accurate, the relative levels are likely to be correct. So the cause for the higher reactivity of C_2H_4 may simply result from a higher temperature at

the point of reaction, attributable to the higher optical absorptivity. If this is so, higher laser intensities should cause CH_4 to react with SiH_4. Higher reactant gas pressures should also improve the stoichiometry of the powders.

The question of possible resonance effects on reactions is fundamentally important for understanding, controlling, and exploiting this laser synthesis process. If they are important, unusual reaction paths and kinetics will be possible. It may also be possible to cause reactions in the presence of unwanted impurities which will not be incorporated proportionally if they do not couple to the laser light. If resonance effects do not occur, it will be correct to describe the reaction as a very fast "thermal domain" reaction as we are now doing.

4. Particle Agglomeration

TEM analysis has shown that all of the laser synthesized powders (Si, Si_3N_4 and SiC) exhibit agglomeration characterized by two-dimensional, chain-like networks of particles. The majority of the Si powders also appear to have neck formation between the particles. This necking has not been observed in the Si_3N_4 or SiC powders.

When fine particles collide, van der Waals forces will act to join the particles and form agglomerates. Once contact is made between the particles, additional forces may make their separation difficult. Contacting particles can reduce their exposed surface by deforming, creating a contact area between them. The decrease in surface energy acts as a bond. The radius of the contact area can be estimated by assuming elastic deformation. If material is actually transferred from the particles to the neck region between the joined particles by either diffusional or evaporation-condensation mechanisms, a sintered aggregate may be formed. Two theoretical situations have been examined to investigate the agglomeration issue: frequency of particle collisions and the neck formation between the particles by elastic deformation due to a decrease in the surface free energy.

a. Particle Collisions

Brownian motion and fluid shear are two principle mechanisms by which particle collisions can occur. Each of these collision rates can be influenced by inter-particle forces such as van der Waals forces and Coulombic forces.

i. Collisions Induced by Brownian Motion

For particles that are much smaller than the mean free path of the gas molecules, the collision frequency due to Brownian motion is:[33]

$$F(t) = \left(\frac{192 \ kTr}{\rho}\right)^{1/2} N \qquad (33)$$

where: ρ is the particle density (g/cm^3)

k is Boltzmann's constant

r is the particle radius (cm)

T is absolute temperature (°K)

N is the particle density within the gas steam (#/cm^3)

and   F(t) is the collision frequency of a single particle (#/sec).

The mean free path in argon at 1100K and 0.2 atm (approximately 1.67×10^{-4} cm) is one to two orders of magnitude larger than the typical particle size. Thus the use of the above expression for the collision frequency is justified.

For silicon synthesis using the run conditions identical to 631S, $r = 3.025 \times 10^{-6}$ cm, $\rho = 2.33$ g/cm^3, $N = 1.66 \times 10^{11}$ particle/cm^3, $k = 1.38 \times 10^{-16}$ erg/°K, and $T = 1323$K, the collision frequency is 1120 collisions/ particle • sec. Under these run conditions, the average flow velocity is estimated to be 100 cm/sec and the dwell time of the particles in the flame is 2.4×10^{-2} sec. Thus on the average, a particle will

undergo approximately 27 collisions while in the flame and approximately 33 additional collisions before reaching the filter. Van der Waals forces are estimated to increase the collision frequency[38] by a factor of 1.152.

ii. Collisions Induced by Fluid Shear

In the orthokinetic case, particles flowing in a fluid stream collide because of their relative motion. The collision frequency is given by the following expression:[39]

$$F(t) = \frac{32}{3} r^3 N \frac{du}{dx} \qquad (34)$$

where $\frac{du}{dx}$ is the velocity gradient across the gas stream. The parameters N, r, and F(t) are the same as above. For the Si synthesis conditions used in run 631S, $\frac{du}{dx}$ is estimated from computer results to be 1×10^3 cm/sec · cm. Using the same N and r values given above yields a collision frequency, F(t), of approximately 4.9×10^{-2} collisions/particle · sec. This indicates that collisions by Brownian motion will dominate.

iii. Effect of Process Variables on Collision Frequency

The particle density in the gas stream is the parameter which dominates the collision frequency caused by Brownian motion. Reaction temperature and particle radius will have less of an effect since the collision frequency has a square root dependence on them. Increased gas stream velocity should reduce the total number of collisions a particle undergoes since the residence time is reduced proportionally.

It was anticipated that diluting the reactant gas stream with argon would decrease the collision frequency by the combined effects of reducing the reaction temperature and the particle density. Runs 631S, 634S and 637S investigated this effect with silane and silane-argon mixtures. Table 13 gives the calculated collision frequency for these three runs. The total

TABLE 13

Calculated Collision Frequency Caused by Brownian Motion

Run	Ar (mole %)	$T^{\neq}$ (°K)	r (cm)	N $\dfrac{\text{particles}}{\text{cm}^3}$	$F(t)$ $\dfrac{\text{collisons}}{\text{particle} \cdot \text{sec}}$
631S	0	1323	3.025×10^{-6}	1.66×10^{11}	1120
634S	0.833	1032	1.47×10^{-6}	2.86×10^{11}	1183
637S	0.667	1103	1.80×10^{-6}	2.93×10^{11}	1392

$^{\neq}$ Uncorrected Pyrometric Temperature

number of collisions a particle experiences is porportional to the collision frequency since the flow velocity is the same for all three runs.

Table 13 shows that the collision fequency did not change significantly with dilution of the gas stream. Even though the reaction temperature decreased as the gas stream was diluted, an effect which by itself would reduce the collision frequency, the density of particles in the gas stream increased because the particles were smaller. Consequently, the collision frequency was not greatly affected by dilution of the gas stream.

    b. Neck Formation between Particles.

Many of the TEM micrographs show the formation of necks between silicon particles. The fraction of the neck radius which results from cold sintering under the influence of surface forces can be estimated. In this calculation, it is assumed that the necks form by elastic deformation due to surface tension forces. A force balance is used to calculate the resulting radius size. The ratio of the radius of contact area, x, to the particle radius, r, is given by:[40]

$$\frac{x}{r} = \left(\frac{\gamma_{eff}}{0.16 \text{ Er}} \right)^{1/3} \qquad (35)$$

with

$$\gamma_{eff} = 2 \gamma_{sv} - \gamma_{ss} \qquad (36)$$

where: γ_{eff} = effective interfacial energy

γ_{sv} = interfacial energy between the solid and the vapor phase

γ_{ss} = the grain boundary energy

E = Young's modulus.

The interfacial energy and grain boundary energy are related by the following expression:[41]

$$\gamma_{ss} = 2 \gamma_{sv} \cos (\phi/2) \tag{37}$$

where ϕ is the angle of the grain boundary groove. Combining these equations gives:

$$\frac{x}{r} = \left(\frac{2 \gamma_{sv}(1-\cos \phi/2)}{0.16 \, Er} \right)^{1/3} \tag{38}$$

Using the following values:[41]

ϕ = 150°

γ_{sv} = 900 ergs/cm^2

E = 1.63 x 10^{12} dynes/cm^2

r = 2 x 10^{-6} cm

x/r = 0.108.

This gives a neck diameter of 43 Å for a 400 Å particle, indicating significant neck formation can arise simply from surface forces. Qualitatively, this size is in agreement with observations. Presumably, these necks can be broken by a proper dispersing agent since no bonding has occurred between the particles. Additional neck formation can arise through sintering mechanisms such as evaporation-condensation, surface diffusion, lattice diffusion and grain boundary diffusion. These bonds can not be broken by dispersing agents.

IV. POWDER PROCESSING

A. Powder Dispersion

To produce uniform, dense compacts by processes in which the powder is suspended in a liquid medium, it is essential to create a stable powder dispersion and to rid the powder of agglomerates. It is generally possible to form high quality parts by slip casting, settling or by centrifugal casting from this dipsersed condition. For the special case of using uniform sized spherical powders, it should be possible to create the ordered structures shown in Figure 1. Dispersion experiments were initiated with Si powders to serve as a basis for these fabrication processes. This study is directed toward forming parts of reaction bonded silicon nitride (RBSN).

Early studies on the dispersability of silicon were reported near the beginning of the century. Weiser[4] first reported forming a hydrosol of thoroughly pulverized silicon by treating the powder alternately with acid and alkali. Wegelin[43] also prepared hydrosols of silicon, but by mechanical grinding. Astfalk and Gutbier[44] investigated chemical preparation of colloidal silicon by reduction of silicon dioxide with magnesium. After grinding and washing the product with hydrochloric acid, they obtained a weak, unstable sol in some cases and, in others, a more concentrated fairly stable sol.

Our initial studies showed that aqueous media have two disadvantages with the laser synthesized Si powders: (1) oxidation of these fine powders is difficult to prevent during drying and (2) when cast from aqueous suspensions, silicon tends to gel, making subsequent elimination of water difficult. We have, therefore, chosen to study dispersions of silicon in various organic solvents. Besides not forming gels, these liquids have the added advantage of being sufficiently volatile that they may be easily eliminated during drying. We have avoided the use of deflocculants because they are difficult to eliminate.

Special care must be taken to control the processing atmosphere because the presence of oxygen influences the wetting properties of powder in the

89

dispersion process. According to Williams and Goodman,[45] a single crystal silicon wafer is oxidized immediately when exposed to air and the resulting SiO_2 layer greatly affects the wetting characteristics. In previous investigations on silicon dispersion, the experiments were performed in uncontrolled atmospheres, so there is some ambiguity in the meaning of the results.

1. Experimental

a. Materials

The silicon powder used in this study was synthesized from the laser driven decomposition of $SiH_4(g)$ under the reference conditions given in Appendix I. Single point BET measurement showed the surface area to be 55 m^2/g, corresponding to an equivalent spherical diameter of 465 Å. Neutron activation analysis indicated 0.14 wt % oxygen and spectroscopic analysis indicated < 30 ppm of all other elements. Commercially available grades of the organic liquids were used in this study. The purity specifications for these are given in Table 14. Selected physical properties are given in Table 15. Liquids were chosen from as many families as possible. They include aliphatic hydrocarbons, cyclo-aliphatic hydrocarbons, members of the benzene group, alcohols, ketones, ether, aliphatic acids, aldehyde and water. The single crystal silicon wafer, used for contact angle measurements was boron doped to a level of $10^{17}/cm^3$.

b. Dispersion Test

A simple screening test was used to determine the wetting behavior and the suspension stability of Si powder in the various liquids. The dispersion test was performed by introducing a small amount of silicon powder (100 mg) under glove box conditions into a glass bottle sealed with a thin rubber diaphram. Then, each of the liquids (15cc) was injected through the rubber stopper into the bottle with a syringe. This avoided introducing

90

TABLE 14

Grades and Impurities of the Liquids Used

No.	Liquid	Supplier	Grade	Main Impurities
	Aliphatic Hydrocarbons			
1	n-Hexane	Fisher	Certified	Sulfur Compound, 0.002%
2	Cyclohexane	Mallinckrodt	Analytical	
3	n-Octane	J.T. Baker	Baker	
	Benzene Group			
4	Benzene	Mallinckrodt	Analytical	
5	Toluene	J.T. Baker	Reagent	Sulfur Compound, 0.002%
6	Xylene	Fisher	Cert. (UV)	Sulfur Compound, 0.0006%
	Alcohols			
7	Methanol	Mallinckrodt	Absolute	$(CH_3)_2CO$, 0.001%; CH_3COOH, 0.0018%; Water, 0.02%
8	Ethanol	U.S. Indust.	Absolute	
9	n-Propanol	Mallinckrodt	Analytical	CH_3COOH, 0.015%
10	Isopropanol	Fisher	Certified	Water, 0.1%
11	n-Butanol	Mallinckrodt	Reagent	CH_3COOH 0.001%; Butyl-Ether, <0.02%; Water, 0.05%
12	n-Heptanol	Eastman		
13	n-Octanol	Fisher	Certified	$C_7H_{15}COOH$, 0.01%
14	Benzyl Alcohol	Mallinckrodt	Analytical	C_6H_5CHO, 0.2%
15	Ethylene Glycol	Fisher	Certified	CH_3COOH, 0.004%; Water, 0.2%
	Ketones			
16	Acetone	Mallinckrodt	Analytical	CH_3OH, 0.01%; $(CH_3)_2CHOH$, 0.005%; Water, 0.3%
17	2-Pentanone	J.T. Baker	Baker	
18	2-Heptanone	Aldrich		
	Ether			
19	Isopentyl Ether	J.T. Baker	Baker	
	Aliphatic Acids			
20	Propionic Acid	Fisher	Certified	Water, 0.1%
21	Butyric Acid	Eastman		
	Aldehydes			
22	Benzaldehyde	Baker	Reagent	

TABLE 15

Physical Properties of Liquids*

No.	Liquid	Dielectric Constant[7]	Vapor-Liquid Surface Tension[8] (mN/m)	Boiling Point[7] (°C)	Viscosity[7] (cPoise)
	Aliphatic Hydrocarbons				
1	n-Hexane	1.89 a	18.4 a	69.0	0.326 a
2	Cyclohexane	2.02 a	25.2 a	80.7	1.02 b
3	n-Octane	1.95 a	21.6 a	125.7	0.542 a
	Benzene Group				
4	Benzene	2.28 a	28.9 a	80.1	0.652 a
5	Toluene	2.4 c	28.5 a	110.6	0.590 a
6	Xylene	2.3-2.5 a	28-30 a	138-145	0.62-0.81 a
	Alcohols				
7	Methanol	32.6 c	22.5 a	65.0	0.597 a
8	Ethanol	24.3 c	22.4 a	78.5	1.200 a
9	n-Propanol	20.1 c	23.7 a	97.4	2.256 a
10	Isopropanol	18.3 c	21.3 a	82.4	2.86 d
11	n-Butanol	17.8 a	25.4 a	117.3	2.948 a
12	n-Heptanol	-	-	176	8.53 d
13	n-Octanol	10.3 a	27.5 a	194.5	10.6 d
14	Benzyl Alcohol	13.1 a	35.5 a	205.4	5.8 a
15	Ethylene Glycol	38.7 a	48.4 a	197.5	20.5 a
	Ketones				
16	Acetone	20.7 c	25.1 a	56.2	0.316 c
17	2-Pentanone	15.4 a	23.6 a	102	-
18	2-Heptanone	9.8 a	26.7 a	151.5	-
	Ether				
19	Isopentyl Ether	2.82 a	22.9 a	173.2	-
	Aliphatic Acids				
20	Propionic Acid	3.30 e	26.7 a	141.0	1.10 a
21	Butyric Acid	2.97 a	26.5 a	163.5	1.54 a
	Aldehydes				
22	Benzaldehyde	17.8 a	38.5 a	178.1	1.395 c
	Inorganic				
23	Water	78.5 c	72.75 a	100.0	1.002 a

* Temperature (°C) at which measurement was made:
a = 20°, b = 17°, c = 25°, d = 15°, e = 10°.

the liquids into the glove box. The mixture was lightly shaken and observed. All systems which incorporated the powder were subjected to an ultrasonic probe for three minutes to mix them thoroughly. After standing for 5 days, the suspensions were observed again. The results are discussed in the following section.

n-Propanol was selected for further testing based on the results of the mixing tests, contact angle measurements and its low surface tension. Samples were prepared using the following three methods.

• Hand mixing by shaking: A small amount of silicon powder ($\sim$ 1 mg) and n-proponol (10 ml) were mixed in a glass bottle in an N_2 atmosphere. The mixture was lightly shaken by hand and diluted to convenient concentrations for particle size measurements.

• Ultrasonic agitation: The powder suspensions were subjected to an ultrasonic probe to enhance wetting, dispersion, and fragmentation of agglomerates. While in a 25 ml beaker, the suspension was subjected to the ultrasonic probe at 150 watts input power with a 1/2 inch diameter disruptor horn and 150 watts input power with a microtip. The suspension was cooled with a dry ice-propanol mixture during agitation. The effects of the ultrasonic treatment on the agglomerate size were examined by several techniques.

• Centrifugal separation of agglomerates: After mixing 500 mg of powder and 15 ml of n-propanol, the suspension was subjected to the ultrasonic probe for 3 minutes. The large agglomerates were removed by centrifugal separation at 12,000 rpm for 10 minutes. This removed approximately one half the powder. The Stokes' Law equivalent spherical diameter of the largest agglomerates still in suspension after this treatment is 260 nm. Then the supernatant of the first centrifuge was recentrifuged at 17,000 rpm for 2 hours. The supernatant of the second separation process contained very little powder but added a tan color to the dispersion. Particle size measurements were also made for this supernatant. The material cast from the second centrifuge was examined by SEM to determine its uniformity.

c. Contact Angle Measurement

The contact angle formed by a sessile drop of representative liquids on single crystal silicon was measured to provide a basis for comparing the mixing test results of Table 16 with surface properties of silicon. The silicon wafer, the surface of which was assumed to be initially oxidized, was cleaned in the following manner: after ultrasonic cleaning in trichloroethylene for 5 minutes, in acetone for 5 minutes, in methanol for 5 minutes and in distilled water for 5 minutes, the silicon wafer was put in a hydrofluoric acid solution (2.9 mol/l) for 5 minutes. The HF solution was then removed by successive dilutions with distilled water while blowing nitrogen into the solution until only distilled water remained. Under glove box conditions, the cleaned, etched and dried silicon wafer was immediately placed into a sealed chamber with an optical glass window and rubber stopper on the top, so that subsequent measurements were made in a nitrogen atmosphere.

After putting a drop (0.01 ml) of the liquid to be tested onto the wafer through the rubber stopper with a microsyringe, measurements were made at 23°C with a contact angle goniometer.

2. Results of Dispersion Test

a. Screening Tests

Three types of behavior were observed during the dispersion tests (Table 16). These are:
• Good Dispersion (designated A): most of the particles remained well dispersed after several days. This phenomenon was observed for liquids with high dielectric constants such as aliphatic alcohol, benzyl alcohol, ketones and benzaldehyde.
• Poor Dispersion (designated B): most of the particles settled out of the suspension within one hour. This phenomenon was observed for liquids with very low dielectric constants such as n-hexane, cyclohexane, n-octane, benzene, toluene, xylene, isopentyl ether, propionic and butyric acid.

94

TABLE 16

Results of The Dispersion Test and The Contant Angle Measurements

		Dispersion Test Results	Contact Angle
Aliphatic Hydrocarbons			
1	n-Hexane	B	0°
2	Cyclohexane	B	*
3	n-Octane	B	0°
	Benzene Group		
4	Benzene	B	0°
5	Toluene	B	0°
6	Xylene	B	*
	Alcohols		
7	Methanol	A	0°
8	Ethanol	A	*
9	n-Propanol	A	0°
10	Isopropanol	A	*
11	n-Butanol	A	*
12	n-Heptanol	A	*
13	n-Octanol	A	0°
14	Benzyl Alcohol	A	14°
15	Ethylene Glycol	A	45°
	Ketones		
16	Acetone	A	0°
17	2-Pentanone	A	0°
18	2-Heptanone	A	0°
	Ether		
19	Isopentyl Ether	B	*
	Aliphatic Acids		
20	Propionic Acid	B	0°
21	Butyric Acid	B	*
	Aldehydes		
22	Benzaldehyde	A	6°
	Inorganic		
23	Water	C	78°

A: good dispersion, no change and no precipitation after several days;
B: poor dispersion and settling; C: flotation

*

Not Measured

95

• Particle Flotation (designated C): all the silicon powder completely floated on the liquid surface. The particles could not be incorporated into the liquid even after vigorous agitation. This phenomenon was observed only for water. It is noteworthy that if the powder was exposed to air for several hours before mixing, it was easily wetted by water.

Among the good dispersing liquids (designated A) some are considered less desirable than others based on other properties. Methanol and acetone are very volatile. Butanol, heptanol, octanol, benzyl alcohol and ethylene glycol have high viscosities and consequently may be difficult to remove from the powder. Benzaldehyde is chemically unstable. n-Propanol was chosen for subsequent experiments since it generally has the most acceptable combination of properties and it has the lowest surface tension of the group.

b. Contact Angle Measurements

Contact angle results are shown in Table 16. Zero values are found for liquids with surface tensions less than 30 mN/m. Non-zero values were measured for higher surface tension liquids like benzyl alcohol, ethylene glycol, benzaldehyde and water.
Our measured contact angle for water (78°) is smaller than that reported by Williams and Goodman[45] (85-88°), which was measured in pure water and an HF solution by the bubble method. The smaller value of the angle we measured is likely due to slight oxidation of the silicon wafer surface during handling in the glove box. Using the experimentally measured relationship between contact angles and oxide thickness reported by Williams and Goodman[45], 78° corresponds to 2-3 Å thick oxide layer. Since the atmosphere is controlled to less than 10 ppm oxygen in this experiment, this level of oxidation is considered possible.

c. State of Agglomeration

The state of agglomeration of Si powder in n-propanol was evaluated by three techniques. Results are shown in Table 17. The techniques are:

TABLE 17

State of Powder Agglomeration in n-Propanol Determined
by Several Techniques

	Light Scattering Analysis		TEM		Laser Doppler Analysis	
	Dissymetry Factor, Z	Corresponding Particle Diameter (Å)	Size (Å)		Particle Diameter	Dispersion Factor
			Max.	Min.	(Å)	
Suspension Mixed by Shaking	>2.5	–	6200	4400	8000	8
Suspersion Subjected to Ultrasonic Disruption	2.67	–	4200	2000	2000	4
Supernatant from second Centrifugation	1.05	500	550	500	500	3

• TEM – Specimens were prepared by dipping carbon coated TEM grids in suspensions of approximately 1×10^{-4} moles Si/liter. Excess suspension was removed by drawing off liquid with the edge of an absorbant paper. Agglomerates of particles were spaced several hundred diameters apart on the grid so agglomeration during drying was not important.

• Laser Doppler particle size analysis – The state of agglomeration was measured by laser Doppler particle size analysis and the results are given in Table 17. This technique evaluates the equivalent particle diameter based on the velocity of Brownian motion. The diameters agree quite well with those determined by TEM. The dispersion factor is a qualitative measure of the width of the particle size distribution on a scale from 1 (narrow distribution) to 10 (wide distribution).

• Light scattering – Light scattering measurements were performed with a Universal Light Scattering Photometer. The intensity of light scattered

from the supernatant after the second centrifugation is shown in Figure 43 as a function of viewing angle. Theoretical curves calculated from Rayleigh scattering theory are placed in an arbitrary position on the figure since the concentrations needed for calculations were unknown. This theory is applicable for the case of particles that are uniform in size and are smaller than 1/20 of the wavelength of the light. For this case, the angular scattering profile for the vertically and horizontally polarized light differ since isotropic scattering polarizes the incident light. As shown in Figure 43, this causes the scattered intensity of the horizontal polarization to vary as $\cos^2\theta$, while the vertical component is independent of scattering angle. Although there are deviations between the shapes of the theoretical and experimental curves, the Rayleigh scattering model represents the experimental curves quite well.

To insure that a single-particle rather than multiple-particle scattering occurs, measurements were also made as a function of the supernatant concentration. The intensity ratio ($I_{90°}/I_{0°}$) varied in a linear manner with concentration, indicating that single-particle scattering is dominant. For multiple-particle scattering at higher concentrations, intensity increases less rapidly.

The agglomerate size can be determined by measurement of the dissymetry factor[46] provided the shape of the particle or agglomerate is known. This is given by:

$$Z_{45°} = \frac{\left(\dfrac{I_{45°}}{I_{0°}}\right)_{suspension} - \left(\dfrac{I_{45°}}{I_{0°}}\right)_{solvent}}{\left(\dfrac{I_{135°}}{I_{0°}}\right)_{suspension} - \left(\dfrac{I_{135°}}{I_{0°}}\right)_{solvent}} \qquad (39)$$

where the I's are the light intensities measured at the indicated angles. This technique gives average aggregate sizes independent of particle refractive index, provided their shapes are known. It looses some accuracy at values of Z much larger than 2 since the values tend to be more dependent

98
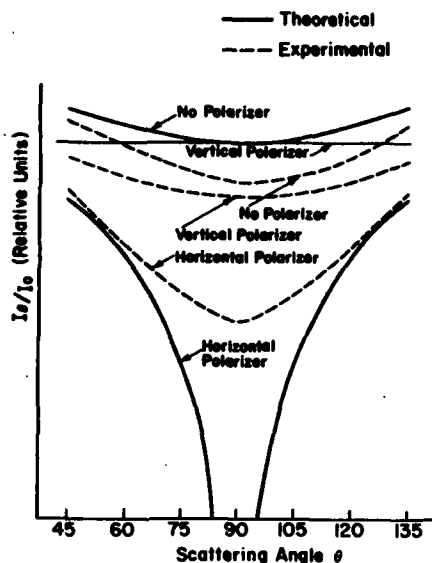
Figure 43. Light scattering as a function of viewing angle for Rayleigh type scatterers.
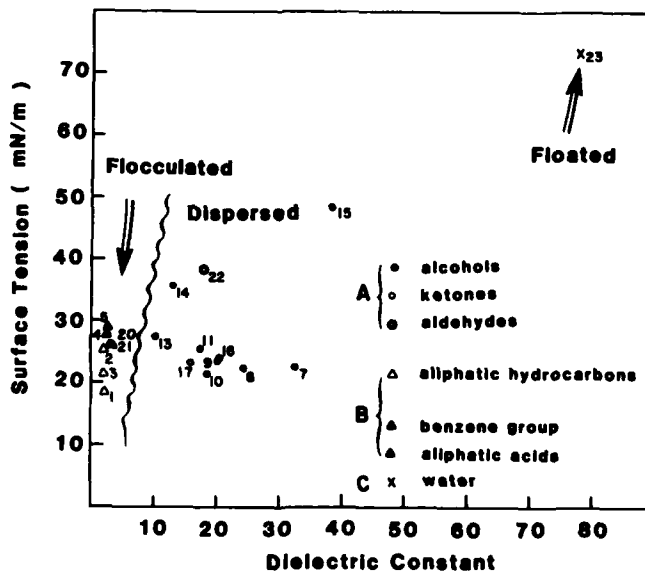
Figure 44. Correlation between dispersing characteristics and the liquid-vapor surface tensions and dielectric constants of solvents tested for forming stable dispersions of silicon powder.

on chain stiffness, non-Gaussian chain branching, etc.[46] The dissymetry
factor, Z, for the second supernatent (Table 17) was calculated to be 1.05.
Assuming a spherical shape, light scattering indicates a particle diameter
of 500 Å. This result agrees with BET and TEM techniques. The supernatent
of the suspension after the first centrifugation had a Z value of 1.83
indicating an equivalent spherical diameter of 1640 Å. This indicates
agglomerates are made up of 2 or 3 particles. Values of Z near 2.5 were
found for suspensions with a variety of larger agglomerate sizes as
determined by TEM. Apparently the dissymetry factor Z becomes insensitive
to size above Z $\cong$ 2.5. Light scattering may be used to determine the sizes
and shapes of larger agglomerates but requires the use of more complex
analyses usually performed by a computer.[47]

3. Discussion

The results of the dispersion tests were plotted with respect to the
surface tension and dielectric constant of the liquids since these two
parameters were found to be significant factors with respect to the wetting
and dispersion of silicon. The results are given in Figure 44. Based on
the contact angle results and the surface tension-dielectric constant
diagram, wetting and dispersion properties of silicon are summarized as
follows:

• Higher surface tension liquids (>30 mN/m, e.g. water, benzyldehyde,
ethylene glycol, and benzyl alcohol) exhibited non-zero contact angles.
However, particle flotation was only observed for water, which has an
extremely high surface tension. The other three liquids, for which $\theta \neq 0$,
did not float the powder. It is possible that the agglomerates were not
fully wetted by the liquids, and thus these three may be less favorable than
lower alcohols or ketones which exhibit a zero contact angle.

• Poor dispersion took place for liquids with a low dielectric constant,
(κ < 5, e.g. aliphatic hydrocarbons, liquids of the benzene group, ether,
and acids) for all values of surface tension. The absence of dispersion
once the powder is wetted is directly related to the silicon-liquid surface

100

tension and not to the liquid-vapor surface tension. These results suggest that poor dispersion occurs because of high liquid-solid surface tensions for these liquids.

• Liquids with high dielectric constants are concluded to be the ideal dispersing media. The surface tension of the liquid should be as low as possible to allow immersion and full penetration of the agglomerates by the liquid.

Analyses of the supernatants shows that the linear agglomerates observed in the Si powders can be broken up substantially. After centrifuging the ultrasonically treated dispersion, approximately one-half of the powder consisted of agglomerates consisting of 2-3 particles. This is a substantial improvement over the starting powders and should permit slip and centrifugal casting processes to be used. Achievement of the ordered structures shown in Figure 1 requires complete dispersion.

In our interpretation, we have considered flotation and poor dispersion as separate phenomenon, however, each of these aspects of poor wetting is presumed to be related to a unifying phenomenon. If so, these two behaviors should be interpretable in terms of more suitable factors such as spreading coefficient, polarizability, or a more complex function of surface tension and dielectric constant. We are unable to develop this model at this time, thus, we have presented this data as an empirical observation (Figure 44). It does have considerable value in the selection of dispersing agents for silicon.

B. Sample Fabrication

1. Objectives and General Approach

The development of powder processing techniques followed the powder synthesis research in the program. We concentrated on developing handling procedures which avoid contamination and on techniques for packing powders that produce uniform, dense compacts. The difficulties in producing high uniform density green compacts are problems which are inherent to using

fine powders. Both conventional and unconventional methods of compacting pieces made up of fine particles were explored. Controlling the characteristics in the green state are extremely important, because defects in the green microstructures are not expected to be eliminated and may even be magnified during later processing steps. Two types of powder compaction were used: conventional uniaxial pressing, with subsequent isostatic pressing, and centrifugal casting. The equipment used for the powder pressing is set up within the glove box. Sintering samples were placed within sealed ceramic tubes within the glove box and then transferred to outside furnaces where they were fired without any exposure to an air atmosphere.

2. Experiments

a. Cold Pressing and Isostatic Pressing

Samples prepared by cold pressing followed by isostatic pressing permitted evaluation of sintering, nitriding, crystallization kinetics, microstructural characterizations and strength measurements. It is recognized that it is difficult to achieve superior characteristics in pieces fabricated by these techniques because the powders are so fine. However, results did indicate that, despite small density heterogeneities, reasonable densities and final void sizes less than 1.0 μm could be achieved, so these shaping techniques may prove technologically useful.

Pellets that were cold pressed in the glove box at pressure levels up to 45,000 psi (single action die, diameter = 1/2 inch) contained laminations. It was found that the combination of cold pressing at lower pressures with subsequent isostatic pressing produced pellets with both adequate and uniform densities. Pellets were first cold pressed at 1000 psi. After cold pressing, the pellets were sealed in double evacuated isopressing bags and then isostatically pressed at 45,000 psi. All processing steps, except isostatic pressing, were carried out in the glove box.

These procedures yielded Si pellets with green densities between 0.95 to 1.15 g/cm^3 (40-49% of theoretical). The green densities of Si$_3$N$_4$ pellets were typically 1.1 g/cm^3 (35% of theoretical). As will be discussed in Sections IVC and IVD, the resulting Si pellets densified and reacted uniformly to produce pieces having microstructural features with scales approaching those of the constituent powders.

b. Centrifugal Casting

Casting of powders from suspensions offers the possibility of achieving very uniformly packed, dense green compacts. Experimentally, monodispersed spherical powders in a sol have been settled to ordered structures much like FCC or HCP packing of atoms in a lattice.[48,49] The resultant density approaches 74% of the theoretical. These centrifugal casting experiments also provide an expedient means of evaluating the degree to which powders are dispersed.

To obtain dense, uniform compacts by casting as shown in Figure 1, it is necessary to achieve dispersions of non-agglomerated powders. Experimentally, first, the liquid must wet the powder, second, agglomerates must either be broken up or removed, and third, the powder must be uniformly dispersed in the liquid. These issues have been investigated and were discussed in Section IVA. Having achieved these dispersions, the powder either must be settled or slip cast to form a dense cake. For very fine powders, centrifugal casting is used to reduce the settling time to a reasonable value.

Several types of powder suspensions were centrifugally cast to permit the characteristics of the compact to be observed. Casting was performed in an IEC HT centrifuge capable of achieving a relative centrifugal force (RCF) of 34,000 g's.

Several suspensions containing 0.5 g of powder per 10 ml of solvent were first settled for about one minute at a RCF of 17,000 g to eliminate the large agglomerates. A pellet was then cast from the supernatant at an RCF of 34,000 g. The second supernatant was then poured off.

Unfortunately, all specimens cracked to some extent during drying even though they were dried very slowly.

One pellet cast from mixed silicon and silicon nitride powders in a water suspension was sufficiently large that a density measurement could be made. It was 30% of theoretical density. TEM examination showed the particles did not achieve ordered packing and remnants of the agglomerate strings in the compact were still evident. These results corroborate the light scattering and laser Doppler analyses which indicated agglomerates persisted. More complete dispersion is required to achieve high densities.

C. Si Sintering

This research program has considered densification processes in Si powders in conjunction with the work on reaction bonding. Typically, the center-to-center distances between Si particles do not change during the nitriding reaction, so the final density is solely dependent on the green density of the starting silicon compact and the degree of reaction. Theoretically dense reaction-bonded silicon nitride cannot be obtained unless the initial compact density is approximately 1.91 g/cm^3 (82% theoretical density). This assumes that there is no sintering after the nitridation process.

One of the drawbacks of using ultrafine silicon powder, such as that produced by the laser synthesis process, is the difficulty in forming a high density green compact by conventional techniques. This results in a low nitrided density even if the piece nitrides to completion. For instance, the typically achieved Si green density of 1.04 g/cm^3 (45% theoretical) results in a fully nitrided piece having a density of 1.73 g/cm^3, which is only 55% of theoretical. This high porosity level is expected to cause the parts to have unacceptably low strengths. To overcome this problem, we developed techniques for densifying the fine silicon compact prior to nitriding.

Greskovich and Rosolowski[24] first reported that silicon powder compacts will sinter to near theoretical density (2.33 g/cm^3) at temperatures close

104

to the melting point of silicon if the silicon powder is sufficiently fine (less than approximately 0.25 μm). They reported 1%, 2.5%, 8%, and 23% linear shrinkage for powders having specific surface areas of 1.9, 11, 14.6, and 55 m^2/g, respectively, for 1 hour cycles at 1350°C in an argon atmosphere. Based on these results, it was concluded that the green silicon compacts could be pre-densified by sintering in Ar to a specific desired density level before they were nitrided. This procedure should allow production of high density Si compacts (70-80% theoretical) which can then be nitrided to completion, the result being a high purity reaction bonded Si_3N_4 with a density of 86 to 98% of theoretical.

1. Experimental

Sintering experiments were conducted with 1/2 inch diameter pellets (nominally 0.1 inches thick). The pellets were formed by pressing the powder (~ 0.2 grams) in a single action steel die within the glove box using a die pressure of 1000 psi. Typically, the die was filled, the powder pressed, broken up and repressed. This was necessary to achieve the desired pellet size. It will be shown in Sections IVC and IVD that this proceedure was not desirable in terms of pellet uniformity. These cold pressed pellets were then placed into double, evacuated, rubber bags and taken outside the glove box for isostatic pressing at a pressure of 40,000 psi. Following isostatic pressing the pellets were returned to the glove box, removed from the rubber bags, characterized and stored until heat treated.

The following procedures were employed for sintering. Samples were heated (heating rate ~ 900°C/hr.) to a predetermined temperature between 960 and 1100°C in vacuum (P < 20 mtorr). Upon reaching this temperature, Ar gas was introduced and the remainder of the sintering cycle was carried out at 1 atmosphere of Ar total pressure. Sintering temperatures ranged from 1100 to 1350°C and times from 10 to 60 minutes. Shorter sintering times were impractical because of the time needed to reach and stabilize the final temperature. Three individual furnace systems were used for these sintering experiments. The final Mo wound furnace permitted samples to be loaded into

a sealed muffle tube within the glove box thereby avoiding any exposure to air. This furnace had improved hot zone characteristics and permitted maximum anticipated nitriding temperatures to be maintained without effecting furnace life adversly. Alumina furnace muffles and boats (99.8%) were used in all cases.

Samples were characterized before and after firing. Dimensions and weights were used to determine densities and to assess both volitization and oxidation. Specific surface areas were monitored by BET. Microstructural analyses were done by SEM and optical microscopy.

Nineteen individual powder lots were studied. Fifteen (01S, 027S, 033S, and 622S-634S) were pure silicon and four (802SB, 803SB, 804SB and 806SB) were boron doped. Individual powder characteristics are summarized in Appendix II. The results of representative sintering experiments are summarized in Table 18.

2. Results

The results show that some of the laser synthesized Si powders densify as anticipated based on the Greskovich and Rosolowski[24] results. They also illustrate that the sintering behavior is highly sensitive to the individual powder lot. Within a specific lot, the pellet characteristics followed expected time and temperature effects.

The sintering results are generallized on the DeHoff[50] plot in Figure 45. DeHoff presented evidence that the specific surface area will decrease linearly with increasing pellet density from the initial specific surface area and density of the green pellet to zero specific surface area at 100% density if powders sinter exclusively by mechanisms which cause densification. If only coarsening mechanisms operate, the specific surface area will decrease continuously while the pellet density remains constant, equal to that of the unfired, green pellet. When coarsening mechanisms operate competitively with densification mechanisms, the specific surface area and density will follow a path between these two limiting cases. Qualitatively, the relative rates of the two types of processes are

106
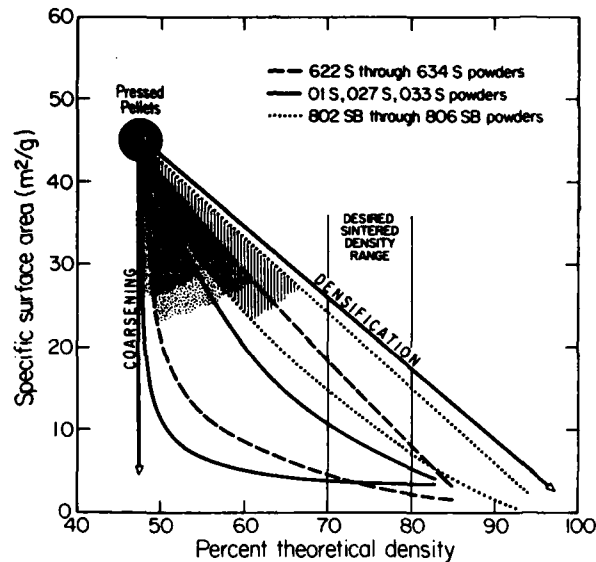
Figure 45. DeHoff plot of sintering characteristics observed for various Si powders.

indicated by the proximity of a pellet's behavioral history to one of the limits.

From the DeHoff plot, Figure 45, it is evident that there was substantial variability among the undoped powders with respect to the relative kinetics of the coarsening and densification processes. In some cases (01S and the 600 series) powders coarsened without appreciable densification while in others (802SB and 804SB) the powders proceeded along a path of almost pure densification.

Undoped powder lot 027S, that was coincidently the first studied, exhibited a behavior dominated by densification processes and rate kinetics which were in reasonable agreement with Greskovich and Rosolowski. Based on these initial observations, it was concluded that undoped powders could be densified to any predetermined density level and the value of the specific surface area at that density could be manipulated by changing the sintering temperature. This conclusion proved premature. Subsequent experiments with

TABLE 18

Si Sintering Conditions and Results[*]

Sample	Temp. (°C)	Time (min)	Final Density (g/cm^3)	Surface Area (m^2/g)
027S-4	1350	60	2.25 (96%)	**
027S-2	1350	0	1.80 (77%)	5.92
027S-1	1250	0	1.31 (56%)	25.4
027S-3	1250	10	1.43 (61%)	17.5
027S-5	1250	10	1.44 (63%)	**
027S-9	1250	20	1.48 (64%)	14.6
01S-13	1250	10	1.19 (51%)	**
01S-6	1300	10	1.14 (49%)	**
01S-11	1350	10	1.21 (52%)	**
01S-7	1350	10	1.28 (55%)	**
01S-14	1350	60	1.28 (55%)	**
033S-11	1250	10	1.17 (50%)	**
033S-13	1200	60	1.24 (53%)	**
033S-15	1300	10	1.26 (54%)	**
033S-14	1250	60	1.33 (57%)	**
033S-7	1300	60	1.47 (63%)	**
033S-1	1350	10	1.56 (67%)	**
033S-9	1325	60	1.58 (68%)	**
033S-5	1375	60	1.89 (81%)	**

[*] Initial densities were between 1.0 and 1.14 g/cm^3 (43 and 49% theoretical).

** Not measured

108

other undoped powders gave progressively less densification. Later lots (600 series) coarsened without any appreciable densification.

Attempting to duplicate the characteristics of powder lot 027S, and to determine why other powders were not densifying, undoped Si powders were characterized extensively. The chemical analysis in Table 2 resulted from this exercise. Small differences in grain structure within the polycrystalline Si powders were correlated with sintering characteristics. Also, various process variables: e.g., heating rate, exposure to air, non-vacuum heating, sintering time, sintering temperature etc., were manipulated empirically to find conditions which would cause densification. No consistant explanation was ever found for the difference in sintering behavior between 027S and other pure Si powders. Many of the differences suggested by chemical analyses proved spurious. Frequently, the impurity levels introduced during analyses were substantially higher than introduced during synthesis, storage and packaging. Many repeated analyses were required to resolve these issues. Reluctantly, we abandoned our investigation of factors which effect the sintering behavior of undoped Si in favor of intentionally adding boron as a sintering aid[51] to enhance sintering and make the sintering behavior more reproducible.

Boron was introduced during synthesis by mixing diborane (B_2H_6) with the other reactant and carrier gases. For these experiments, the diborane content was set corresponding to 0.4 wt. % boron in the gas phase. Chemical analyses of resulting powders indicated 0.47 wt. % boron showing that all of the boron from the diborane was incorporated into the powder.

As anticipated, the addition of boron to the Si powders caused their sintering to be dominated by densification processes. All of the boron doped powders closely followed the densification line on the DeHoff plot. This is particularly important for the subsequent nitriding step, because specific surface area is maximized at all density levels. The results also indicated that, in contrast to the undoped powders, the sintering characteristics of the boron doped Si powders were reproducible for different powder batches and for different sintering runs. This result permits specific density levels to be attained in combined sintering-nitriding heat treatments. Sintering characteristics were not effected by

109

exposing boron doped Si pellets to air prior to a sintering cycle which included vacuum heating to 960-1100°C. If the air exposure proves to have no adverse effect on the reaction kinetics or the properties of nitrided pieces, it may be possible to relax the stringent handling procedures currently employed.

The temperature effect on densification kinetics of the laser synthesized Si powders is summarized in Figure 46. All powders were boron doped and had initial surface areas (BET) of 46-48 m^2/g. Samples were held at the sintering temperature for 20 minutes. The slope of the curve corresponds to an activation energy of 2.074 eV. It is evident though that these powders sinter much more rapidly than powders studied by Greskovich and Rosolowski.[24,51] The densities achieved with 1250°C, 20 minute cycles for the laser synthesized powders were comparable to levels they achieved with 1360°C, 60 minute cycles using smaller diameter powders.

D. Si Nitriding

1. Objective

The three main factors which bring about high strength in reaction bonded silicon nitride (RBSN) are a product that is 100% silicon nitride, a high fractional density, and a controlled microstructure, i.e. grain, flaw, and void sizes, with a controlled phase mixture. The size of flaws in a ceramic body are usually related to the particle size of constituent powders, provided other classes of defects such as laminations, dirt and exceptionally large grains, as result from discontinuous grain growth, have been eliminated. Also, to retain strength at high temperatures, the amount of glassy grain boundary phase must be minimized, requiring high purity starting materials. In addition, higher reaction rates are expected for these smaller laser synthesized powders than is exhibited by conventional silicon powders, thus allowing nitriding to completion at lower temperatures and in shorter times. For these reasons, the silicon powders produced by the laser driven reactions would seem to be the ideal starting powders for

110
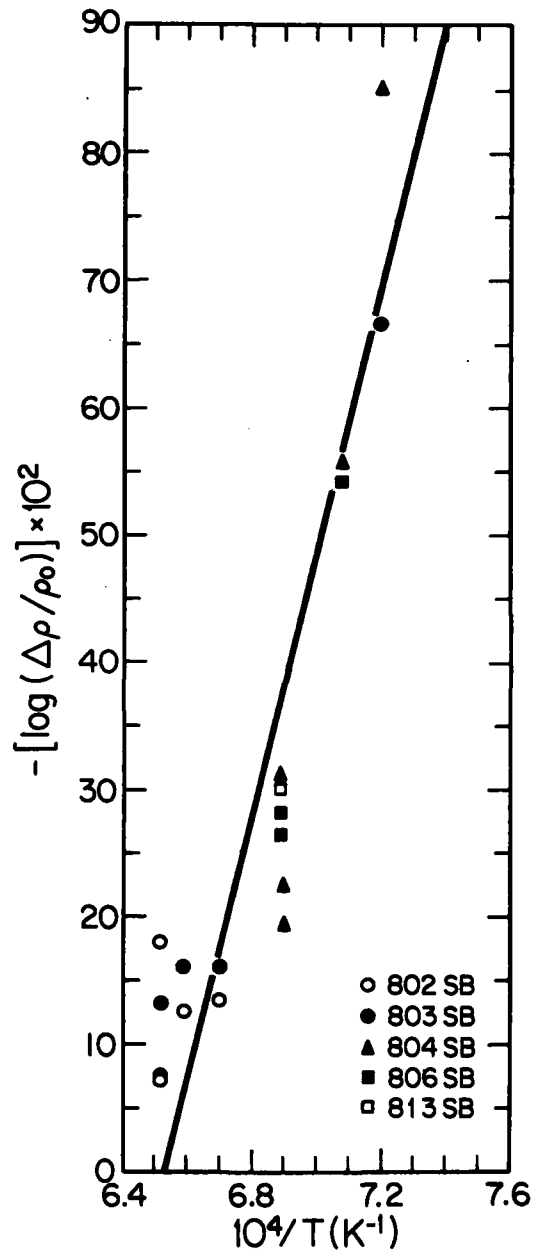
Figure 46. The effect of temperature on the sintered densities for various
Si powders.

producing high strength silicon nitride because of their high purity, extremely fine particle size and shape.

There are two key issues that must be addressed and dealt with successfully prior to optimizing process variables. The first, controllably sintering the laser synthesized Si to the desired densities, has been dealt with successfully. The second concerns completely reacting the green Si compacts with and without boron for varying post sintering densities. The overal goal is to fully react the high density Si compacts and maintain a high degree of control over the resultant microstructure so that the final nitrided structure is closely related to the sintered microstructure in terms of grain size, pore size, density, and general microstructural homogeniety.

Experiments were undertaken with the laser synthesized Si powders to determine whether the anticipated microstructural and reaction kinetics advantages would in fact be realized. Principally, they used conventional processing techniques and thus provided a direct comparison to existing materials. Although the literature contains many studies on nitriding kinetics, there have been almost as many rate laws postulated as there have been experimenters.[51-56] This poor state of understanding exists both because the reactions are inherently complex and they appear to be dominated by impurity effects. Thus, the use of these high purity, uniform Si powders could serve as an important basis for improved mechanistic studies. Also, new processing sequences are possible. With the unusually fine Si_3N_4 grain size that should be achievable with these Si powders, it may be possible to densify the nitrided pieces by a post nitriding sintering cycle. These additional topics were deferred in favor of the more limited objectives.

2. Theoretical

The nitriding processes are governed by both mechanistic issues which are typified by atomic or particulate scales as well as macroscopic issues characterized by the dimensions of the nitrided piece. The process needs to be controlled at all levels simultaneously.

112

There are several mechanisms of forming each of the α and β polymorphs of Si_3N_4 as evidenced by the varied morphologies of silicon nitride produced.[54] The main mechanisms would seem to be a vapor phase reaction where $Si(g)$ or $SiO(g)$ reacts with N_2 to form the nitride which is deposited,[54] and a condensed phase mechanism in which silicon (solid or liquid) reacts with adsorbed nitrogen to form the nitride in situ.[54,57,58] It is generally agreed the vapor phase mechanisms form α-silicon nitride, and they are enhanced by lower temperatures, minor oxygen impurity levels, slow heating rates, and low gas flow rates, while the condensed phase mechanism form β-silicon nitride and they are enhanced by higher temperatures, Fe impurities, fast heating rates and high gas flow rates.[53-56] Various additives can be employed to "enhance" specific mechanisms, but they usually have adverse effects on process control microstructure and/or properties.[59]

Since the system of $3Si+2N_2 \rightarrow Si_3N_4$ is so similar to the classical systems involving the oxidation of a metal, many of the models of the reaction postulated in the literature have been based on the oxidation models. These models include the familiar linear and parabolic rate laws[52,57,60,61] and those derived by Evans[62] for the oxidation of metals where transport is via microcracks. There seems to be experimental evidence for each model. This could be due to the many experimental techniques used: no two groups of researchers have used exactly the same equipment or procedures, and none achieved the same results.

Macroscopically another type of transport must be considered in the nitriding reaction: the bulk transport of nitrogen gas into the powder compact. Since there is an approximate 22% volume increase associated with the reaction, porosity in the compact will be totally eliminated as the reaction proceeds if the initial silicon density is greater than about 80% of theoretical, thus preventing the nitrogen access to the remaining unreacted Si. Because of this, complete nitriding will be retarded as the pre-nitriding fractional density is raised. It is clear that, for achieving high fractional densities one desires a sintered Si compact with the maximum specific surface area possible for any chosen density.

The formation of silicon nitride is a highly exothermic reaction which must be considered on the macroscale of the piece. If this is not taken into account during the reaction bonding process, problems can be encountered which range from catastrophic melting of the powder compact to localized melting of the silicon grains causing strength limiting voids. In general practice, these problems are avoided by slow, controlled heating of the compact to allow formation of a nitride layer around each silicon grain, after which the heating rate and the nitriding temperature can be increased. Elimination of all nitriding aids such as Fe also reduces the chances of melt related microstructural defects. Careful consideration of the transfer of heat in the compact becomes of paramount importance, when working with very reactive powders. Since the heat produced is porportional to the amount of nitride produced, the rate of reaction as well as the surface-area to mass ratio of the compact needs to be considered in determining whether uncontrolled heating will occur.

3. Experimental Approach

It is apparent that the development of an understanding of the nitriding process involves an almost open ended level of complexity. Consequently, we have limited our nitriding research to describing nitriding kinetics under previously reported processing conditions, consideration of the macroscopic transport issues and thorough characterization of resulting pieces. The intent of the experiments was to demonstrate that the advantages anticipated with using these Si powders could be realized.

Nitriding experiments have been performed using Si powders both with and without boron doping, and have utilized pellets both with and without sintering treatments in argon. The following undoped Si powders have been used, (Appendix II): 01S, 027S, 103S, 216S, 627S, 628S, 630S, 631S, 632S, 801S, 808S, and 809S. Powders doped with boron used for nitriding were (Appendix II): 802SB-806SB, 813SB, LSB1, and LSB3. The powder surface areas ranged from 34.4 m^2/g to 110 m^2/g but were all near 47 m^2/g for the latest experiments using boron doped Si.

114

Sample fabrication was carried out as described in Section IVCl. The densities of the as pressed pellets were all in the range of 1.05 to 1.17 g/cm^3 (45 to 50%) theoretical). Pellets that were sintered and then nitrided were of two types. One set was sintered in argon, removed from the furnace for characterization and then subsequently nitrided. The second set of pellets was sintered in argon and then nitrided without removal from the furnace. In this case, the furnace was cooled to < 1000°C after sintering, and then evacuated and backfilled twice with the nitriding atmosphere to prevent further sintering and to insure maximum gas exchange.

Nitriding experiments have been preformed to address the key issues cited above. Preliminary experiments determined if the laser synthesized powders would indeed nitride and whether the reaction rates differed substantially from conventional powders. These experiments were carried out in an Al_2O_3 muffle tube furnace in a static N_2-5% H_2 atmosphere at 2 psig. Prior to the establishment of nitriding conditions, the samples were heated (at 250°C per hour) to 1100°C under vacuum since they were exposed to air during loading into the furnace.

A second set of experiments comprised of a kinetic study.[63] For this group, thermogravinometric measurements were preformed in the glove box using a tungsten induction furnace. Since the glove box was used, the atmosphere was static nitrogen rather than the N_2-5% H_2 mixture used in the first set of experiments. The temperature was increased rapidly to 1020°C, and held for 5 minutes to allow the system to equilibrate, then the temperature was increased rapidly to the nitriding temperature. Only one powder lot (103S) was used in this set of experiments which was intended to determine the effect of temperature on the reaction rate.

A third set of experiments was performed to provide data for the kinetics and microstructural studies, and also to produce the first group of high density samples for mechanical testing. In this case, 99.8% Al_2O_3 muffles and boats were used (a seperate set for Si and Si with boron) in a Mo wound furnace. Heating rates were ~ 900°C/hour and the nitriding gases were static N_2 or N_2-10% H_2 at +8"H_2O pressure. Samples were either loaded in air or loaded into the muffle inside the glove box and then transferred

to the furnace without air exposure. All samples were heated at 960 to 1100°C under vacuum (< 20 mtorr) prior to sintering and/or nitriding.

Nitrided samples were characterized in the following fashion: sintered and nitrided densities were determined and percent reaction was measured by both weight gain and X-ray diffraction. The nitrided structure was evaluated by BET measurements of the surface area, and X-ray diffraction to measure the α and β contents. Optical microscopy was used to examine the pore structure, regions of unreacted Si, and any large scale microstructural inhomogeneities that may have existed. Scanning electron microscopy was used to evaluate the microstructures of fracture surfaces.

4. Results

The first set of experiments consisted of preliminary nitriding runs to determine if the laser powders would indeed nitride and whether the reaction rates for these powders differed from those of conventional powders. Four lots of laser powder were used in these experiments, 215S, 216S, 808S, and 809S (see Appendix II for the powder characteristics).

Although the surface areas were different, the powders nitrided similarly (Table 19). The major conclusion derived from the first set of experiments is that these powders will nitride and they are much more reactive than conventional silicon powders. Several other conclusions can be drawn from these results:

1. These Si powders do not react with nitrogen appreciably at 1200°C in one hour (216S-A and 216S-E), but at 1275 to 1300°C they will react to 60 to 80% in one hour (216S-E, 216S-C, 627S-1, 808S4, 808S5, 631S1, 631S3), and at 1400°C they will react to ~ 95% in one hour (808S-3, 809S-3).

2. The majority of the nitride formation is completed in less than one hour at temperatures above 1300°C, indicating significantly faster kinetics than for conventional Si powders.[52,54,57]

3. In these muffle systems, higher temperatures and longer times promote more complete reaction as expected.

Table 19

Nitriding Histories and Results from Undoped Pellets

Sample	Green Density (g/cm³)	Heat Treatment	% Nitrided	Nitrided Density (g/cm³)	Nitrided BET Surface Area (m²/g)	Nitrided Equivalent Spherical Diameter (Å)	X-ray Phase Composition Si/α/β (wt %)	Crystallite Size, X-ray Line Broadening Si/α/β (Å)
215-S-B*	-	1082°C-16 hrs 1227°C-45 hrs 1330°C-24 hrs	97	-	18	1415	3/81/17	-
216-S-D	1.12	-	-	-	28.5	903	100/-/-	100/-/-
216-S-A*	1.09	1200°C-1 hr	0	1.08	32.5	792	100/-/-	123/-/-
216-S-E*	0.95	1316°C-1 hr	74	1.39	8.3	2431	26/60/15	443/271/273
216-S-C*	1.09	1316°C-4 hrs	79	1.67	7.7	2583	21/63/16	300/260/460
216-S-J*	1.03	1316°C-4 hrs 1625°C-0.5 hr	100	1.68	9.0	2083	-/80/20	-/300/490
808S-4†	1.12	1275°C-1 hr	84	1.75	9.84	1917	16/67/18	**
808S-5†	1.10	1275°C-1 hr	83	1.69	9.49	1988	18/60/21	**
808S-8†	1.04	1300°C-1 hr	78	1.61	**	-	**	**
809S-8†	1.07	1300°C-1 hr	81	1.65	**	-	**	**
808S-7†	1.04	1350°C-1 hr	88	1.71	9.61	1957	**	**
809S-7†	1.03	1350°C-1 hr	83	1.67	10.61	1778	**	**
808S-3†	1.05	1400°C-1 hr	95	1.78	9.9	1906	2/69/29	**
809S-3†	1.14	1400°C-1 hr	97	1.86	12.3	1534	1/70/29	**

† Nitrogen
* Nitrogen – 5% H_2
**Not Measured

117

4. Complete nitriding is possible by heating the mostly nitrided pellet to 1625°C, well above the melting point of silicon, for short times, with no appreciable changes in the microstructure, surface area, phase composition or crystallite size. (216S-J & 216S-C)

5. Near complete nitriding can be achieved by a low temperature, long time heating cycle with about the same amount of surface area reduction as in the rapid high temperature cycle, but with a more uniform microstructure. (216S-B & 216S-J).

Microstructural examination (SEM) has been performed on 215S-B, 216S-A, and 216S-E. After heating a Si compact to 1200°C for 1 hour (216S-A), there was no reaction and no discernable change in microstructure from that of the green Si compact. Sample 215S-B, which reacted to 97%, had much the same microstructural features as the starting Si compact, i.e. small, uniform, and spherical grains. In contrast, a large microstructural change was observed for 216S-E (1 hr at 1316°C) which reacted to 74%. This sample consisted of high density regions 3-5 μm in size, interspersed with low density regions 1-2 μm in size. This corraborated other[64] work which indicated that slower heating rates and longer times at lower temperatures yield superior microstructures.

Despite these seemingly well behaved results, other early experiments indicated that the nitriding kinetics may be powder-lot sensitive. As an example: pellets 631S-1 and 632S-1 were nitrided under the same conditions as 631S-3 and 632S-3. The percent reacted was 61.8 and 28.6% for 631S-1 and 632S-1, while for 631S-3 and 632S-3 it was 63.6 and 26.2% respectively. Due to certain design deficiencies in the original furnace system, it is possible that this apparent powder-lot sensitivity resulted from unequal thermal histories experienced by the pellets. Rather than redesign and modify that piece of equipment, a second set of nitriding experiments involving the kinetics and a third set involving mechanical testing samples were initiated. Each of these sets of experiments used newly constructed nitriding systems.

The kinetics studies were conducted in the powder handling N_2 atmosphere of the glove box with an induction heated thermogravinometric

unit. This set of experiments produced the four curves shown in Figure 47 for the fractional weight gain vs. time at 1275°, 1300°, 1325°, 1400°C for powder 103S. At the three lowest temperatures the curves exhibited two distinct regions; a linear region, followed by a second region best described by the asymptotic rate law derived by Evans[62]. The initial reaction rate in the asymptotic region is about 10 times that of the linear region. In the second region the slope goes to zero indicating that no further nitriding takes place. The highest temperature studied did not exhibit the initial linear region.

Comparison of these results with others in the literature brings out two important points:

1) The laser synthesized silicon powders are much more reactive than conventional silicon powders,[52,56] nitriding to the same extent in much shorter times. This agrees with the conclusion from the first set of experiments.
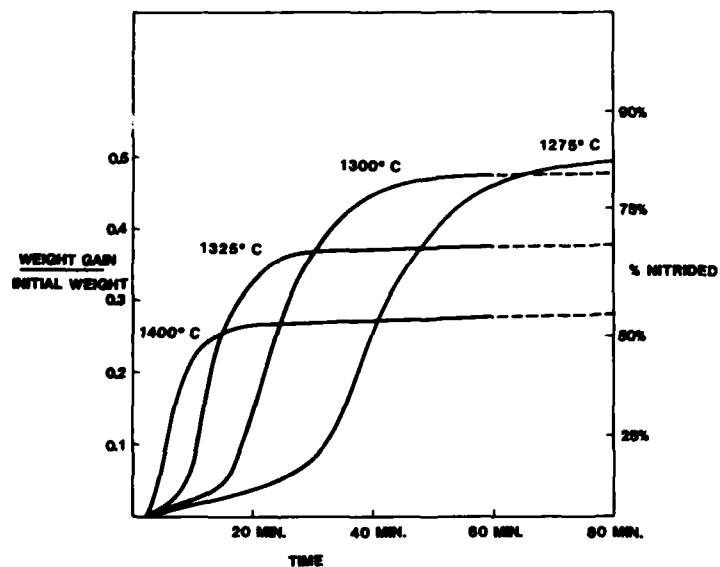
Figure 47. Fractional weight gain as a function of nitriding time at various tempratures. The % nitrided scale was calculated from the weight gain.

2) In contrast to conventional silicon powders,[52,57] as the nitriding temperature is increased the total extent of reaction decreases. At short times this anomaly is masked by the linear region where the nitriding rate increases with increasing temperature.

The anomalous behavior of decreased extent of reaction with increased temperature has not yet been explained fully. A parallel series of experiments were conducted in the newer Mo wound Al_2O_3 muffle furnace to determine if this unusual result was due to inherent powder characteristics, or the unique environment of the glove box. Table 19 also shows the percent reaction for powder lots 808S and 809S nitrided for one hour in N_2 at 1275, 1300, 1350, and 1400°C in the Al_2O_3 muffle system. At 1275°C, the extent of reaction is slightly higher than that measured on lot 103S using TGA. In contrast to the TGA results, in the Al_2O_3 muffle system, the extent of reaction clearly increased as the nitriding temperature increased. These results indicate that while there may be some powder lot variation on the nitridation kinetics, the actual nitriding environment is likely to be the controlling factor.

The information required to complete the heat transfer analysis can be obtained from the reaction rate curves in Figure 47. The calculations that were made determine whether heat flow could have been responsible for the anamolous results observed in the W furnace and for the apparent operation of two distinct reaction rate domains. Each curve can be approximated by two linear regions, and the molar rate of formation of the nitride, dn/dt, can be calculated for each. This value, combined with the heat of formation, ΔH_f, at that particular temperature, can be used to find the rate of heat generation in the compact using

$$\dot{Q} = \left| \Delta H_f \right| dn/dt \tag{40}$$

where $\dot{Q}$ is constant for each linear region. With radial heat flow, the difference in temperature between the center and the surface of a cylindrical shape is given by:[65]

$$\Delta T = \frac{SR^2}{4k} \tag{41}$$

where S is the rate of heat production per unit volume, R is the radius of the compact, and k is the effective thermal conductivity.

Heat transfer should not be a problem for any of the temperatures in the first linear region. The largest calculated temperature increase is 2.7°C for the 1325°C reaction rate. In the second linear region at the highest temperature, 1400°C, the calculations indicate that the temperature at the center of the pellet is over 21°C higher than the surface, thus bringing the interior to almost 12°C above the melting point of silicon. Catastrophic melting of the pellet did not occur. The absence of melting could be explained because these calculations were based on the geometry of an infinite cylinder and thus the heat loss from the ends was ignored. Taken in total, the results of these calculations indicate that for small samples, heat transfer should not be a problem in terms of catastrophic melting, although localized melting of individual grains of silicon may occur. For larger samples, this analysis can guide the selection of the best nitriding temperature and rate to avoid overheating. The heat transfer calculations also imply that the change of the reaction rate from a linear to an asymptotic behavior cannot be attributed to runaway heating of the pellets.

An additional concern was how the addition of boron to the Si would effect the nitriding kinetics. Table 20 compares the extent of reaction of powders nitrided in Al_2O_3 muffles with and without boron. Without boron, powders react to between 61 to 81% in one hour at 1300°C and 58 to 97% in one hour at 1395-1400°C. At 1300°C for one hour, pellets with boron react to only 5-7% and at 1395°C react to 41-44% after one hour. The addition of 0.4 wt. % boron (as an aid for Si sintering) has the effect of reducing the nitriding kinetics substantially. It is felt[66] that the addition of boron to Si aids in sintering by reducing the surface diffusion rate of Si, thereby allowing densification mechanisms to become active. If so, this might also reduce the rate of nitridation by decreasing the rate at which Si is made available for nitridation at the reaction sites (assuming surface diffusion is the active material transfer mechanism).

121

TABLE 20[*]

Si Nitriding Results for Undoped and B-doped Pellets

Sample	Temp. (°C)	% Reacted
631S-1	1300	61
6315-3	1300	63
808S-8	1300	78
809S-8	1300	81
631S-5	1395	68
632S-5	1400	58
808S-3	1400	95
809S-3	1400	97
LSB1-3	1300	5
LSB1-7	1300	8
LSB1-1	1395	41
LSB1-3	1395	43
LSB1-7	1395	41

[*] Nitriding time for all samples was 1 hour

Two additional sets of nitriding experiments were performed (in Al_2O_3 muffles) with sintered boron doped and undoped Si powders to determine if complete reaction could be achieved with high density Si compacts. These samples were used for mechanical testing.

For non boron doped Si, a comparison of the results shown in Table 19 and Table 21 indicates that both Ar-sintered and non-sintered samples exhibited the same general nitriding characteristics. Samples which were sintered and nitrided without removing from the furnace, nitrided less completely than samples which were pre-sintered, removed from the furnace and exposed to air, and then returned to the furnace for the nitriding cycle. This is observed by comparing samples 027S-5 and 027S-9 (Table 21) with samples 027S-8 and 027S-10, which were all subjected to similar sintering and nitriding cycles. This is likely to have resulted from achieving higher sintered densities when not exposed to air in the

TABLE 21

Si Nitriding Histories and Results for Undoped Presintered Pellets

Sample	Green Density (g/cm³)	Heat Treatment	% Nitrided	Nitrided Density (g/cm³)	Nitrided BET Surface Area (m²/g)	Nitrided Equivalent Spherical Diameter (Å)	X-ray Phase Composition Si/α/β (Wt %)	Crystallite Size, X-ray Line Broadening Si/α/β (Å)
Presintered in Ar (See Table 18)								
027S-5	1.44*	1250°C 48 hrs 1350°C 24 hrs	97	2.34	7.7	2450	3/66/31	-/370/580
027S-9	1.48*	1250°C 48 hrs 1350°C 24 hrs	97	2.52	7.5	2520	3/67/29	-/650/750
Sequential Sintering and Nitriding				Est. Si Density				
027S-8		See Below	63	1.87 1.60 (69%)	-	-	63/27/10	
027S-10		See Below	88	2.74 1.78 (77%)	-	-	12/60/28	

Sample	in Ar Temp.	Time	in N₂-5% H₂ Temp.	Time
027S-8	1250	10 min	1300	1 hr**
027S-10	1250	10 min	1250 1350	72 hr** 24 hr**

* Ar sintered density
** A vacuum was pulled for 1/2 hour between Ar and N₂ - 5% H₂ anneals.

123

sequential process. The estimate of shrinkage during sintering assumed that no dimensional changes took place during nitriding. Comparison of 027S-8 (a sequential sintering-nitriding run) and 216S-E (Table 19, a sample not pre-sintered in Ar) indicates that the degree of nitriding was more complete in the not pre-sintered, lower density sample. This result is related to the inability of nitrogen to enter a more dense specimen during a short nitriding cycle.

Microstructural examination of fracture surfaces by SEM of sample 027S-5 did not reveal either the high density regions or the very porous regions which had been seen in the fracture surfaces of Ar-sintered silicon specimens 027S-2 and 027S-3. This sample also nitrided to near completion, as shown in Table 21. Polished surfaces were examined by optical microscopy to determine whether unreacted silicon was present. No highly reflective areas typical of unreacted Si were seen, so it was concluded there were none greater than 1 μm in size. Approximately 1-5 μm diameter voids could be found throughout the surface. These voids, which probably result from agglomerates, must be reduced in size to improve the brittle fracture strength. The next smallest group of flaws were approximately 1000 Å to 2000 Å pores. The 1-5 μm voids are much smaller than voids observed in reaction bonded silicon nitride made from conventional powders.[64]

Table 22 shows the results of nitriding experiments on boron doped Si samples with densities ranging from 47% (not sintered) to 78.8% of theoretical. These results corroborate earlier observations, that the higher density green compacts are more difficult to nitride to completion than are the lower density (non-sintered) samples. The reduced kinetics in this case are due both to limited N_2 permeability and to the presence of boron. A pellet with a green density of 47% (806SB-8, not sintered) can be completely reacted by the thermal cycle indicated, namely 24 hours each at 1200, 1250, 1300, 1350 and 1400°C. As the green density increases, the extent of reaction decreases reaching 68.3% for a green density of 78.8% (803SB-12).

With low density pellets, the nitride product is largely α-Si_3N_4. For complete reaction (806SB-8) the α/β ratio is 7.3 which is desirably high

124

for reaction bonded Si_3N_4.[64] As the sintered density increases and the ultimate extent of reaction decreases, the α/β ratio decreases to a value of 0.8 for 803SB-12. This indicates that the kinetics of $\alpha-Si_3N_4$ formation are inhibited more by higher densities than the rate of $\beta-Si_3N_4$ formation.

By comparing nitride runs for pellets air and not air exposed (804SB-11 and 804SB-13), it is evident that air exposure does not have any significant effect on the percent reaction or the phase make up of the Si_3N_4 produced. This does not preclude air exposure being critically related to the high temperature mechanical properties of the Si_3N_4.

Pellets 813SB-5 and 813SB-6 were nitrided in $N_2-10\%H_2$, rather than N_2, to determine the influence of H_2 on the kinetics and phase ratio. Comparing these pellets with other equal density pellets (804SB-12 and 806SB-7) nitrided in N_2, indicates that H_2 had no significant effect on the kinetics or phase make up of the Si_3N_4. Other investigations[64,67,68] have found the addition of H_2 to the nitriding system has the effect of refining the microstructure and either changing[68] or not changing[67] the α/β ratio.

It appears that the reaction kinetics and the nitride product (percent reacted and α/β ratio) are fairly reporducible run to run (804SB-12, 806SB-7 and 803SB-13) and they do not appear to be powder-lot sensitive. There is frequently a discrepency between the extent of reaction as determined by X-ray diffraction and by weight gain with weight gain analysis usually indicating less reaction. Vaporization losses which occur during nitridation make that measure of reaction yield a lower value than X-ray diffraction analyses.

Microstructural examination of these Si_3N_4 materials was carried out using optical microscopy of polished sections and SEM of fracture surfaces. Optical microscopy has revealed generally two scales of inhomogeneities. There are very small pores, $\sim 1\mu m$, associated with the Si_3N_4 product, and much larger inhomogeneities, 10-50 μm, which are associated with the method of die pressing the Si powders.

After the initial die pressing, the pellet is broken up, more powder added, and then the powder mixture is repressed. This results in an

inhomogeneous green compact consisting of low and high density regions.
During sintering, the high density regions (or regions of high particle
coordination number) densify more rapidly than do the low density regions,
yielding structures typical of that in Figure 48. The severity of these
inhomogeneities increases with increasing sintered densities. In nitrided
samples such as 806SB-8, which was not sintered, there is only a slight
suggestion of the as-pressed microstructural inhomogeneities. At the other
extreme are samples such as 804SB-11 or 803SB-12 where the inhomogeneities
are so severe after sintering that the high denisty regions have reached
fractional densities ~ 80-90%. Because these regions are fairly large,
> 10 μm, their nitriding kinetics are much slower than the lower density
regions. The result is large regions of unreacted Si remaining in these
samples which may act as potential flaws.

Examination of these samples using SEM revealed the following: (1) the
structures generally appeared quite fine, typically with an ≈ 0.1 μm grain
size, (2) the structures of fully reacted samples appeared very uniform,
Figure 49, (3) the nitrided structures of the high sintered density samples
had two characteristic sizes, i.e. a fine scale ≈ 0.1 μm grain size, and a
larger feature 1-5 μm in size which had the appearance of a cleaved fracture
surface, Figure 50. This large, smooth, fracture surface could either be
attributed to fracture of high density Si regions or to fracture of
predominantly β-Si$_3$N$_4$ regions. This type of feature is similar in size and
morphology to the features seen on fracture surfaces of the high density
sintered silicon compact, Figure 51.

Several points are evident from these results. First, it is absolutely
essential that any inhomogeneities in the as-pressed powders be eliminated.
The practice of pressing pellets and breaking them up is clearly
inappropriate for further investigation. The second point relates to the
ability to nitride high density compacts to completion. Based on the
microstructures we have seen, the presence of these very high density
regions (80-90%) is the main reason we have been unable to nitride sintered
pellets (70% dense) to completion. We feel quite strongly that if the
imhomogeneities are removed and a uniform sintered density of 70-80% is

126
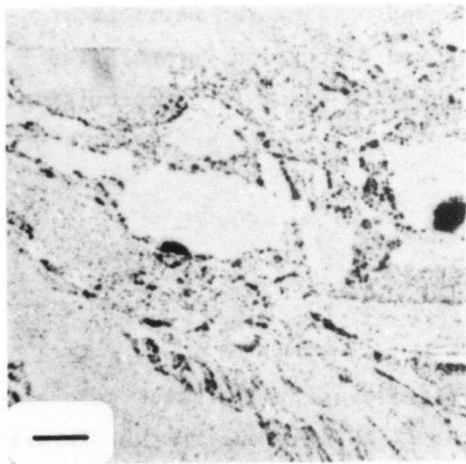
Figure 48. Optical micrograph showing non-uniform sintered microstructures resulting from compacting method used. (Bar = 10 μm)
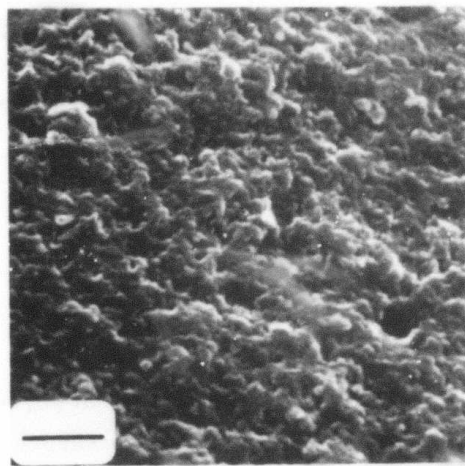
Figure 49. SEM micrograph showing fine, uniform structure of fully reacted Si_3N_4 sample. (Bar = 1 μm)
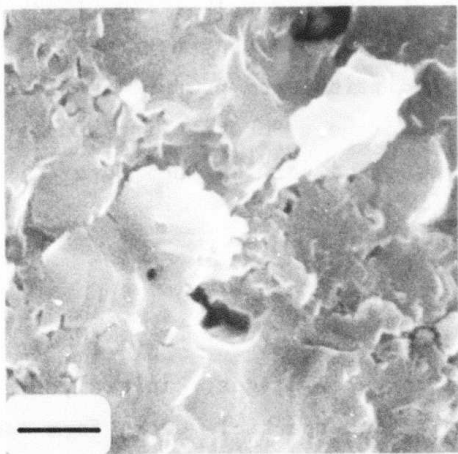
Figure 50. SEM micrograph of Si_3N_4 made from a high sintered density Si compact; note fine and coarse structures. (Bar = 1 μm)
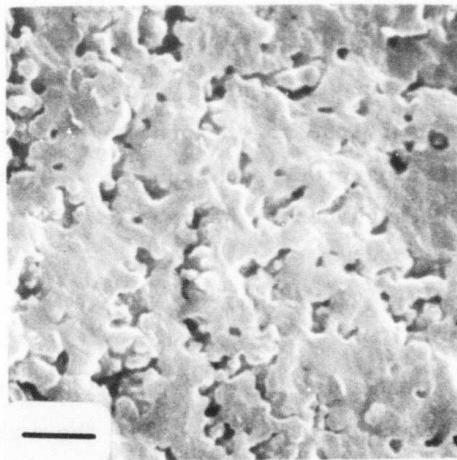
Figure 51. SEM micrograph of high density sintered Si compact. (Bar = 1 μm)

127

achieved, we should be able to fully react them to completion yielding 86-98% dense Si_3N_4 compacts with flaw sizes approaching the particle dimensions. The powder handling procedures and dispersion technologies leading to the ordered particulate arrays shown in Figure 1 are promising routes for achieving this result.

E. Silicon Nitride Sintering

1. Objective

To date, stoichiometric Si_3N_4 has not been densified without resorting to sintering aids, applied pressure or both.[69] This is due to the sintering being dominated by mechanisms which cause neck growth without reducing interparticle distances. The relative rates of the mass transport processes are particle size dependent and it has been proposed[24] that processes which cause densification may dominate the sintering process if the Si_3N_4 particles are made sufficiently small.

This program has investigated the feasibility of densifying the laser synthesized Si_3N_4 powders without additives or pressure. It is important to eliminate the additives used for sintering aids because they degrade high temperature mechanical properties, and it is difficult to produce intricate shapes by the more expensive hot pressing technique. Substituting simple sintering processes reduces manufacturing costs and permits much more complex shapes to be fabricated.

2. Background

Sintering is traditionally separated into three stages: initial, intermediate and final. In the initial stage, interparticle necks form and grow, in the intermediate stage, porosity changes from interlinked to discrete, and in the final stage, the remaining isolated pores are eliminated. Mass transport mechanisms which operate during sintering can be divided into those which cause densification (lattice and grain boundary diffusion and viscous flow) and those which cause only coarsening of the

structure (evaporation-condensation and surface diffusion). The identities
of the dominant transport mechanisms during initial stage sintering are
usually inferred from neck growth rates, surface area changes and shrinkage
rates under isothermal conditions. Sintering models for the latter two
stages concentrate on the effects of grain and pore size distributions as
well as surface area changes. The scale of microstructural features often
change during the latter stages of sintering[70] which can cause a change in
rate controlling mechanisms.

Pure silicon nitride is highly covalent (70%), and for a long time was
classified as unsinterable because the Si and N diffusivities are so low.
Silicon nitride is presently densified with the addition of oxide sintering
aids. These react with the Si_3N_4 and the silica on the surface of the Si_3N_4
particles to form a liquid phase during heat treatment.[71] Densification
takes place by rearrangement followed by a solution-reprecipitation
mechanism.[72] Typical sintering aids include $MgO(3-5\%)$, Y_2O_3 (4-15%) or
combinations such as BeO (1-2%) + MgO (3-4%).[69] Parts produced in this
manner have sintered densities in the range of 85-97% of theoretical.
Weight losses due to the dissociation of silicon nitride are typically 4-15%
which resulted in some research being done using high nitrogen pressures to
suppress decomposition.[73] The high temperature performace of the sintered
nitrides is limited by the presence of glassy secondary phases at the grain
boundaries which result in high creep values, and limit fracture strengths.

It has been shown[24] that there is no fundamental thermodynamic barrier
to the densification of Si_3N_4 and that the final microstructure is
determined by the operative mass transport mechanisms. It has been
proposed[24] that the ratio of diffusivity to particle size should be on the
order of 10^{-6} cm/sec for densification processes to dominate in covalently
bonded solids. Based on this criteria and a diffusivity of 5 x 10^{-12}
cm^2/sec (for nitrogen in Si_3N_4 grain boundaries at 1800°C)[71], densification
should be observed with particle sizes less than 500 Å (38 m^2/g surface
area). This maximum diameter is larger than is typically produced by the
laser synthesis process.

In addition to having a small particle size, the laser synthesized
powders are amorphous and can contain excess Si. The excess Si is known to

lower the crystallization temperature of amorphous Si_3N_4 relative to the 1490°C measured[74] for stochiometric Si_3N_4. It will also nitride during the sintering heat treatment and thus will contribute a microstructural characteristic which is distinct from that originating by a sintering process. Both the nitriding and the crystallization processes have moderately high driving forces associated with them which may contribute to the densification process. For instance, the amorphous to crystalline transformation has been reported to cause an increase in the shrinkage rate during hot pressing.[74,75] Similar results might be expected in sintering without resorting to applied pressure.

3. Experimental Procedures

Two sets of sintering experiments were undertaken. The sintering temperature was varied in one (A and B series) and was held constant in the other. The process conditions used to produce the powdes are given in Appendix I. The chemical characteristics of the resulting powders are given in Appendix II. Physical and crystallographic characteristics are given in Tables 23 and 24 along with pellet characteristics. Both powder lots are amorphous and have essentially the same specific surface area. The stoichiometry was manipulated to provide a basis of comparison. Although the oxygen content is significantly higher than other impurities, it is lower than found in commercially available powders and this O_2 level corresponds to slightly less than a monolayer per particle. Improved synthesis and handling procedures have permitted O_2 contents to be reduced by an order of magnitude.

Pellets were made by loading 150 mg of powder into a 0.5 inch diameter stainless steel die and cold pressing to 5000 psi with a hand operated press within the glove box. All of the type 405SN pellets and representative type 402SN pellets were isostatically pressed in evacuated double bags at a presesure of 45,000 psi. Although pressing occurred outside the glove box, no contamination was detected because the bags were loaded and sealed within the glove box.

TABLE 22

Si Nitriding Histories and Results for B-doped Pellets

Sample	Green Density (g/cm³)	(%Theo)	Sintering Temperature (°C)	Sintered Density (g/cm³)	(%Theo)	Thermal History	Nitrided (wt.%)	Nitrided Density (g/cm³)	(%Theo)	Nitrided Surface Area (m²/g)	Phase Content (wt.%) Si/α/β
804SB-12*	1.09	46.6	1141	1.37	58.6	A	92	2.19	68.7	8.91	3/77/19
806SB-7*	1.07	45.8	1141	1.38	59.0	A	97	2.27	71.3	#	2/77/20
803SB-12*	1.06	45.5	1215	1.84	78.8	A	68	2.56	80.6	#	21/35/43
803SB-13*	1.07	45.8	1115	1.30	55.7	A	93	2.15	67.6	#	1/73/20
804SB-11*	1.02	43.8	1171	1.63	69.8	A	83	2.44	76.9	#	1/50/50
806SB-8*	1.10	47.0	Not Sintered	-	-	A	100	1.53	48.0	#	1/87/12
804SB-13	1.10	47.0	1171	1.63	69.9	A	85	2.58	81.0	5.68	2/74/25
806SB-9	1.08	46.3	1171	1.67	71.5	A	80	2.51	79.0	5.10	3/72/25
806SB-10	1.10	47.2	1171	1.68	72.0	B	87	2.65	83.3	5.19	1/73/26
813SB-2	1.13	48.4	1171	1.69	72.6	B	83	2.62	82.4	6.80	1/68/31
813SB-5	1.10	47.4	1171	1.46	62.6	A	89	2.33	73.2	9.48	1/75/24
813SB-6	1.06	45.4	1171	1.47	62.9	A	95	2.41	75.7	9.71	0/79/21

Thermal History A: Sintered in Ar at indicated temperature for 20 minutes, evacuated at 960°C, exposed to nitriding gas, then held at 1200, 1250, 1300, 1350 and 1400°C for 24 hours each.

Thermal History B: Same cycle as A plus additional nitriding at 1450, 1500 and 1550°C for 12 hours each.

Nitrided Gas: N₂ for all runs except 813SB-5 and 813Sb-6 which used N₂+10% H₂.

* Air exposed

\# Not measured

131

After isostatic pressing, the pellets were heated in a tubular tungsten element, inductively coupled furnace within the glove box. Samples were totally enclosed within a capped tungsten crucible and supported on a Si_3N_4 substrate. Supports below the tungsten crucible were Al_2O_3. Temperatures were measured by optical pyrometry with appropriate corrections[76] and heat up times were less than minute for all temperatures.

Powders and pellets were characterized by several complimentary techniques to follow the consequences of the firing cycles. Physical dimensions were used to measure bulk density and shrinkage. BET analysis was used to measure specific surface area and monitor equivalent particle size. X-ray diffraction analysis was used to provide quantitative evaluations of α, β and amorphous phases and to measure grain sizes of crystalline phases. SEM and TEM analysis were used to give particle size, particle size distributions and descriptions of other microstructural features. TEM was also used to determine the locations of amorphous and crystalline particles. He pycnometry and Hg porosimetry were used to measure density and pore size distribution respectively.

4. Results and Discussions

The BET and X-ray results for the fired samples and starting powders are given in Tables 23 and 24. These results show two generalizations. First, a reduction in surface area occurs concurrently with an increase in the percent crystallized. As heat treatment progresses, the equivalent particle size (BET) increases from a dimension that is slightly smaller than the crystallite size to one which is substantially larger. Second, the crystallite size appears constant, invarient of the firing temperature, firing time, volume fraction crystallized or crystalline phase. The linear correlation between specific surface area and percent crystallinity is shown in Figure 52. Nearly stoichiometric powders and powders containing excess Si exhibit identical behavior.

SEM and bright field TEM , Figure 53, both show that heat treatment produces a progressively coarsening microstructure which is comprised of

TABLE 23

Characterizations by X-ray and BET Analyses of Si_3N_4 Samples
Fired 30 Minutes at Different Temperatures

Sample	Temp. (°C)	Wt. Gain Δw/w %	Si	Si$_3$N$_4$ α	Si$_3$N$_4$ β	Si$_3$N$_4$ amor.	m^2/g	Sperical Dia (Å)	α(301)	α(222)	β(320)
402SN-1	1650	11	0	58	42	0	15	1200	334	292	310
402SN-2	1500	11	0	60	40	0	17	1070	310	280	282
402SN-3	1380	9.6	0	54	38	8	18	1010	311	283	290
402SN-10	1340	0	0	14	0	86	71	256	333	310	-
402SN-5	1300	-	0	4	0	96	76	240	-	-	-
402SN	-	-	0	0	0	100	92	200	-	-	-
405SN-1	1525	0	0	76	24	0	22	870	310	282	300
405SN-2	1380	0	0	64	21	15	30	638	320	300	300
405SN-3	1340	0	0	46	23	31	34	568	340	320	310
405SN-4	1300	0	0	17	10	73	62	308	310	320	-
405SN	-	-	0	0	0	100	98	195	-	-	-

TABLE 24

Characterizations by X-ray and BET Analysis of Si_3N_4 Samples
Fired at 1340°C for Different Times

Sample	Time (min)	Wt. Gain Δw/w %	Si	Si$_3$N$_4$ α	Si$_3$N$_4$ β	Si$_3$N$_4$ amor.	m^2/g	Spherical Dia. (Å)	α(301)	α(222)	β(320)
402SN-10	30	0	0	14	0	86	71	256	330	310	-
402SN-11	60	0	0	21	0	79	63	289	335	315	-
402SN-12	90	0	0	33	0	67	57	320	335	310	-
402SN-13	120	0	0	42	0	58	39	467	310	310	-
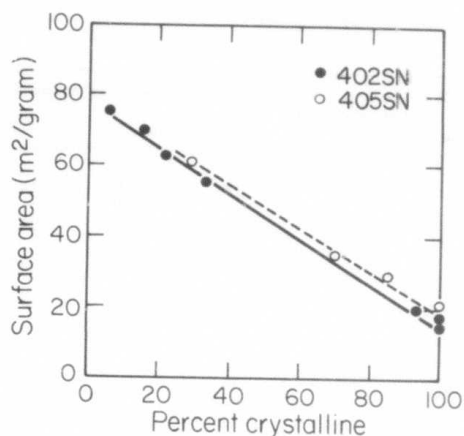
Figure 52. Specific surface area as a function of crystallinity for Si_3N_4 powders subjected to varying time-temperature histories.
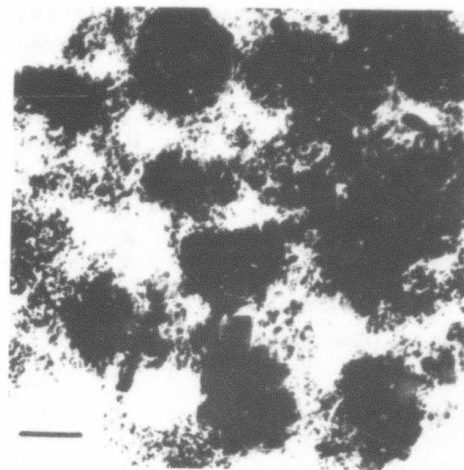
Figure 53. TEM bright field micrograph of partially crystallized Si_3N_4 sample (405SN-3) fired 30 minutes at 1340°C. (Bar = 1000 Å)

particles having two characteristic dimensions. The smaller particles have the same size as unfired amorphous particles and the larger ones are many times bigger. Also, with progressive firing, the pore structure enlarged following the formaiton of the large particles. Dark field TEM showed that all remaining small aprticles were amorphous and that all large particles were completely crystalline having a randomly oriented, mixed α and β crystals with a grain size approximately equal to the diameter of the small amorphous particles. With complete crystallization, all of the small particles disappear from the microstructure becoming incorporated into the larger clusters. Negligible macroscopic shrinkage was observed. These observations agree with the Hg porosimetry measurements. As-pressed 405SN pellets exhibit a single pore size averaging approximately 200 Å. With intermediate firing (405SN-3), both 200 Å and 1500 Å pores were present. Full firing (405SN-1) left only the larger pores.

The microstructural results also agree with the BET measurements. The equivalent spherical diameters of the unfired powders equal the directly observed diameters indicating that the particles have smooth surfaces and

134

contain no porosity which is accessble to the gas. The specific surface
areas of the fully fired samples also agree closely with those calculated
for the 1400 x 700 Å ellipsoidal shaped large particles; again indicating
that they contained no open porosity. Intermediate firings showed specific
surface areas corresponding to a mixture of the two particle sizes.

He pycnometric densities were measured to determine the densities of
the large particles that result from firing. Allowing for a high level of
experimental error due to a limited sample volume, these measurements,
Table 25, indicate that the clusters making up the large particles contain
some internal porosity (7-34%) which BET characterization showed was not
open to the surface.

TABLE 25

Pycnometric Densities of Unfired and Fired Si_3N_4 Pellets

Sample	Pellet Density		Pycnometric Density[*]		Error Bounds[**]			
					Low		High	
	g/cm^3	% Theoretical	g/cm^3	% Theoretical	g/cm^3	% Theoretical	g/cm^3	% Theoretical
405SN[†]	1.28	40	2.71	85	2.08	65	3.19	100
405SN-1[††]	1.28	40	2.48	78	2.12	66	2.98	93

[*] Porous Materials - Ithaca, N. Y.
[**] Systematic Error in Volume Measurement
[†] Pressed Powder in Green State - 100% Amorphous
[††] Fired Sample - 100% Crystalline

All of these characterizations indicate that, using these small
diameter, amorphous Si_3N_4 powders, a 40% dense, pellet made up of individual
constituent particles transforms with firing to a microstructure made up of
dense, polycrystalline clusters. Densification occurs on a local scale but
not macroscopically and the densification process evidently involves
crystallization. It has not yet been determined what caused the formation
of the large particle clusters. It is probable that they result from
agglomerates in the starting powders because green density had no effect on
cluster size. This result suggests that macroscopic densification would
occur in powder compacts having uniformly high coordination numbers between
particles as shown in Figure 1.

These observations indicate that localized densification into clusters is connected with the crystallization process, perhaps via the Hedvall[77] effect. Alternative explanations for the observed microstructural changes, such as amorphous particles first attaching and then sintering into crystalline clusters or sintering of agglomerates (before or after crystallization) were considered. These alternative explanations seem unlikely since both predict an increase in crystallite size and/or cluster size with either an increased firing time or temperature; neither of which were observed in this study.

Crystallization kinetics were modelled because the phase transformation is linked to the localized densification process. Several models show[11] that the time dependence of the volume fraction transformed for a heterogeneous transformation with interface controlled, thermally activated growth will follow an expression having the form:

$$\xi = 1 - \exp(-kt^n) \qquad (42)$$

where ξ is the volume fraction transformed at time t, k is a constant and n is determined by the type of nucleation and growth behavior. Nucleation can be either homogeneous or heterogeneous. Growth can be limited by impingement with other transforming regions, by bulk surfaces or by internal structure (e.g. pores). We had no direct evidence for the type of nucleation process; however, X-ray and TEM results showed that growth proceeded to an ultimate grain size which was slightly larger than the original particle size.

Turnbull[79] analyzed the case where crystal growth is limited by a physical dimension which is small compared to the growth-rate • growth-time product. For his experiment which followed the solidification of mercury droplets suspended in a methyl cyclopentane solution, the value of n = 1 and the value of k is equal to Iv where I is the homogeneous nucleation rate per unit volume and v is the root mean square volume of the droplets. An identical time dependence (n = 1) immerges if nucleation is heterogeneous, but k = IA where I is the nucleation rate per unit area and A is the area of the particles.

The results given in Table 24 were analyzed, as shown in Figure 54, to determine the time dependence for the transformation. The least square slope of this data corresponds to n = 0.93 which is in reasonable agreement with the Turnbull value of 1.0. The implied transformation process also agrees with microstructural observations. Growth was very likely inhibited by a physical barrier. Also, over the entire range of volume fraction crystallized, multiple crystallites were never observed within the volume of an initially amorphous particle. No stages of growth other than the final crystallite size, which was slightly larger than the amorphous particles, were observed. It appears that growth is quite rapid until terminated and that also transformation kinetics are nucleation rate controlled.

It was not possible to distinguish between homogeneous and heterogeneous nucleation processes from these results; however, rates for both can be calculated. At 1340°C, the nucleation rate is either $2.55 \times 10^{12}/cm^3sec$ or $8.45 \times 10^5/cm^2sec$ based on the dimensions of the amorphous particles and the fact that 1-3 particles transform into a single grain. This latter observation indication indicates that a transformation front propagates through a few necks between initially amorphous particles.
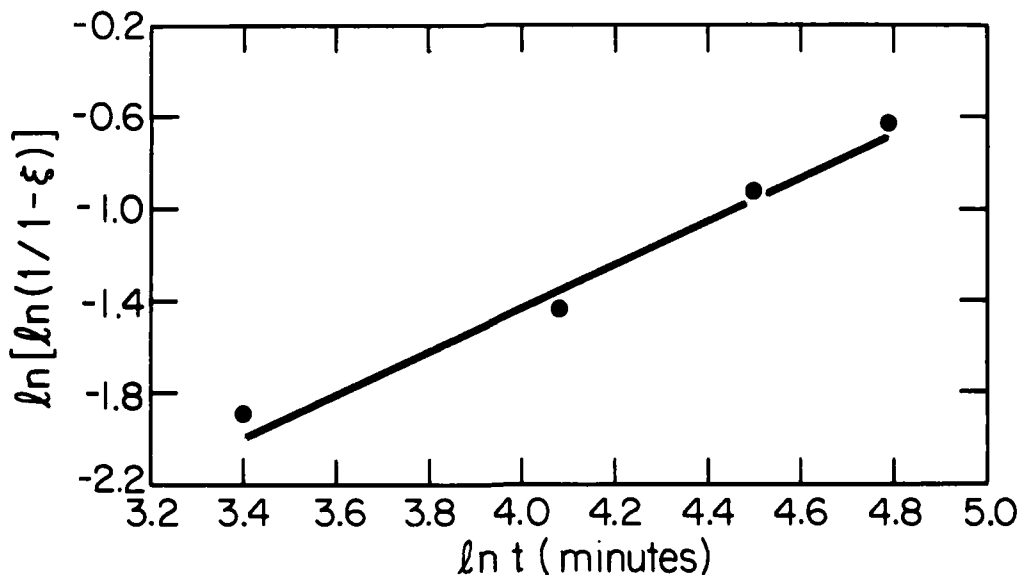
Figure 54. Functional dependence between volume fracture crystallized (ξ) and time (t).

137

The nucleation rate is exponentially dependent on a term[80] proportional to ΔG_c + Q where ΔG_c is the free energy of forming a critical size nucleus and Q is the activation energy for transport across the amorphous-crystalline interface. Using approximations for the pre-exponential terms, we estimate the sum ΔG_c + Q = 166 kcal/mole at 1340°C. The variable temperature experiments, Table 23, were used to determine that the sum ΔG_c + Q decreased with increasing temperature. The relative dependencies of the two terms could not be isolated, but it is likely[80] that Q decreases at a greater rate than ΔG_c increases with increasing temperature.

Crystallization, nitriding of excess Si, and surface area reduction occurred during heat treatment of ultrafine, high purity, amorphous Si_3N_4 powder compacts. For fired samples which were partially crystalline, two types of particles were observed; spherical 200 Å diameter particles which were amorphous, and 1400 x 700 Å polycrystalline platelet shaped clusters. As the volume fraction crystallized increased, the number of polycrystalline platelets increased and the number of 200 Å diameter amorphous particles decreased. Fully crystalline samples were composed entirely of polycrystalline clusters. No linear shrinkage was observed but the 1400 x 700 Å platelets were found to be approximately 78% dense. Thus, densification occurred on a local scale but not on a macroscopic scale. Surface area reductions were concurrent with the increase in volume fraction crystallized and a linear relation between surface area and crystallinity was observed.

The crystallization kinetics followed a model based on nucleation rate controlled kinetics with growth being physically confined to a volume which is small in comparison with the growth-rate • growth-time product.

Propagation of the amorphous crystalline interface through the interparticle neck region was found in the current study to be energetically favorable for neck sizes greater than 10 Å, which is essentially point contact. However, microstructural analysis of fired samples showed that the interparticle penitration did not occur for distances greater than 2-3 particle diameters.

While bulk densification was not observed, it is highly likely that it would occur with high density, high coordination number green compacts. These bodies could have the ordered structures shown in Figure 1 or random close packed structures. In either case it is absolutely essential to achieve complete dispersion of the particles so the microstructural instabilities resulting from agglomerates are avoided. Localized densification also was associated with the crystallization of the amorphous Si_3N_4 powders produced by the laser process. Thus, it appears likely that the ultimate goal of achieving densification of Si_3N_4 powders without resorting to pressure and/or additives is realizable with these unique powders.

V MECHANICAL PROPERTY EVALUATIONS OF REACTION BONDED Si_3N_4 MADE FROM LASER SYNTHESIZED Si POWDERS

Mechanical testing was performed on several reaction bonded Si_3N_4 (RBSN) samples made from laser synthesisized powders, to: (a) evaluate the modulus of rupture (MOR) or fracture strength, hardness (H), and fracture toughness (K_{IC}), and (b) empircially provide initial data for process optimization. Superior mechanical properties were anticipated based on microstructural analyses of the parts made from these powders.

Previous research on RBSN revealed a complex relationship between mechanical properties and both microstructure and the test samples' entire processing history. Many trends have proven so subject to exceptions and caveats because of the inherent complexity of the problem that they lose validity as generalizations; however the following are generally true. Room temperature strength, hardness and fracture toughness generally increase with reduced porosity, more complete reaction and reduced scale of microstructural features. It is the simultaneous achievement of this combination of characteristics which are possible with the laser synthesized powders that allows substantially improved mechanical properties to be anticipated.

It has been shown recently[81] that the increase in strength anticipated with improved microstructure characteristics may be obscured because of flaws introduced during sample cutting and grinding operations. This work indicated that for the Brown University RBSN designated K-series Si_3N_4, ($\rho = 79\%$ theoretical) the four point MOR strength ranged from 200 to 290 MN m^{-2} with no direct dependance on the various microstructures produced. This was a result of the high fraction (75%) of failure initiating flaws introduced as a result of the grinding operation, thereby obscuring the expected relationship between MOR and microstructure. The fracture toughness of these samples were measured as 2.316 ± 0.180 MN $m^{-3/2}$ by the notched beam technique and 2.47 MN $m^{-3/2}$ by the relationship between measured fracture stress and fractographically determined flaw size. Fracture toughness also was found to be independent of the various

141

microstructures produced provided the density was kept constant. For independent reasons, these experiments did not reveal anticipated microstructural effects.

Strength and fracture toughness (K_{IC}) parameters were characterized for RBSN samples made from laser synthesized Si powders. Strengths were measured directly by the 4-point flexure technique (MOR) and indirectly by Vickers hardness measurements. Hardness values correlate with tensil strengths and are frequently a better measure of true strength since they are not as sensitive to work damage. Fracture toughness was evaluated on all samples from the lengths of cracks induced with a hardness indentor,[82] and in some cases fractographically from the broken MOR samples. Failure origions were identified fractographically. RBSN samples were also made from Norton NC350[†] and Brown University material type K-8. Both of these high quality materials have been characterized extensively so they provide both a means of corroborating the measurement techniques used in this study as well as a direct basis for comparison for the new material.

Hardness measurements were made using a Vickers indentor with 0.981, 1.962, and 4.905 N loads on metallographically polished specimens (1 μm diamond final polish). The hardness H is calculated from the relation $H = 2\ P/A^2$, where: P is the applied load (Newtons) and A is the average indent diagonal (meters) at load P. The loads were kept low enough to prevent any crack formation at the indent apices.

Modulus of rupture values were measured on Si_3N_4 samples cut from the parent pellet and diamond ground[††] (320 grit) to final dimensions of 0.795 x 0.148 x 0.072 ± 0.005 cm with a 0.008 cm 45° edge chamfer to remove fracture origins at the corners. It was only possible to obtain one MOR sample from each pellet. Measurements were made using a knife edge 4-point bend fixture with an inner span and outer span of 0.190 and 0.510 cm respectively. A cross head speed of 0.05 cm/min was used on an Instron testing machine. The limited number of samples evaluated did not provide a

[†] Norton, Co., Worcester, MA.
[††] Bomas Machine Specialist, Somerville, MA

142

statistical discription of strength; however, when combined with the additional information obtained from fractographic analyses, the results do permit properties to be evaluated. Fractography yields the characteristics of the fracture origin (its location, size and source) and an independant measure of the fracture toughness K_{IC}.

Fracture toughness measurements were performed on metallographically prepared samples using a modified Vickers indentation technique as described by Anstis et al[82]. In this technique, the Vickers pyramid indenter is loaded to the point where crack patterns associated with the indentation are produced. Under sufficiently high loads, penny shaped radial/median cracks are produced with a dimension C local to the indent. These cracks propagate and grow to their final dimensions as the indentor is unloaded. In this manner the fracture toughness K_{IC} can be obtained from the expression:[82]

$$K_{IC} = B \left(\frac{E}{H}\right)^{1/2} P/C^{3/2} \tag{43}$$

where:

      B is a material independent constant
        for the Vickers geometry,

      E is Youngs modulus,

      H is the Hardness as defined above,

      P is the applied load,

      C is the average measured crack length from indent
        center to crack tip.

To permit the calculation of fracture toughness, one must determine the constant B for the working equation empirically. This is done by using a set of standard materials where values of K_{IC} and E are determined anaccurately by using independent techniques. Once accomplished, measurements of the indentation fracture parameter $P/C^{3/2}$ will allow accurate K_{IC} determination. Anstis et al[82] determined a value of 0.016 ± 0.004 for the constant B with the Vicker's geometry.

Table 26 shows the results of all of the mechanical testing. The hardness values for the Si_3N_4 materials produced from laser synthesized Si

TABLE 26

Summary of Mechanical Property Measurements

Sample	806SB-8	803SB-13	804SB-12	806SB-7	804SB-11	803SB-12	K-8	NC350
Sintered Density % Si Theoretical	46[+]	56	59	59	70	79	64[+]	68[++]
Nitriding History	†	†	†	†	†	†	**	††
% Nitrided by Weight	100	93	92	97	83	68	99	99
Phase Composition by X-ray, α/β/Si	82/12/1	73/20/1	77/19/3	77/20/2	50/50/1	34/43/21	75/25/1	90/10/1
Nitrided Density % Si_3N_4 Theoretical	57	69	70	72	81	88	79	83
Measured MOR (MN m^{-2})	259.9	304.1	288.9	155.8	352.3	306.1	299.2	289.6**
Measured H (MN m^{-2})	5.9	7.9	13.3	11.9	13.9	13.2	7.0[*]	8.3
Measured K_{IC} (MN $m^{-3/2}$)	1.45	1.70	1.86	1.44	0.84	1.13	1.90	2.00
Calculated MOR (MN m^{-2}) based on density[***]	47.6	102.7	121.3	131.0	287.5	555.0	222.0	296.5
Calculated E (GN m^{-2}) based on density[***]	85	118	127	132	184	244	166	177
E (GN m^{-2} used in) K_{IC} calculation	160	160	160	160	160	160	166**	170**

[+] Not Sintered
[++] Assumed
† 1200°C, 1250°C, 1300°C, 1350°C, and 1400°C for 24 hours each
†† Trade Secret
[*] 9.81 Newton Load
** Reference 81
*** Reference 57

144

increase from approximately 6 to 13 MN m^{-2} as the nitrided density increases from 57 to 88% of theoretical. This relationship between density and hardness is expected based on an increasing load bearing area with increasing density. The measured hardness for K-8 and NC350 were 6.95 and 9.6 MN m^{-2} respectively, values that are esentially equal to one another and that appear to be significantly below those for laser synthesized material of comparable nitrided density (804SB-11). Previous results have shown[81] that these two materials exhibit essentially the same MOR strenghts. This indicates that the hardness and the inherent strengths anticipated for high density, fully reacted Si$_3$N$_4$ materials produced by the combined sintering and nitriding of laser synthesized Si would be superior to conventionally prepared Si$_3$N$_4$ materials.

The strengths measured by the MOR technique appear to be accurate. These results indicate a strength of 299.2 MN m^{-2} for K-8 which is close to a reported value[81] of 289.6 MN m^{-2}. The small sample dimensions, the testing fixtures, measuring procedures and the sample fabrication procedures all appear to be proper.

Four point bend strength values varied from a low of 155.8 MN m^{-2} for 806SB-7 to a high of 352.3 MN m^{-2} for 804SB-11. On first consideration, these strength results suggest that the current Si$_3$N$_4$ material is quite similar to K-8 and NC350. In one case our material was stronger but in two cases it was weaker. Fractographic analysis of the failure initiating flaws shows that the inherent strengths of samples made of the laser synthesized powder are probably superior as anticipated from the hardness measurements.

For K-8 Si$_3$N$_4$, the flaw that induced failure was a relatively large pore near the corner of the specimen: a typical microstructural defect. In contrast, each sample of the laser synthesized Si$_3$N$_4$ material failed as a result of a grinding induced flaw. Thus, the measured strengths were not determined by the microstructural defects inherent to the material, but by defects introduce by the surface grinding operation. This result indicates that the "true" fracture strengths of these materials are significantly higher than the measured values. A second important result is that the measured strengths of the low density samples were much higher than would be expected based on their nitrided densities.[57] As an example, 806SB-8 and

803SB-13 exhibited strengths of 259.9 and 304.1 MN m^{-2} respectively while, based on their nitrided densities, one would expect[57] strengths of only 47.6 and 100 MN m^{-2} respectively. The difference would have been even greater if true strengths had been achieved. The reason that this trend does not continue to the higher density samples (803SB-12), is probably related to the presence of unreacted Si.

The fracture toughness (K_{IC}) measurements using the Vickers indentation method, are also given in Table 26. The value of the constant B in Equation 43 was determined to be equal to 0.011 for Si$_3$N$_4$ by setting the K_{IC} value for NC350 equal to 2.0 MN m$^{-3/2}$ and using Young's modelus of 177 GNm^{-2}. The reported values of K_{IC} for NC350[81][83] range from approximately 1.8 to 2.3 MN m$^{-3/2}$ so the value selected for these calculations is near the average of this range and is also the value Anstis used.[82] Analysis of the K-8 Si$_3$N$_4$ material (57.86N load) gave a K_{IC} = 1.9 MN m$^{-3/2}$ in good agreement with the NC350 material. Previous work using a a notched beam technique[81] yielded K_{IC} values of 2.31 and 2.316 MN m$^{-3/2}$ for NC350 and K-8 respectively. In both cases, the tests indicate that NC350 and K-8 Si$_3$N$_4$ have similar K_{IC} values. The differences between the absolute values is insignificant.

Values measured for K_{IC} ranged from 0.84 to 1.86 MN m$^{-3/2}$ for Si$_3$N$_4$ materials produced from laser synthesized boron doped Si. The results suggest that the fracture toughness values for these Si$_3$N$_4$ materials are generally slightly lower than for NC350 and K-8 Si$_3$N$_4$. For samples 806SB-8, 803SB-13, 804SB-12, and 806SB-7, the densities are significantly lower than for NC350 and K-8 hence one would expect much lower K_{IC} values, yet the K_{IC} values are only slightly lower. This implies that comparable density fully reacted samples should exhibit K_{IC} values equal to or higher than NC350 or K-8. While 804SB-11 and 803SB-12 have comparable or greater densities than NC350 and K-8, their K_{IC} values are lower because these two samples contain significant amounts of unreacted Si.

VI SUMMARY

This research program has investigated both the means of producing Si, Si_3N_4 and SiC powders having highly special characteristics as well as means of fabricating these particulate materials into ceramic bodies that exhibit superior characteristics. The powders which were sought will permit major changes in powder processing techniques and improvements in the defect structures of these brittle materials. Ideally, it should be possible to create green bodies of these materials having a close-packed ordered arrangement of the constituent particles (Figure 1) as has been done with metallic and oxide dispersed systems. These bodies will exhibit a uniform, precisely defined shrinkage with sintering. Flaw sizes should approximately equal the diameters of constituant particles. Coordination numbers should be high, which will virtually eliminate rearrangement and will enhance densification process rates. Even if the ordered structures are not achieved, it should be possible to attain most of the anticipated advantages in random structures.

The powder characteristics which were sought include small size, uniform size, equiaxed (tending toward spheres) in shape, composed of a specific phase(s), compositionally pure and free of agglomerations. In principle, gas phase synthesis processes can achieve these attributes, however, variations in time-temperature history throughout conventionally heated reaction zones cause unacceptably large variations in particle characteristics. Also, the typically long exposure to elevated temperatures causes particles to bond to one another. We have elected to heat the reactant gases by absorbed IR light emitted from a laser. This unique means of transferring energy to the gas permits precise, uniform heating with unusually high heating rates and small reaction volumes. It was anticipated that this laser heated synthesis process would overcome the deficiencies of conventional gas phase processes, while retaining their advantages.

In this process, optically absorbing gases are passed through a laser beam to cause a reaction within the region where the two intersect. We have

147

investigated process geometries in which the gas stream and the laser beam intersect orthogonally and also where they intersect coaxially from opposite directions (counter flow). A CO_2 laser was used as the energy source to induce reactions in gases containing active components such as SiH_4, NH_3, CH_4, C_2H_2 and B_2H_6 as well as inert dilutants. The resulting Si, Si_3N_4 and SiC powders were collected and characterized as a function of process variables.

The results of this research program demonstrate that this laser heated synthesis process produces powders with virtually all of the desired characteristics. The resulting particles are small, uniform in size, spherical and pure. The particles appear to be attached to one another in chain-like agglomerates. Light scattering measurements show that the powders leave the reaction zone as individual particles so agglomerates probably form where the powders are captured or during subsequent handling. Direct examination by TEM revealed no neck formation between the particles of the Si_3N_4 and SiC powders. We anticipate that they can be dispersed. It has not been determined whether the necks observed between Si particles result from elastic deformation or from sintering, but it was demonstrated that a large fraction of them could be dispersed completely.

Besides producing powders with ideal characteristics, this laser heated synthesis process is extremely efficient. Approximately 95% of SiH_4 is converted to Si or Si_3N_4 powder in a single pass through the laser beam. Also Si, Si_3N_4, and SiC powders can be produced from these reactants with as little as 2 kWhr of energy per kilogram of powder. It is likely that this process can produce both a superior and lower cost powder than conventional gas phase or solid phase synthesis processes.

Much of our efforts have focused on developing an analytical description of the laser heated synthesis process. To develop a model, many fundamental property measurements were required, such as detailed optical absorptivity measurements for reactant gases as a function of pressure and emitted wavelength. Emissions from the reaction have been studied to identify reaction species and to estimate the reaction temperature. Computer analysis of the gas flow were used to predict gas

stream dimensions and velocities. Combined with direct observations of both the reaction positions relative to the laser beam and the reaction temperatures, these analyses and characterizations have been used to describe the time-temperature history of the reactant gases throughout the course of the reaction.

With the process conditions used for the majority of these synthesis experiments (laser intensity = 765 watts/cm^2, pressure = 0.2 atm, gas velocity = 500 cm/sec), reaction products were evident within 3-5 mm penetration into the laser beam. Heating rates to the reaction temperature (nominally 1000°C) were approximately 10^{6}°C/sec. The reaction was initiated in approximately 10^{-3} seconds and was completed in, at most, 7.5 x 10^{-3} seconds. The individual particles grew at a nominal rate of 1800 Å/sec and depleted a volume of reactant gas equal to a sphere approximately 1 x 10^{-4} cm in diameter.

Most process variables were manipulated to determine their effect on particle characteristics. These interactions were interpreted in terms of changes in the process. Laser intensities up to 10^5 watts/cm^2 produced heating rates in excess of 10^{8}°C/sec. Variations in heating rates within different gas streams were analyzed in terms of the Gaussian intensity in the laser beam and the parabolic velocity profile in the stream. The effects of nonabsorbing gases were also considered. The process variables effected the reaction temperature, the corresponding gas depletion volume and resulting particle size. Increased reaction temperature caused the particle size of the Si$_3$N$_4$ powders to decrease and the size of the Si and SiC powders to increase. The relative temperature coefficients for the nucleation and growth processes exhibited by these reactions are different from one another.

The general characteristics of the powders of the three materials are similar to one another, but they differ in detail. Silicon powders were crystalline under all but the lowest laser intensity conditions where they are at least partially amorphous. Individual crystalline particles consisted of multiple grains which were 1/3-1/5 of the particle diameter. Mean Si particle diameters were in the range of 190-1500 Å with a standard

deviation of 35-50%. Silicon nitride powders were almost always amorphous. Mean particle sizes ranged from 25-220 Å, depending primarily on the laser intensity. These powders were more uniform in size than the silicon powders. Diameter standard deviations were approximately 25% and the ratio between the largest to the smallest observed particle was less than 2.5. The stoichiometry varied with processing conditions. High laser intensities yielded stoichiometric powders; lower intensities produced powders which were rich in silicon. The silicon carbide powders are comprised of crystalline β-SiC and Si, contain up to 10% excess Si and/or C, and have particle sizes ranging from 200-500 Å. Powders of all three materials are comprised of spherical particles whose BET equivalent diameters equaled the directly observed mean diameters. This observation and direct density measurements indicate that individual particles contain no porosity. All of the materials were quite free of contaminants. The oxygen impurity level decreased progressively as handling procedures improved. In later powder later powder batches, the O_2 content was less than 0.05% by weight. Levels of other impurities detected by emission spectroscopy generally totaled less than 100 ppm.

Resulting powders have been processed into pellets in the controlled atmosphere of a glove box. Silicon powders were nitrided and silicon nitride powders were sintered without sintering aids. The results of the nitriding experiments were particularly important. Silicon powders were nitrided to completion in the form of pellets whose densities could be controlled by a pre-nitriding sintering step. Unusually rapid reaction rates were observed because of the small particle size, but no problems were encountered with thermal runaway. The grain size and typical interparticle pore size in the resulting pieces were less than 1000 Å. Larger pores (~ 1-5 μm) observed on occasion probably resulted from agglomerates and can therefore be eliminated with adequate dispersion. The results of the Si_3N_4 sintering experiments indicated that, for the first time, densification occurred without the use of sintering aids or pressure. Uniform macroscopic densification should be observed with the ordered green structures shown in Figure 1. This will have important consequences for improving high temperature mechanical properties.

A systematic study of developing stable dispersions was undertaken. n-Propanol was the best organic liquid studied. Pieces were centrifugally cast from these dispersions.

Preliminary mechanical property characterizations of reaction bonded Si_3N_4 samples made from these Si powders, indicate that superior properties can be achieved using the laser synthesized powders. Without virtually any interactive optimization between pellet fabrication procedures and properties, the mechanical characteristics equaled or exceeded those of highly developed RBSN materials. For samples with either lower densities, lower percent reaction, and/or microstructural heterogenieties, hardnesses were higher, strengths were generally comparable or better than, and toughnesses were comparable to K-8 and NC350 Si_3N_4, which are regarded as high quality materials. Microstructural and fractographic analyses showed that the strength limiting defects were not intrinsic to the material. With readily definable improvements in fabrication procedures, the mechanical properties of this laser synthesized material should be substantially better than others.

This research program has easily achieved its primary objective. Powders which result from the laser heated, gas phase synthesis process have most of the characteristics presumed to be ideal for ceramic powders. Also, the resulting powders can be processed into high quality pieces. The process also appears capable of reducing the cost of these powders because it requires very little energy per kilogram of powder and utilizes feed materials very efficiently. It still needs to be developed further to eliminate the tendency to form chain-like agglomerates and to increase the mean particle size. For many materials, it is desirable to have mean particle sizes of approximately 1000 Å rather than 250 Å as typically produced by this process. Achieving the larger particle size will require an improved understanding of the nucleation an growth processes. It is also important to apply the process to other materials. Many electronic, magnetic, and optical ceramic processes would benefit from using powders with the characteristics demonstrated in this research program.

Appendix I

Lot #	Laser Intensity (W/cm^2)	Cell Pressure (atm)	SiH_4 ($\frac{cm^3}{min}$)	NH_3 ($\frac{cm^3}{min}$)	Ar † ($\frac{cm^3}{min}$)	Ar †† ($\frac{cm^3}{min}$)	Max. Gas Velocity at Nozzle (cm/sec)	Reaction Zone Temp. by Pyrometer (°C)	Filter (g)	Total in Cell +Filter (g)	Total Eff. (%)
						Run Conditions				Wt. Collected	
215S	531	0.2	11	0	0	1000	104	*	*	2.6	90
216S	707	0.2	20	0	0	1000	188	*	*	8.1	86
026S	531	0.2	11	0	0	1000	104	*	*	3.0	30
026S	531	0.2	11	0	0	1000	104	*	2.08	*	*
027S	531	0.2	11	0	0	1000	104	*	5.10	*	*
030S	531	0.2	11	0	0	1000	104	*	7.00	*	*
031S	531	0.2	11	0	0	1000	104	*	2.10	*	*
032S	531	0.2	11	0	0	1000	104	*	2.63	*	*
033S	531	0.2	11	0	0	1450	104	*	6.67	6.67	61
034S	531	0.2	11	0	0	1450	104	*	6.23	6.23	84
035S	531	0.2	11	0	0	1450	104	*	7.27	7.27	96
101S	531	0.2	11	0	0	1000	104	*	1.50	3.75	*
103S	531	0.2	11	0	0	1000	104	*	9.00	10.00	76
622S	601	0.35	66	0	0	735	356	1055	6.76	*	90
623S	601	0.35	110	0	0	735	593	1025	8.30	*	100
624S	601	0.35	40	0	0	735	216	1200	9.55	*	100
625S	531	0.2	11	0	0	700	104	1030	2.27	*	92
626S	531	0.2	13	0	0	700	122	1060	6.38	*	92
627S	531	0.2	7.5	0	0	700	71	850	2.27	*	90

* Not Measured
† Dilution
†† Annular and Window

153

Appendix I (cont.)

Lot #	Run Conditions								Wt. Collected		
	Laser Inten- sity (W/cm²)	Cell Pressure (atm)	SiH₄ (cm³/min)	NH₃ (cm³/min)	Ar † (cm³/min)	Ar †† (cm³/min)	Max. Gas Velocity at Nozzle (cm/sec)	Reaction Zone Temp. by Pyrometer (°C)	Filter (g)	Total in cell +Filter (g)	Total Eff. (%)
6628S	531	0.2	8.8	0	0	700	83	955	5.01	*	100
6629S	531	0.2	5.5	0	0	700	52	790	0.99	>1.53	>85
6630S	531	0.2	104	0	0	700	981	950	7.71	*	98
6631S	531	0.2	38	0	0	700	358	1050	6.26	*	87
6632S	531	0.2	38	0	0	700	358	1055	6.86	*	88
6633S	531	0.2	60	0	0	700	566	980	7.72	*	90
6634S	531	0.2	6.5	0	31.5	700	358	750	2.20	*	80
6635S	531	0.35	66	0	0	735	356	*	7.90	*	89
6636S	601	0.35	16	0	0	735	86	1215	2.34	*	86
6637S	531	0.2	12.7	0	25.3	700	358	830	1.68	*	81
6638S	266	0.35	66	0	0	735	356	930	4.92	*	98
6639S	531	0.2	25.3	0	12.7	700	358	1030	3.37	*	88
6640S	177	0.35	66	0	0	735	356	910	4.20	*	92
6641S	531	0.2	50	0	25	700	707	970	4.40	*	90
6642S	531	0.2	19	0	19	700	358	970	2.00	*	88
6643S	601	0.35	11	0	0	560	59	1125	1.59	*	89
6644S	601	0.35	28	0	0	735	151	1265	2.75	*	90

* Not Measured
† Dilution
†† Annular and Window

154

Appendix I (cont.)

Lot #	Laser Intensity (W/cm²)	Cell Pressure (atm)	SiH₄ (cm³/min)	NH₃ (cm³/min)	Ar † (cm³/min)	Ar †† (cm³/min)	Max. Gas Velocity at Nozzle (cm/sec)	Reaction Zone Temp. by Pyrometer (°C)	Filter (g)	Total in Cell +Filter (g)	Total Eff. (%)
									Wt. Collected		
645S	5411	0.35	66	0	0	735	356	1230	4.11	*	91
646S	424	0.35	66	0	0	735	356	1085	5.33	*	94
648S	406	0.35	66	0	0	735	356	1105	6.09	*	92
649S	601	0.35	110	0	0	735	593	1100	6.19	*	97
650S	531	0.6	66	0	0	960	207	1335	4.57	*	91
651S	531	0.6	90	0	0	960	282	1285	5.19	*	95
652S	531	0.6	30	0	0	960	94	1220	2.44	*	89
653S	531	0.2	38	0	0	700	358	*	*	*	*
654S	531	0.2	12.7	0	25.3	700	358	*	*	*	*
655S	265	0.2	30	0	30	1000	566	800	3.21	0.30	85
656S	531	0.6	45	0	0	960	141	1305	2.25	*	87
657S	531	0.6	110	0	0	960	345	1280	7.10	*	89
658S	131	0.35	66	0	0	735	356	865	3.70	*	97
659S	531	0.6	19.5	0	0	960	61	1200	1.20	*	96
660S	176	0.2	20	0	40	1000	566	*	0.93	*	58
661S	531	0.2	28.5	0	9.5	700	358	1035	*	*	*
662S	531	0.2	31.7	0	6.3	700	358	1025	3.45	*	90
663S	531	0.2	19	0	19	700	358	*	*	*	*

* Not Measured
† Dilution
†† Annular and Window

155

Appendix I (cont.)

				Run Conditions					Wt. Collected		
Lot #	Laser Inten-sity (W/cm^2)	Cell Pressure (atm)	SiH$_4$ $\frac{cm^3}{min}$	NH$_3$ $\frac{cm^3}{min}$	Ar † $\frac{cm^3}{min}$	Ar †† $\frac{cm^3}{min}$	Max. Gas Velocity at Nozzle (cm/sec)	Reaction Zone Temp. by Pyrometer (°C)	Filter (g)	Total in Cell +Filter (g)	Total Eff. (%)
024SN	2 x 10^4	0.8	8	80	0	1000	207	*	*	small	*
025SN	2 x 10^4	0.9	5.4	54	0	1000	124	*	*	8.0	~100
400SN	531	0.75	11	110	0	1000	304	*	4.77	*	86
401SN	531	0.75	11	110	0	1000	304	*	6.82	*	89
402SN	531	0.75	11	110	0	1000	304	*	6.85	*	71
221SN	2 x 10^4	0.75	40	80	—	1025	679	1390	9.10	*	53
222SN	2 x 10^4	0.75	20	100	—	1100	679	1105	9.80	*	80
405SN	2 x 10^4	0.75	42	78	—	1000	302	*	*	*	*
LSB1	531	0.2	25	0	13#	700	358	1050	*	*	87
LSB3	531	0.2	25	0	13#	700	358	1025	6.80	*	82
802SB	531	0.2	50	0	25#	900	707	1010	4.97	*	96
803SB	531	0.2	50	0	25#	900	707	1015	7.76	*	81
804SB	531	0.2	50	0	25#	900	707	1015	6.55	*	94
805S	531	0.2	50	0	25	900	707	985	7.30	*	91
806SB	531	0.2	50	0	25#	900	707	1010	6.17	*	94
808S	531	0.2	50	0	25	900	707	985	6.71	*	91
809S	531	0.2	50	0	25	900	707	975	6.90	*	91
813SB	531	0.2	50	0	25#	900	707	1030	5.59	*	95

* Not Measured
† Dilution
†† Annular and Window
# Ar + 1% B_2H_6

156

Lot Number	Analysis Si	N (wt %)	O	Excess Si (%)	BET (m²/g)	(Å)	TEM Diameter (Å)	Crystallite† Size (Å)
215S	–	–	*	–	60	429	*	*
216S	–	–	0.36	–	28.5	903	*	*
026S	–	–	0.17	–	83.0	310	*	*
027S	–	–	0.22	–	67	380	*	*
030S	–	see 01S		–	78	330	*	*
031S	–	see 01S		–	70	370	*	*
032S	–	see 01S		–	68	380	*	*
033S	–		*	–	110	230	*	*
034S	–	see 01S		–	79	325	*	*
035S	–	see 01S		–	94	270	*	*
101S	–		0.14	–	46.5	550	*	*
102S	–		0.14	–	*	*	*	*
103S	–		0.11	–	68	380	*	*
01S	(030S+031S+ 032S+034S+ 035S)		0.67	–	81	320	*	*
622S	–	–	<0.064	–	25.1	1027	*	348
623S	–	–	*	–	44.2	583	*	171
624S	–	–	*	–	23.3	1107	*	372
625S	–	–	0.28	–	38.8	664	*	162
626S	–	–	*	–	39.0	661	*	202
627S	–	–	*	–	64.1	402	*	86
628S	–	–	*	–	51.0	505	*	127
629S	–	–	*	–	70.2	367	*	75
630S	–	–	*	–	61.5	419	356	107
631S	–	–	0.70	–	42.5	604	525	200
632S	–	–	0.67	–	40.7	632	*	191
633S	–	–	*	–	48.5	530	*	144
634S	–	–	*	–	87.6	294	275	68
635S	–	–	*	–	27.6	932	*	338
636S	–	–	*	–	27.7	931	*	326
637S	–	–	*	–	73.8	349	*	83
638S	–	–	*	–	67.8	380	*	71
639S	–	–	*	–	36.3	709	*	224
640S	–	–	*	–	73.2	352	*	62
641S	–	–	*	–	44.8	575	*	143

Powder Characteristics

* Not Measured
† Assumes Gaussian-Shaped Peaks

Appendix II (cont.)

Lot Number	Analysis Si	N (wt %)	O	Excess Si (%)	BET (m²/g)	(A)	TEM Diameter (A)	Crystallite[†] Size (A)
642S	–	–	*	–	43.9	586	*	188
643S	–	–	*	–	30.0	859	*	293
644S	–	–	*	–	24.3	1059	*	335
645S	–	–	*	–	23.3	1106	*	353
646S	–	–	*	–	34.1	755	*	254
648S	–	–	*	–	37.4	689	*	217
649S	–	–	*	–	44.2	583	*	197
650S	–	–	*	–	17.5	1469	*	414
651S	–	–	*	–	20.0	1290	*	405
652S	–	–	*	–	24.9	1033	*	329
653S	–	–	*	–	42.1	612	*	191
655S	–	–	*	–	89.1	289	*	56
656S	–	–	*	–	19.1	1351	*	433
657S	–	–	*	–	20.1	1284	*	353
658S	–	–	*	–	80.2	321	*	Amorphous
659S	–	–	*	–	27.2	945	*	333
660S	–	–	*	–	136.0	189	*	Amorphous
661S	–	–	*	–	42.3	609	*	222
662S	–	–	*	–	41.2	625	*	204
221SN	55.3	35.3	1.78	1.0	36.0	517	*	305
222SN	55.5	37.0	1.86	<1	112.0	168	*	Amorphous
405SN	57.3	37.9	.32	<1	98.0	195	*	Amorphous
LSB1	–	–	*	–	42.0	613	*	*
LSB3	–	–	*	–	34.4	744	*	192
802SB	–	–	*	–	47.2	546	*	*
803SB	–	–	*	–	46.3	556	*	*
804SB	–	–	*	–	43.1	597	*	*
805S	–	–	*	–	44.6	577	*	*
806SB	–	–	*	–	46.1	558	*	*
808S	–	–	*	–	49.6	521	*	*
809S	–	–	*	–	50.6	508	*	*
813SB	–	–	*	–	–	–	*	*
024SN	*	*	*	*	*	*	*	Amorphous
025SN	*	*	1.18	13	58.5	332	*	Amorphous
400SN	*	*	*	*	80.1	250	*	Amorphous
401SN	59.7	30.94	*	13	84.5	237	*	Amorphous
402SN	62.4	30.5	.34	17	92.1	217	*	Amorphous

† Assumes Gaussian-Shaped Peaks
* Not Measured

158

REFERENCES

1. Bowen, H.K., October 1980, Physics and Chemistry of Packing Fine Ceramic Powders, under Contract DE-AC02-80ER10588, M.I.T., Cambridge, MA.

2. Haggerty, J.S. , and Cannon, W.R., October 1978, Sinterable Powders from Laser Driven Reactions, under Contract N00014-77-C0581, M.I.T., Cambridge, MA.

3. Haggerty, J.S., and Cannon, W.R., July 1979, Sinterable Powders from Laser Driven Reactions, under Contract N00014-77-C0581, M.I.T., Cambridge, MA.

4. Haggerty, J.S., and Cannon, W.R., July 1980, Sinterable Powders from Laser Driven Reactions, under Contract N00014-77-C0581, M.I.T., Cambridge, MA.

5. Gaydon, A.G., and Wolfhard, H.G., Flames: Their Structure, Radiation, and Temperature, Chapman and Hall, Ltd., London, 1970.

6. Van de Hulst, H.C., Light Scattering by Small Particles, John Wiley and Sons, Inc., N.Y., 1957, Chap. 14.

7. Suyama, Y., Marra, R., Haggerty, J.S., and Bowen, H.K., "Synthesis of Ultrafine SiC Powders by Laser Driven Gas Phase Reaction", to be published.

8. Kramer, T.M., "Dispersion and Surface Studies of Laser Synthesized SiC", Ph.D Research in progress, M.I.T.

9. Mitchell, A.C.G., and Zemansky, M.W., Resonance Radiation and Excited Atoms, Cambridge Univ. Press, Cambridge, 163, 1961.

10. Johns, J.W.C., and Kreiner, W.A., "Measurement and Analysis of the v_4 Band of Silane", J. Mol. Spectrosc. 60, 400-11 (1976).

11. Purnell, J.H., and Walsh, R., "Pyrolysis at Monosilane", Proc. Royal Soc., Series A, London, p. 545, 1966.

12. Haas, C.H., and Ring, M.A., "Reaction of Silyl Radical and Silylene with Acetyiene and Application to Orbital Symmetry to the Pyrolysis of Silane and Disilane", Inorganic Chemistry, 14, 2253, (1975).

13. Galasso, F.S., Veltri, R.D., and Croft, W.J., "Chemically Vapor Deposited Si_3N_4", Bull. Am. Ceram. Soc., 57, 453 (1978).

14. Billy, M, Brossard, M., Desmaison, J. Girard, D., and Goursat, P., "Si Oxynitride by Ammonolysis of Chlorides", J. Am. Ceram. Soc., 58, 254 (1975).

15. Cochet, G., Mellottee, H., and Delbougo, R., "Experimental Investigation of Gas Phase in a Chemical Vapor Deposition Reaction: Application to the Silane-Ammonia Reaction leading to Silicon Nitride Deposits", J. Electrochem. Soc., 125, 487-92, 1978.

16. Greskovich, C.D., Prochazka, S., and Rosolowski, J.H., Basic Research on Technology Development for Sintered Ceramics, Report AFML-TR-76-179, G. E. Research on Technology Development Laboratory under contract with AF Materials Laboratory, November, 1979.

17. Lin, Sin-Shong, J. Colloid and Interface Sci., 124, 1945 (1977).

18. Dubois, I., "Absorption Spectrum of the Free SiH_2 Radical" Canadian J. Physics, 46, 2485 (1968).

19. Pease, R.W.B., and Gaydon, A.G., The Identification of Molecular Spectra, 4th Ed., Chapman and Hall, London, 1976.

20. Dressler, K., and Ramsay, D.A., Phil. Trans., A, 251, 553 (1959).

21. Braker, W., and Mossman, A.L., Matheson Gas Data Book, Matheson Gas Products, E. Rutherford, NJ, 5th Ed., 506 (1971).

22. Rutgers, G.A.W. and De Vos, J.C., "Relation between Brightness, Temperature, True Temperature and Colour Temperature of Tungsten", Physica, XX, 715-20 (1954).

23. Kuhl, Ch., Schlotterer, H. and Schwidefsky, F., "Optical Investigation of Different Silicon Films", J. Electrochem. Soc., 121, 1496-1500 (1974).

24. Greskovich, G., and Rosolowski, J.H., "Sintering of Covalent Solids", J. Am. Ceram. Soc., 59, 285-88 (1976).

25. JANAF Thermochemical Tables, 1971, NSRDS-NBS37.

26. Hogness, T.R., Wilson, T.L., and Johnson, W.C., "The Thermal Decomposition of Silane", J. Am. Chem. Soc., 58, 108 (1936).

27. Devyatykh, G.G., Kedyarkin, V.N., and Zorin, A.D., "Kinetics of the Thermal Decomposition of Monosilane, Arsine, and Monosilane with Arsine Impurity", Russ. J. Inorg. Chem., 18, 1528 (1965).

28. Niki, H. and Mains, G.J., "Mercury-Photosensitized Decomposition of Monosilane", J. Phys. Chem., 68 304 (1964).

29. White, A. and Rochow, E.G., "Reactions of Silane with Unsaturated Hydrocarbons", J. Am. Chem. Soc., 76, 3897 (1954).

30. Oraevskii, A.N., Pankatov, A.V., Skachkov, A.N., and Shabarshin, V.M., "Laser-Chemical Decomposition of Monosilane", High Energy Chem., 12, 48 (1978).

31. Deutsch, T.F., "Infrared Laser Photochemistry of Silane", J. Chem. Phys., 70, 1187 (1979).

32. Volmer, M. and Weber, A., "Keimbildung in ubersattigten Gebilden", Z. Phys. Chem., 119, 277 (1926).

33. Friedlander, S.K., Smoke, Dust, and Haze, John Wiley and Sons, Inc., N.Y., 1977, Chptr.7.

34. Suyama, Y., and Kato, A., "TiO$_2$ Produced by Vapor Phase Oxygenolysis of TiCl$_4$", J. Am. Ceram. Soc., 59, 146-9 (1976).

35. Flint, J.H., "Powder Temperatures in Laser Driven Reactions", M. S. Thesis, M.I.T., 1982.

36. Powell, C.F., Chemically Deposited Nonmetals in Vapor Deposition, 343, 1966, Editors: Powell, C.F., Oxley, J. H., and Blocher, J.M., John Wiley and Sons, Inc., New York.

37. Patty, R.E., Russwarm, G.M., and Morgan, D.R., "CO$_2$ Laser Absorption Coefficients for Determining Ambient Levels of O$_3$, NH$_3$, and C$_2$H$_4$", Applied Optics, 13, 2850-4 (1974).

38. Tikhomirov, M.V., Tunitzky, N.N. and Petrjanov, J.B., "On the Influence of van der Waals Forces on Coagulation of Aerosols", Acta Physicochimica, U.R.S.S., 17, 185-96 (1942).

39. Mason, S.G., "Orthokinetic Phenomena in Disperse Systems", J. Colloid Interface Sci., 58, 275-85 (1977).

40. Eastering, K.E., and Tholén, A.R., "Surface Energy and Adhesion at Metal Contacts", Acta Metall., 20, 1001-8 (1972).

41. Kingery, W.D., Bowen, H.K. and Uhlmann, D.R., Introduction to Ceramics, John Wiley and Sons, Inc., N.Y., 1976, Chap. 5.

42. Weiser, H.B., "Inorganic Colloid Chemistry", in The Colloidal Elements, Vol. 1, John Wiley and Sons, N.Y., 1933, 14-16, 163.

43. Wegelin, G., "Ueber die Herstellung, kolloider Losungen durch mecanische Zertielung", Kolloid-Z., 14, 65-9, (1914).

44. Astfalk, R. and Gutbier, A., "Ueber kolloides Silizium. Ein Beitrag zur Kenntnis der mechanisch-chemischen Dispersionmethoden", Kolloid-Z., 15, 23-7 (1914).

45. Williams, R., and Goodman, A.M., "Wetting of Thin Layers of SiO_2 by Water", Appl. Phys. Lett., 25, 531-2 (1974).

46. Peterlin, A., "Determination of Molecular Dimension from Light Scattering Data", Progress in Biophysics, 9, 175-237 (1959).

47. Kerker, M., The Scattering of Light and Other Electromagnetic Radiation, Academic Press, N.Y., 1969, Chap. 1.

48. Okamoto, S., and Hachisu S., "Ordered Structure in Monodisperse Gold Sol", J. Colloid Interface Sci., 62, 172-81 (1977).

49. Iler, R.K., "Formation of Precious Opal", Nature, 207, 472-3 (1965).

50. DeHoff, R.T., Rummel, R.A., LaBuff, H.P., and Rhines, F.N., "The Relationship Between Surface Area and Density in Second-Stage Sintering of Metals", Modern Developments in Powder Metallurgy, Ed. H.H. Hausner, Plenum Press, N.Y., 310-31, 1966.

51. Greskovich, C.D., Prochazka, S., and Rosolowski, J.H., Basic Research on Technology Development for Sintered Ceramics, Report AFML-TR-76-179, G. E. Research and Development Laboratory under contract with AF Materials Laboratory, November, 1979.

52. Atkinson, A., Moulson, A.J., and Roberts, E.W., "Nitridation of High-Purity Silicon", J. Am. Ceram. Soc., 59, 285-88 (1976).

53. Longland, P., and Moulson, A.J., "The Growth of α- and β-Si_3N_4 Accompanying the Nitriding of Silicon Powder Compacts", J. Mater. Sci., 13, 2279-80 (1978).

54. Jennings, H.M., and Richman, M.H., "Structure, Formation Mechanisms and Kinetics of Reaction-Bonded Silicon Nitride", J. Mater. Sci., 11, 2087-98 (1976).

55. Messier, D.R., Wong, P., and Ingram, A.E., "Effect of Oxygen Impurities on the Nitridation of High-Purity Silicon", J. Am. Ceram. Soc., 56, 171-2 (1973).

56. Campos-Loritz, D. and Riley, F.L., "The Effect of Silica on the Nitridation of Silicon", J. Mater. Sci., 11, 195-8 (1976).

57. Moulson, A.J., "Reaction-Bonded Silicon Nitride: Its Formation and Properties", J. Mater. Sci., 14, 1017-51 (1979).

58. Grün, R., "The Growth of β-Si_3N_4 Single Crystals", J. Cryst. Growth, 46, 143-50 (1979).

59. Evans, A.G. and Davidge, R.W., "The Strength and Oxidation of Reaction Sintered Silicon Nitride", J. Mater. Sci., 5, 314-25 (1970).

60. Mendelson, M.I., "On Si Nitriding Kinetics and Mechanisms", J. Mater. Sci., 14, 1752-4 (1979).

61. Messier, D.R. and Wong, P., "Kinetics of Nitridation of Si Powder Compacts", J. Am. Ceram. Soc., 56, 480-5 (1973).

62. Evans, U.R., Corrosion and Oxidation of Metals, Edward Arnold Ltd., London, 1960, Chap. 20.

63. Kramer, T.M., "Nitriding of Silicon Formed by Laser Driven Decomposition of Silane", B. S. Thesis, M.I.T., 1980.

64. Danforth, S.C., "Effective Control of the Microstructure of Reaction Bonded Silicon Nitride (Si$_3$N$_4$) as Related to Improved Mechanical Properties", (Ph.D. Thesis, Brown University, 1978), Chap. 9.

65. Bird, Stewart and Lightfoot, Transport Phenomena, John Wiley and Sons, 1960, Chap. 9.

66. Coblenz, W.S., "Physics of Sintering of Silicon", Ph.D Thesis, M.I.T., 1981.

67. Mangels, J.A., "Effect of H$_2$-Ne Nitriding Atmospheres on the Properties of Reaction Sintered Si$_3$N$_4$", J. Am. Ceram. Soc., 58, 354-5 (1975).

68. Lindley, M.W., Elias, D.P., Jones, B.F., and Pitman, K.C., "The Influence of Hydrogen in the Nitriding Gas on the Strength, Structure and Composition of Reaction-Sintered Silicon Nitride", J. Mater. Sci., 14,, 70-85 (1975).

69. Hausner, H., "Pressureless Sintering of Non-oxide Ceramics" in Energy and Ceramics, Materials Science Monograph, 6, 588-95 (1980).

70. Ikegami, T., Tsutsumi, M., Matsuda, S., Shirasaki, S., Suzuki, H., "A Model Of Glass Densification with Simultaneous Grain Growth", J. Appl. Phys. 49, 4238-41 (1978)

71. Thummler, F., "Sintering and High Temperature Properties of Si$_3$N$_4$ and SiC" in Sintering Processes, Proceedings of the Fifth International Conference on Sintering and Related Phenomena, Materials Science Research, 13, 247-60 (1980).

72. Greskovich, C., and O'Clair, C., "Effect of Impurities on Sintering Si$_3$N$_4$ Containing MgO or Y$_2$O$_3$ Additives", Ceramic Bulletin, 57, 155-6 (1978)

73. Mitomo, M., "Pressure Sintering of Si$_3$N$_4$", J. Mater. Sci., 11, 1103-7 (1976)

74. Morgan, P.E.D., "Production and Formation of Si_3N_4 from Percusor Materials", Report # A-X3316, March – December 1973, 9-13.

75. Mazdiyasni, K.S., and Cooke, C.M., "Synthesis, Characterization, and Consolidation of Si_3N_4 Obtained from Ammonolysis of $SiCl_4$", J. Am. Ceram. Soc., 56, 628-33 (1973)

76. Rutgers, G. A. W., and DeVos, J. C., "The Relation Between Brightness Temperature, True Temperature, and Colour Temperature of Tungsten", Physica, 20, 715 (1954).

77. Hedvall, J. A., Reactivity of Solids, Verlag: Johann Ambrososius Barth, Leigzig, 1938.

78. Christian, J. W., The Theory of Transformations in Metals and Alloys, Part 1, Pergamon Press, 1-20 (1975).

79. Turnbull, D. "Isothermal Rate of Solidification of Small Droplets of Mercury and Tin", J. Chem. Phys., 18, 768 (1950).

80. Christian, J. W., The Theory of Transformations in Metals and Alloys, Part 1, Pergamon Press, 441 (1975).

81. Danforth, S.C. and Richman, M.H., "Strength and Fracture Toughness of Reaction Bonded Si_3N_4". Submitted to the J. Am. Ceram. Soc.

82. Anstis, G.R., Chantikul, P., Laun, B.R., and Marshall, D.B., "A Critical Evalution of Identation Techniques for Measuring Fracture Toughness: I, Direct Crack Measurements", J. Am. Ceram. Soc., 64, 553-8 (1981).

83. Wills, R.R., Mendiratta, M.G., and Petrovic, J.J., "Controlled Surface Flaw – Initiated Fracture in Reaction Bonded Si_3N_4", J. Mater. Sci., 11, 1330-4 (1979).